
Electronic Thesis and Dissertation Repository

4-11-2017 12:00 AM

Basic Science to Clinical Research: Segmentation of Ultrasound and Modelling in Clinical Informatics

Ali K. Hamou
The University of Western Ontario

Supervisor
Mahmoud R. El-Sakka
The University of Western Ontario

Graduate Program in Computer Science
A thesis submitted in partial fulfillment of the requirements for the degree in Doctor of Philosophy
© Ali K. Hamou 2017

Follow this and additional works at: <https://ir.lib.uwo.ca/etd>



Part of the [Bioinformatics Commons](#), [Biomedical Commons](#), [Health Information Technology Commons](#), and the [Signal Processing Commons](#)

Recommended Citation

Hamou, Ali K., "Basic Science to Clinical Research: Segmentation of Ultrasound and Modelling in Clinical Informatics" (2017). *Electronic Thesis and Dissertation Repository*. 4494.
<https://ir.lib.uwo.ca/etd/4494>

This Dissertation/Thesis is brought to you for free and open access by Scholarship@Western. It has been accepted for inclusion in Electronic Thesis and Dissertation Repository by an authorized administrator of Scholarship@Western. For more information, please contact wlsadmin@uwo.ca.

Abstract

The world of basic science is a world of minutia; it boils down to improving even a fraction of a percent over the baseline standard. It is a domain of peer reviewed fractions of seconds and the world of squeezing every last ounce of efficiency from *a processor, a storage medium, or an algorithm*. The field of health data is based on extracting knowledge from segments of data that may improve some clinical process or practice guideline to improve the time and quality of care. Clinical informatics and knowledge translation provide this information in order to reveal insights to the world of improving patient treatments, regimens, and overall outcomes.

In my world of minutia, or basic science, the movement of blood served an integral role. The novel detection of sound reverberations map out the landscape for my research. I have applied my algorithms to the various anatomical structures of the heart and artery system. This serves as a basis for segmentation, active contouring, and shape priors. The algorithms presented, leverage novel applications in segmentation by using anatomical features of the heart for shape priors and the integration of optical flow models to improve tracking. The presented techniques show improvements over traditional methods in the estimation of left ventricular size and function, along with plaque estimation in the carotid artery.

In my clinical world of data understanding, I have endeavoured to decipher trends in Alzheimer's disease, Sepsis of hospital patients, and the burden of Melanoma using mathematical modelling methods. The use of decision trees, Markov models, and various clustering techniques provide insights into data sets that are otherwise hidden. Finally, I demonstrate how efficient data capture from providers can achieve rapid results and actionable information on patient medical records. This culminated in generating studies on the burden of illness and their associated costs.

A selection of published works from my research in the world of *basic sciences* to *clinical informatics* has been included in this thesis to detail my transition. This is my journey from one contented realm to a turbulent one.

Keywords

Basic Science, Clinical Informatics, Segmentation, Active Contours, Alzheimer's Disease, Sepsis, Markov modelling, Clustering, Decision Tree's, Disease Management Systems, Chronic Diseases.

Co-Authorship Statement

All works presented in this thesis were fully or co-written by the author. All mathematical algorithms were fully or partially implemented by the author or improved upon from prior versions of a codebase. Other than my supervisor, additional authors provided support on clinical interpretations and clinical understanding for associated sections.

For further details, please refer to the "Integrated Articles" section.

Epigraph

“Yesterday I was clever, so I wanted to change the world. Today I am wise, so I am changing myself.” – Rumi

Dedication

To my lovely patient wife, and the four monsters that haunt her constantly...

Acknowledgments

I would like to thank and praise *Allah* almighty, for always lighting the path of my long arduous journey. May I always hold true to the principles laid out by *Him*.

I would like to express my utmost gratitude to my supervisor and guide *Mahmoud El-Sakka* for his constant encouragement, support and uplifting spirit that made this research possible and enjoyable. His invaluable advice, whether for academia or otherwise, has shaped the way I view the world around me.

To my friends in the London community, I will never forget all of their support, understanding and kindness. May *Allah* bless this wonderful group of people for all of their hard work on keeping our Ummah strong.

Much gratitude goes to my loving sister, *Fatima Hamou*, a dweller of the desert, who reviewed my cumbersome dissertation drafts and provided many suggestions and edits along the way.

Finally, I would like to recognize the strong appreciation and moral support from my family, and especially my Mother and Father, *Olmaza* and *Khaled Hamou*. Their constant drive to help me achieve excellence in all of my endeavours will be rewarded with my everlasting worship on their behalf.

Of course, my utmost thanks and affection go to my beloved wife *Rasha El-Sabaawi*, for her patience, love, encouragement and understanding – in the face of raising our four wonderful kids (*Khaled, Nusayba, Sarah* and *Fatima*) throughout.

Table of Contents

Abstract	ii
Keywords	iii
Co-Authorship Statement.....	iii
Epigraph.....	iv
Dedication	v
Acknowledgments.....	vi
Table of Contents.....	vii
List of Tables	xii
List of Figures	xiii
Preface.....	1
Integrated Articles.....	2
Chapter 1	5
1 Basic Science Introduction.....	5
1.1 Heart Disease and Stroke Overview	5
1.2 Relevant Imaging Technologies	6
1.3 Ultrasound Focus	7
1.4 Selection of Papers.....	9
1.5 References.....	9
Chapter 2 - Article 1	12
2 Carotid Ultrasound Segmentation using DP Active Contours.....	12
2.1 Introduction.....	12
2.2 System and Methods	15
2.2.1 External Energy Formulation.....	15
2.2.2 Canny Edge Detection	16
2.2.3 A-Priori knowledge.....	18
2.2.4 Clinical Metrics.....	19

2.3 Results.....	21
2.4 Conclusions.....	23
2.4.1 Contributions.....	24
2.5 Acknowledgements.....	24
2.6 References.....	24
Chapter 3 – Article 2.....	26
3 Active Contours with Optical Flow and Primitive Shape Priors for Echocardiographic Imagery	26
3.1 Introduction.....	26
3.2 Background.....	29
3.2.1 Active Contours	29
3.2.2 Optical Flow.....	30
3.3 Description of Proposed Model	32
3.4 Experimental Results	35
3.5 Conclusions.....	39
3.6 Acknowledgements.....	39
3.7 References.....	39
Chapter 4 – Article 3.....	42
4 SRAD, Optical Flow and Primitive Prior based Active Contours for Echocardiography	42
4.1 Introduction.....	42
4.2 System and Methods	45
4.2.1 Parametric Active Contour Review	46
4.2.2 SRAD Measurements.....	48
4.2.3 Optical Flow Estimates	50
4.2.4 Primitive Shape Measurements on Contour Points	52
4.2.5 Fusion Characteristics	54
4.3 Results and Discussion	54
4.4 Conclusions.....	58

4.5 Acknowledgements.....	58
4.6 References.....	58
Chapter 5.....	62
5 Clinical Sciences Introduction	62
5.1 Selection of Papers.....	65
5.2 References.....	66
Chapter 6 – Article 4.....	68
6 Cluster Analysis of MR Imaging in Alzheimer’s Disease using Decision Tree Refinement	68
6.1 Introduction.....	68
6.2 Systems and Methods	70
6.2.1 Dataset Source	70
6.2.2 Tissue Classification and Regional Segmentation.....	70
6.2.3 Variables	72
6.3 Analysis.....	72
6.3.1 Cluster Analysis	72
6.3.2 Decision Trees	74
6.4 Discussion and Conclusions	76
6.5 References.....	79
Chapter 7 – Article 5.....	81
7 A Markov Analysis of Patients Developing Sepsis using Clusters	81
7.1 Introduction.....	81
7.1.1 Analytic Techniques	82
7.2 Methods.....	83
7.2.1 Data Acquisition	83
7.2.2 Model Formulation	84
7.3 Results.....	88
7.3.1 Further Implications.....	90

7.3.2	Validation.....	91
7.3.3	Future Work.....	91
7.4	Conclusions.....	92
7.5	References.....	92
Chapter 8 – Article 6.....		95
8	A Disease Registry and Disease Management System for Patients with Malignant Melanoma.....	95
8.1	Introduction.....	95
8.2	Methods.....	96
8.2.1	System Design	96
8.2.2	Collecting Patient Information.....	97
8.2.3	Imaging	99
8.2.4	Access and Security	99
8.2.5	Reporting and Analysis.....	100
8.3	Conclusions.....	100
8.4	Acknowledgements.....	101
8.5	References.....	102
Chapter 9 – Article 7.....		103
9	Burden of illness for metastatic melanoma in Canada: 2011–2013.....	103
9.1	Introduction.....	104
9.2	Methods.....	105
9.2.1	Epidemiologic Analysis: Melanoma-Related Disease Characteristics ...	105
9.2.2	Statistical Methods.....	105
9.3	Results.....	105
9.3.1	Patient Characteristics.....	105
9.3.2	Treatment Modalities	106
9.3.3	Factors Affecting Survival	107
9.4	Discussion	109

9.5 Conclusions.....	111
9.6 Acknowledgments.....	111
9.7 Conflict of Interests Disclosure	111
9.8 References.....	119
Chapter 10.....	123
10 Concluding Thoughts	123
10.1 Transition	124
10.2 Future Outlook.....	124
Appendix.....	126
Curriculum Vitae	127

List of Tables

Table 4-1: Sensitivity, precision rate and overlap ratio of the proposed system	56
Table 6-1: Demographics of AddNeuroMed dataset	79
Table 7-1: Sepsis Study: 25 variables collected to form a single datapoint	85
Table 9-1: Patient characteristics by initial stage at diagnosis	114
Table 9-2: Number of patients with unresectable or metastatic disease utilizing treatment modalities by line of treatment	116
Table 9-3: Variables in the Cox proportional model for survival at 1 year	117
Table 9-4: Variables in the Cox proportional model for survival at 2 years	118

List of Figures

Figure 2-1: Example of Edge detection. (a) Original carotid US image. (b) Canny edge detected binary image (c) Modified Canny edge detected grayscale image (d) Distance transformed modified Canny edge detected image.....	17
Figure 2-2: Active contour on a carotid ultrasound image. (a) without a-priori knowledge. (b) with a-priori knowledge.	20
Figure 2-3: (a) Drawing of NASCET criteria for evaluation of carotid stenosis: A is the diameter of the residual lumen at the point of maximal stenosis (vertical lines representing plaque); B is the diameter of the normal artery distal to the stenosis. (CCA, ECA and ICA stand for Common, External and Internal Carotid Artery, respectively) (b) Ultrasound image of a cross-sectional slice, at line L in (a), showing the area of the carotid. Image is histogram equalized for better visualization.	20
Figure 2-4: Transverse carotid artery US images of the carotid bulb. (a) the original image. (b) the original image manually segmented by a clinical radiologist. (c) original image with four points – white circles – placed by the clinical radiologist as an initial value for the algorithm and the extracted prior ellipse as a dashed line. (d) the resulting segmentation by the proposed active contour algorithm.	22
Figure 2-5: Transverse carotid artery US images of the internal carotid artery. (a) the original image (b) the original image manually segmented by a clinical radiologist. (c) original image with four points – white circles – placed by the clinical radiologist as an initial value for the algorithm and the extracted prior ellipse as a dashed line. (d) the resulting segmentation by the proposed active contour algorithm.	23
Figure 3-1: An example of the virtual electric field on standard U-Image.....	30
Figure 3-2: An example of an optical flow field on a Rubik's cube rotated image; (a) Rubik's cube at time t ; (b) Rubik's cube at time $t+\Delta t$; (c) optical flow.....	32
Figure 3-3: Generation of primitive priors on active contour points.	34
Figure 3-4: An example of a primitive prior formulation on the left ventricle.....	34
Figure 3-5: Flow Chart of Proposed Algorithm.....	36

Figure 3-6: Segmenting the left ventricle of the heart (a) Expert manual segmentation (b) standard GVF segmentation (c) GVF-optical flow segmentation with priors.	36
Figure 3-7: Sensitivity using different external energies	38
Figure 3-8: System Accuracy using different external energies.....	38
Figure 4-1: Example of gradient vector forces; (a) standard U-Image, and (b) Gradient Vector Flow of U-Image	49
Figure 4-2: An example of an optical flow field on a Rubik's cube rotated image; (a) cube at time t , (b) cube at time $t+\Delta t$, and (c) Optical flow of image (a) to (b) using Lucas-Kanade method (originally published in <i>Barron et al.</i> [3]).	51
Figure 4-3: Left ventricle primitive shape fitting; (a) primitive shape fitting algorithm using two hyperbolas, and (b) echocardiogram with segmentation overlay; solid line represents primitive whereas X-line represents active contour	53
Figure 4-4: Top level block diagram of proposed scheme	55
Figure 4-5 Segmentation results; (a) LV echocardiogram, (b) SRAD diffusion of image (a), (c) manual expert delineation of image (a), (d) and (e) segmentations when utilizing GVF only and when utilizing the proposed scheme, respectively.....	57
Figure 6-1 Cluster analysis of AddNeuroMed dataset modeled on 3D space proximity grid. (a) Full variable selection to create a cluster fields. (b) Using only the variables determined to be of value by decision trees. (Implementations of clustering and graphing were applied using C++ and Matlab).....	78
Figure 6-2: Decision tree comparison of normal patients and categorized Alzheimer's patients	79
Figure 7-1: Markov transition graph represented by first cluster	89
Figure 7-2: Portion of Markov Graph.....	90
Figure 8-1: Data collection forms	98
Figure 8-2: Imaging for pathology and general patient	99

Figure 8-3: Analytics Module	101
Figure 9-1: Flow diagram of metastases developed during the course of disease and resectability by disease stage at initial diagnosis.	112
Figure 9-2: Kaplan-Meier survival curves for (A) patients with unresectable or metastatic disease vs all other patients in the entire cohort; (B) entire cohort by disease stage; (C) patients with unresectable or metastatic disease by presence or absence of BRAF mutation; and (D) patients with unresectable or metastatic disease by presence or absence of brain metastasis.....	113

Preface

Throughout this thesis, several published articles have been presented to represent my transition from basic sciences research to clinical informatics research. In one way or another, the techniques described in each article build on each other, and have fostered the nurturing of my skills to continue into the world of clinical informatics.

Though some of these works were published earlier on during my research tenure, my intention is to demonstrate that I would not have accomplished or ended up at my current research state without such prior works.

Please note, this is not a complete list of my published works during this period.

Integrated Articles

Basic Sciences Articles

1. **Ali K. Hamou**, Said Osman and Mahmoud R. El-Sakka, “Carotid Ultrasound Segmentation Using DP Active Contours”, *International Conference on Image Analysis and Recognition (ICIAR)*, 2007, LNCS 4633, pp. 961-971.
2. **Ali K. Hamou** and Mahmoud R. El-Sakka, “Active Contours with Optical Flow and Primitive Shape Priors for Echocardiographic Imagery”, *International Conference on Imaging Theory and Applications (IMAGAPP)*, 2009, pp. 111-118.
3. **Ali K. Hamou** and Mahmoud R. El-Sakka, “SRAD, Optical Flow and Primitive Prior based Active Contours for Echocardiography”, *Computer Vision, Imaging and Computer Graphics. Theory and Applications. VISIGRAPP 2009. Communications in Computer and Information Science*, 2010, Springer Berlin / Heidelberg, vol. 68, pp. 158-171.

Delegation of Work Presented: Written work, development and implementation of all presented articles by Ali Hamou. Review, consultation and supervision of all work was provided by Mahmoud El-Sakka. A gold standard tracing for the testing of algorithms and results was provided by Said Osman.

Clinical Sciences Articles

4. **Ali Hamou**, Michael Bauer, Benoit Lewden, Andrew Simmons, Yi Zhang, Lars-Olof Wahlund, Catherine Tunnard, Iwona Kloszewska, Patrizia Mecozzi, Hilkka Soininen, Magda Tsolaki, Bruno Vellas, Sebastian Muehlboeck, Alan Evans, Per Julin, Niclas Sjögren, Christian Spenger, Simon Lovestone, Femida Gwadry-Sridhar, and other participants in the AddNeuroMed consortium, “Cluster Analysis and Decision Trees of MR Imaging in Patients Suffering Alzheimer’s”, *Trends in Practical Applications of Agents and Multiagent Systems, Advances in Soft Computing*, 2010, vol. 71, pp. 477-484.
5. Femida Gwadry-Sridhar, Michael Bauer, Benoit Lewden, **Ali Hamou**. “A Markov Analysis of Patients Developing Sepsis Using Clusters”, *Knowledge Representation for Health-Care. KR4HC 2010. Lecture Notes in Computer Science, Springer*. 2011, vol. 6512, pp. 85-100.
6. **Ali Hamou**, Stacey Guy, Alexandria Ratzki-Leewing, Jesse O’Brien, Femida Gwadry-Sridhar, “A Disease Registry and Disease Management System for Patients with Malignant Melanoma”, *AHIC – Advances in Health Informatics Conference*, 2012, 4 Pages.
7. Scott Ernst, Teresa Petrella, Anthony Joshua, **Ali Hamou**, Marroon Thabane, Sharon Vantyghem, & Femida Gwadry-Sridhar. “Burden of illness for metastatic melanoma in Canada, 2011–2013”, *Current Oncology*, 2016 vol. 23(6), pp. 563-570.

Delegation of Work Presented: Written work, development and implementation of all presented articles by Ali Hamou. Partial support on codebases was provided by Benoit

Lewden and Jesse O'Brien. Review and support of written work by Stacy Guy and Alexandria Ratzki-Leewing. Review of work and consultation was provided by Michael Bauer and Femida Gwadry-Sridhar. Medical doctors Scott Ernst, Teresa Petrella, Anthony Joshua provided clinical expertise. Sharon Vantighem and Marroon Thabane provided funding contributions for the study. All remaining authors were members of the AddneuroMed Consortium who provided imaging and metric data sets for the work to be conducted on and background information on how the sets were created.

Related articles though not included

The following articles, though may be relevant, are not included in this dissertation as they build on the articles already depicted:

8. Femida Gwadry-Sridhar, Soodeh Nikan, **Ali Hamou**, Soo Jin Seung, Teresa Petrella, Anthony Joshua, Scott Ernst, Nicole Mittmann. "Resource utilization and costs of managing patients with advanced melanoma: a Canadian population-based study", *Current Oncology*, (IN PRESS)
9. **Ali Hamou**, Jesse O'Brien, Femida Gwadry-Sridhar, "Comprehensive Web-Based Patient Data Collection Systems with Integrated Imaging Functionality", *MICCAI - Medical Image Computing and Computer Assisted Intervention, High Performance and Distributed Computing for Medical Imaging Workshop*, 2011, 7 Pages.
10. **Ali Hamou**, Jesse O'Brien, Stacey Guy, Femida Gwadry-Sridhar, "InfoFrame – An Intelligent Informatics Data Collection Framework", *IEEE Computer Based Medical Systems*, 2011, pp. 1-6.
11. Femida Gwadry-Sridhar, **Ali Hamou**, Benoit Lewden, Claudio Martin, Michael Bauer, "Predicting Sepsis: A Comparison of Analytical Approaches", *Electronic Healthcare for the 21st Century, (eHealth 2010), Lecture Notes of the Institute for Computer Sciences, Social Informatics and Telecommunications Engineering*, Springer, Berlin, Heidelberg. 2011, vol. 69, pp. 95-102.
12. **Ali Hamou**, Stacey Guy, Benoit Lewden, Adam Bilyea, Michael Bauer and Femida Gwadry-Sridhar, "Data Collection with iPhone Web Apps: Efficiently Collecting Patient Data Using Mobile Devices", *International Conference on e-Health Networking, Application & Services (HealthCom)*, 2010, pp 235-239.
13. **Ali K. Hamou** and Mahmoud R. El-Sakka, "An SRAD and Optical Flow Based External Energy for Echocardiograms", *International Conference on Image Processing (ICIP)*, 2009, pp. 2613-2616.

BASIC SCIENCES

Chapter 1

1 Basic Science Introduction

“A worker in basic scientific research is motivated by a driving curiosity about the unknown. When his explorations yield new knowledge, he experiences the satisfaction of those who first attain the summit of a mountain or the upper reaches of a river flowing through unmapped territory. Discovery of truth and understanding of nature are his objectives. His professional standing among his fellows depends upon the originality and soundness of his work.”

National Science Foundation, Annual Report, 1953 – “What is Basic Research”

My journey begins here.

Basic science research (i.e. pure or fundamental research) is a methodical study directed toward greater knowledge or understanding of the fundamental aspects of phenomena. [1] It has a very measurable and practical end goal, without a specific product in mind. It is founded in curiosity where an application or particular problem can be solved or improved upon. This is the type of research where foundations are layered upon and advancement of fundamental parts are achieved. An unexpected discovery is many a times the catalyst for basic science research, and the flood gates of systemic research follows.

1.1 Heart Disease and Stroke Overview

Computer imaging and imaging technologies were my primary interest. I have continued my exploration of the cardiovascular system, which was the logical progression to my earlier research endeavours. [2][3][4] Being extremely interested in specific cardiovascular diseases and treatment methodologies, I set out to understand the nature of imaging, and specific

testing on the heart. In 1992, the Advisory Board of the International Heart Health Conference stated: “*Cardiovascular disease is largely preventable. We have the scientific knowledge to create a world in which most heart disease and stroke could be eliminated.*” [5] I wanted to be a part of that initiative.

Heart disease and stroke cost the Canadian economy more than \$20.4 billion every year, in physician services, hospital costs, lost wages and decreased productivity. [6] Sadly, one in three deaths in Canada is still due to heart disease and stroke alone. [6] In order to help reduce such costs, the use of modern day technologies need to be developed in order to help simplify and reduce a medical practitioner’s daily workload. The advent in ultrasonography is one such technique.

The assessment of cardiac function has been a major area of interest in the medical field. Normal heart function includes pumping chambers (known as ventricles) which regulate the systemic and pulmonary circulation systems by delivering blood to the proper areas. [7] Abnormal heart function in the left ventricle (LV) can be caused by systolic dysfunction, (i.e. the reduction in the ability to contract) or diastolic dysfunction (i.e. the inability to fill efficiently). Along with function, other various heart structures (e.g. valves and tissues) may fail at any point causing cardiomyopathies, endangering the life of the host individual. Fortunately, many myopathies are treatable (with medication, implanted pacemakers, defibrillators, or ventricular assist devices) given early detection. Standard clinical metrics such as an ejection fraction (i.e. the fraction of blood pumped out of a ventricle with each heart beat) plays a large role in such detections. [7]

1.2 Relevant Imaging Technologies

Several imaging modalities of cardiac function have each evolved independently in order to measure left ventricular function, various valve analysis and myocardial perfusion for various patients and research studies. These include:

Cardiovascular Magnetic Resonance (CMR) [8] – a powerful medical imaging modality due to its non-invasiveness and remarkable flexibility. CMR is able to produce high-resolution *in vivo* images of vascular anatomy and to a lesser degree measure blood flow rates through vessels. Though CMR’s current limitations include: 1) low accessibility, due to

significant costs for setup and operation, 2) poor out of plane spatial resolution, and 3) lengthy procedure times (often up to an hour depending on the scanning protocol)

Cardiac Computed Tomography (CT) [9] – extended the life of the traditional x-ray imaging techniques by providing tomographical images rather than projections of anatomy. CT imaging eliminates the superposition of multiple vessels problem, found in traditional x-ray measurements. However, pronounced coronary calcification, especially in patients with high heart rates, and motion artifacts can render images difficult or even impossible to interpret. Patients with arterial fibrillation or other arrhythmias cannot be evaluated.

Cardiac Positron Emission computed Tomography (PET) [10] – is a nuclear medicine technique that can produce a functional image map of the heart. Generally, a tracer (radioactive isotope) is injected into the body and tracked by a scanner. Analysis reconstructs the flow of the isotope throughout the various heart chambers and generates a three-dimensional map. This imaging technique not only shares many of the limitations of CT but is also invasive and expensive to administer.

Echocardiography [11, 12] – involves the transmission and reception of directional ultrasound (acoustical) waves in order to form image data of the heart, (also known as cardiac ultrasound). Echocardiography can produce accurate assessment of blood velocity and cardiac tissue at any arbitrary point using pulsed or continuous ultrasound waves. This allows for various cardiac valve and function assessment.

1.3 Ultrasound Focus

All of my basic science research has focused on the use of ultrasound technologies as it provides an inexpensive non-invasive means for visualizing various tissues within the human body. However, these visualizations tend to be filled with speckle noise and other artifacts, due to the sporadic nature of high frequency sound waves. Many techniques for segmenting ultrasound images have been introduced in order to deal with these problems [13, 14, 15, 16, 17, 18].

Several types of US (e.g., Doppler, B-mode, Pulse Inversion, Harmonic, etc) have proven to be useful tools for medical imagery [16][19]. Doppler US measures the Doppler shift between impinging ultrasound waves that are scattered by red blood cells [17]. This

technique can be used to determine the direction and speed of blood flow between vessels within the heart cavity. Though this can be used to estimate peak systolic and diastolic velocities, these flow based measurements suffer from problems concerning intra- and inter-operator variability due to the turbulent nature of the flow within the heart. A B-mode (brightness mode) US image is a two-dimensional tomographic display composed of bright dots by measuring the time-resolved reflected power of impinging ultrasound waves upon tissues and vessels in the body [20]. The echo amplitude determines the brightness of each dot which is sensitive to the boundaries between fluid filled structures, such as blood vessels and surrounding tissues. High-resolution B-mode ultrasonography has greatly improved the ability to identify problematic regions in the heart over other techniques (e.g. PET, CMR, CT) without risking the patient's well-being [12].

In the first integrated article, which has been cited 18 times as of the submission of this thesis, "Carotid ultrasound Segmentation using DP Active Contours" [21], two proposed alterations to the dynamic programming parametric active contour model (or snake) are introduced. The first alteration allows the snake to converge to the one-response result of a modified Canny edge detector. The second provides a function that allows a user to pre-set *a-priori* knowledge about a given object being detected, by means of curve fitting and energy modification. The results yield accurate segmentations of cross-sectional transverse carotid artery ultrasound images that are validated by independent clinical radiologists. Utilizing the proposed alterations leads to a reduction of clinician interaction time while maintaining an acceptable level of accuracy for varying measures such as percent stenosis.

In the second integrated article which has been cited 15 times as of the submission of this thesis, "Active Contours with Optical Flow and Primitive Shape Priors for Echocardiographic Imagery" [22] we propose the use of a new external energy for a Gradient Vector Flow (GVF) snake, consisting of the optical flow data of moving heart structures (i.e. the perceived movement). This new external energy provides more information to the active contour model to combat noise in moving sequences. An automated primitive shape prior mechanism is also introduced, which further improves the results when dealing with especially noisy echocardiographic image cines. Results were compared with that of expert manual segmentations yielding promising sensitivities and system accuracies.

In the third integrated article which was only cited 2 times as of the submission of this thesis, however this has been published as a book chapter as well, “SRAD, Optical Flow and Primitive Prior based Active Contours for Echocardiography” [23] we build on the previous work and include a new operator in the external energy to significantly improve the results. This energy consists of optical flow estimates of heart sequences along with the use of a speckle reducing anisotropic diffusion (SRAD) operator. Furthermore, an automatic primitive shape prior algorithm was employed to further improve the results and regularity of the snake, when dealing with especially speckle laden echocardiographic images. Results were compared with expert-defined segmentations yielding better sensitivity, precision rate and overlap ratio than the standard GVF model.

This selection of works concludes my basic science research and allows me to leap frog into the world of informatics research in the clinical domain.

1.4 Selection of Papers

The selection of these works demonstrates a growth in the presented techniques and how the development of the segmentation pipeline evolved over time. The additional works that were not selected in the basic science domain presented further cases and testing sets at conferences. The presented works have been used as a foundation in other research projects by external parties. We have provided the citation count for each of the works as depicted above. The first article presents the segmentation pipeline with alterations that help to segment borders in ultrasound images. The second builds on these techniques to provide inter-cine information to remove more noise and improve the segmentation accuracy. The final article adds additional algorithms to in noise reduction in order to garner further accuracy from the pipeline. All data was collected from volunteers and imaged under standard clinical practices in order to ensure developed algorithms could be used on patient supplied images.

1.5 References

1. Annual Report: "What is basic research?", *National Science Foundation*.
“http://www.nsf.gov/pubs/1953/annualreports/ar_1953_sec6.pdf” 1953.
2. Ali K. Hamou and Mahmoud R. El-Sakka, “A Novel Segmentation Technique For Carotid Ultrasound Images”, *IEEE International Conference on Acoustics, Speech, and Signal Processing (ICASSP)*, 2004, vol. 3, pp. 521-524.

3. Ali K. Hamou and Mahmoud R. El-Sakka, "Wavelet-Filter Performance Evaluation for Digital Images", *IEEE Canadian Conference on Electrical and Computer Engineering (CCECE)*, 2003, vol. 3, pp. 2075-2078.
4. Ali K. Hamou, "Segmentation of Carotid Artery Ultrasound Images", *The University of Western Ontario, Master of Science Dissertation*, 2003.
5. The Victoria Declaration on Heart Health. *The Advisory Board International Heart Health Conference*, Canada, 1992.
6. Conference Board of Canada, *Tracking Heart Disease and Stroke in Canada*, 2010.
7. Zimmerman, J. "The functional and surgical anatomy of the heart", *Annals of The Royal College of Surgeons of England*, 1966, 39(6), pp. 348-366.
8. Dudley J. Pennell, Udo P. Sechtem, Charles B. Higgins, Warren J. Manning, Gerald M. Pohost, Frank E. Rademakers, Albert C. van Rossum, Leslee J. Shaw, E. Kent Yucel, "Clinical indications for cardiovascular magnetic resonance (CMR): Consensus Panel report", *European Heart Journal*, 2004; 25 (21): pp. 1940-1965.
9. Ritman, E. "Cardiac computed tomography imaging: a history and some future possibilities", *Cardiology Clinics*, 2003, vol. 21(4), pp. 491-513.
10. Ghosh, N; Rimoldi OE; Beanlands RS; Camici PG, "Assessment of myocardial ischaemia and viability: role of positron emission tomography", *European Heart Journal*, 2012, vol. 31(24), pp. 2984-2995.
11. Ommen, S., Nishimura, R., Appleton, C., Miller, F., Oh, J., Redfield, M. and Tajik, A. "Clinical utility of Doppler echocardiography and tissue Doppler imaging in the estimation of left ventricular filling pressures: A comparative simultaneous Doppler-catheterization study" *Circulation*, 2000, vol. 102(15), pp. 1788-1794.
12. Singh S, Goyal A. The Origin of Echocardiography: A Tribute to Inge Edler. *Texas Heart Institute Journal*, 2007, vol. 34(4), pp. 431-438.
13. Abolmaesumi, P., Sirouspour, M., and Salcudean, S. "Real-time extraction of carotid artery contours from ultrasound images", *IEEE International Symposium on Computer Based Medical Systems*, 2000, pp. 181-186.
14. Collaris, R. and Hocks, A. "Automatic detection of closed tumor contour in medical ultrasound images on the basis of level-dependent spatial summation", *IEEE Engineering in Medicine and Biology Society*, 1996, vol. 2, pp. 907-908.
15. Felix-Gonzalez, N. and Valdes-Cristerna R. "3D echocardiographic segmentation using the mean-shift algorithm and an active surface model", *Medical Imaging - Image Processing*, 2006, vol. 6144, pp. 147-151.
16. Papademetris, X., Sinusas, A., Dione, D., and Duncan, J. "3D cardiac deformation from ultrasound images", *Medical Image Computing and Computer-Assisted Intervention*, 1999, pp. 420-429.
17. Qiu, Wu, et al. "Automatic segmentation approach to extracting neonatal cerebral ventricles from 3D ultrasound images", *Medical image analysis*, 2017, vol. 35, pp. 181-191.

18. Noble, J. A., and D. Boukerroui. "Ultrasound Image Segmentation: A Survey", *IEEE Transactions on Medical Imaging*, 2006, vol. 25(8) pp. 987-1010.
19. Atkinson, P. and Woodcock, J., "Doppler ultrasound and its use in clinical measurements", *Academic Press*, 1982.
20. Donald, I., MacVicar, J. and Brown, T. "Investigation of abdominal masses by pulsed ultrasound", *Lancet*, 1958, vol. 1(7032), pp. 1188-1195.
21. Ali K. Hamou, Said Osman and Mahmoud R. El-Sakka, "Carotid Ultrasound Segmentation Using DP Active Contours", *International Conference on Image Analysis and Recognition (ICIAR)*, 2007, LNCS 4633, pp. 961-971.
22. Ali K. Hamou and Mahmoud R. El-Sakka, "Active Contours with Optical Flow and Primitive Shape Priors for Echocardiographic Imagery", *International Conference on Imaging Theory and Applications (IMAGAPP)*, 2009, pp. 111-118.
23. Ali K. Hamou and Mahmoud R. El-Sakka, "SRAD, Optical Flow and Primitive Prior based Active Contours for Echocardiography", *Computer Vision, Imaging and Computer Graphics. Theory and Applications. (VISIGRAPP 2009). Communications in Computer and Information Science*, 2010, Springer Berlin / Heidelberg, vol. 68, pp. 158-171.

Chapter 2 - Article 1

2 Carotid Ultrasound Segmentation using DP Active Contours*

Abstract: Ultrasound provides a non-invasive means for visualizing various tissues within the human body. However, these visualizations tend to be filled with speckle noise and other artifacts, due to the sporadic nature of high frequency sound waves. Many techniques for segmenting ultrasound images have been introduced in order to deal with these problems. One such technique is the active contouring.

In this paper, two proposed alterations to the dynamic programming parametric active contour model (or snake) are introduced. The first alteration allows the snake to converge to the one-response result of a modified Canny edge detector. The second provides a function that allows a user to preset *a-priori* knowledge about a given object being detected, by means of curve fitting and energy modification. The results yield accurate segmentations of cross-sectional transverse carotid artery ultrasound images that are validated by an independent clinical radiologist. Utilizing the proposed alterations leads to a reduction of clinician interaction time while maintaining an acceptable level of accuracy for varying measures such as percent stenosis.

Keywords: Ultrasound Imaging, Carotid Stenosis, Image Segmentation, Active Contour Models

2.1 Introduction

Carotid ultrasound (US) is considered an inexpensive non-invasive clinical procedure for evaluating many carotid artery diseases [10]. It provides flexibility for offline review of

* A version of this chapter has been published: Ali K. Hamou, Said Osman and Mahmoud R. El-Sakka, "Carotid Ultrasound Segmentation Using DP Active Contours", *International Conference on Image Analysis and Recognition (ICIAR)*, 2007, LNCS 4633, pp. 961-971.

patient records efficiently, i.e., the US images can be acquired by a clinician and stored for later testing and analysis, with minimal user input. A brightness-mode (or B-mode) US image is one of the two major types of US used on the carotid. This study will primarily focus on B-mode images since it provides an adequate means for an efficient clinical measurement of patients that are susceptible to plaque accumulation (whether from diet, genetics, obesity, etc). A B-mode US image is made up of a two-dimensional ultrasound display composed of bright pixels representing the ultrasound echoes and reverberations [16]. The echo amplitude determines the brightness of each pixel.

A high degree of carotid artery stenosis, which can be used as a pre-clinical disease marker, is an early indicator of a possible stroke. Stenosis is the abnormal narrowing of a blood vessel. It is generally caused by plaque build up [10]. Atheromatous plaque is an accumulation of fatty deposits that form inflamed patches within the inner lining of the arteries. In ultrasound images, hard (calcified) and soft plaque are represented as a range of high and low contrast pixels. However, these plaque areas have virtually the same levels of contrast to the surrounding soft tissue due to the lack of texture resolution and the high levels of noise inherent to US images. This poses many difficult problems for plaque and lumen detection algorithms since experienced clinicians subjectively dictate the amount of plaque build up based on knowledge of image structures and prior training.

Boundary detection is one of the most important elements of computer vision. Many techniques have been introduced to accomplish this task. One such example is an active contour model. Kass *et al.* [11] first proposed the original active contour model, also commonly known as a snake or a deformable model. In their formulation, image segmentation was posed as an energy minimization problem.

Active contours treat the surface of an object as an elastic sheet that stretches and deforms when external and internal forces are applied to it. These models are physically-based, since their behaviour is designed to mimic the physical laws that govern real-world objects [8]. This model helps solve the problems of edge based segmentation techniques, such as bleeding of the contour and unstable borders as exhibited in [1].

Active contour models have two inherent problems:

- *the proximity limitations of attaining a true boundary, especially when coupled with poor initialization plots*
- *the inability of traversing boundary concavities due to strong surface tension in the curve.*

The former is rarely an issue in the medical arena since clinicians are generally accepted as experts. Conversely, several studies have been conducted to overcome the latter, while also improving the accuracy and the speed of the original design. Of these are Dynamic Programming (DP) [5], level sets [18] and Gradient Vector Flow (GVF) models [19] just to name a few.

The DP parametric active contour provides an efficient algorithm to quickly attain a desired curve. In this study, we have chosen this model for this attractive feature. Within this model, we propose a new external energy to be made up of two distinct elements. The first is to be composed of an edge map resulting from a modified Canny edge detector. Canny edge detection will maintain the one-edge response and the local connectedness property of an image, whereas the active contour will ensure that our entire energy is minimized over the detected border [5]. The second will be the curve-fitted data built upon the user's initial plots and incorporated into the energy. This will amplify the amount of knowledge received from the clinician in acquiring a desired boundary.

The proposed segmentation algorithm is used to extract a cross-sectional area of the carotid artery at two specified positions (see Section 2.3), which is then used to calculate a percent stenosis that is less prone to user bias between clinicians. It is important to note that measuring the percent stenosis is usually done by manually estimating the diameter of the carotid via catheter angiography. This introduces large user bias into the calculations, while being quite costly from a clinician's time standpoint.

Abolmaesumi *et al.* [4] designed an efficient Kalman-star algorithm to estimate the location of the arterial wall. However, their algorithm still crosses the external boundaries of the wall due to the use of first degree gradient estimation.

Mao *et al.* [13] used a contour probability distribution (CPD) function in order to evaluate the accuracy of their segmentation algorithm. Their algorithm employed entropy mapping and

morphological operations based on gray-level values within an image. These mappings create an accurate identification of the arterial wall. However they are strenuous on computer systems resulting in long execution times.

A class of schemes [1,2,3,9] for carotid artery contour extraction that are based on the use of local edge detection techniques are proposed. However, these schemes are used globally throughout an image, and hence lack localization. All of these techniques are susceptible to leaking (or contour bleeding), especially if the image quality is not suitable. Hence other means are needed to properly segment the carotid and calculate its percent stenosis.

The rest of this paper is organized as follows. In Section 2, the proposed scheme is presented. The results of the scheme are shown in Section 3, and Section 4 contains conclusions.

2.2 System and Methods

2.2.1 External Energy Formulation

A snake is an energy minimization problem. Its energy is represented by two forces (internal energy, E_{in} , and external energy, E_{ex}) which work against each other. The total energy should converge to a local minimum – in the perfect case – at the desired boundary. The snake is defined as $X(s)$, where s belongs to the interval $[0,1]$. Hence, the total energy to be minimized to give the best fit between a snake and a desired object shape is:

$$\text{Total Energy} = \int_{s=0}^{s=1} \{E_{in}(X(s)) + E_{ex}(X(s))\} ds \quad (1)$$

The internal energy would force the curve to be smooth (by incorporating both elasticity and stiffness); whereas the external energy would force the curve towards image structures (image edges). The internal energy of the active contour formulation is further defined as:

$$E_{in}(X(s)) = \alpha \times \left(\frac{dX(s)}{ds} \right)^2 + \beta \times \left(\frac{d^2 X(s)}{ds^2} \right)^2 \quad (2)$$

where α and β are the weights of elasticity and stiffness, respectively. The first order term makes the snake's surface act like a membrane. The weight α controls the tension along the spine (stretching a balloon or elastic band). The second order term makes the snake act like a

thin plate. The weight β controls the rigidity of the spine (bending a thin plate or wire) [8]. We define our external energy as:

$$E_{ex} = \gamma \times \text{Canny}(f(x,y), \sigma, l, u) + \tau \times \text{Shape}(X(s)) \quad (3)$$

where γ and τ are the weights for the two proposed external energy elements, Canny and prior shape knowledge, respectively, and $f(x,y)$, σ , l , and u , represent the original image and the parameters for the Canny operator, being the degree of Gaussian blur, a lower threshold and an upper threshold. The weights γ and τ are important factors in governing whether the clinician's knowledge or the modified Canny edge map takes precedence in the converging snake model.

In general, active contour internal and external energies need to be balanced properly in order to converge to the desired edge in question. In order to properly tune the given curve with the proper weights, values were adjusted until the snake converged to the edges chosen by the radiologist. Samples were taken on both normal and diseased images in order to properly validate the curve with the chosen weights. Initially, equal weights were assigned to each energy. Gradually weights were shifted until acceptable edge convergence was achieved across several datasets. The weights α , β , γ and τ were set to 0.09, 0.01, 0.5, and 0.4, respectively. This is justified for the US images, since the modified Canny edge detector and the a-priori knowledge resides in the external energy formulation. Hence more weight should be shifted towards the external energy.

2.2.2 Canny Edge Detection

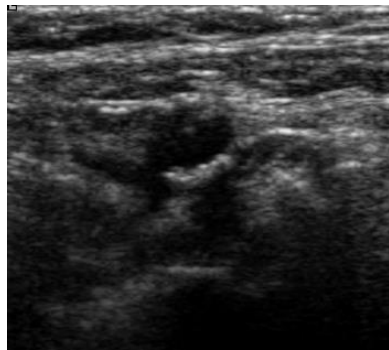
The Canny algorithm will first smooth the data (by means of a Gaussian filter) in order to remove speckle noise. Then edge detection is performed. Canny optimizes edge-response with respect to three criteria:

- *Detection*: real edges should not be missed, and false edges should be avoided.
- *Location*: the edge response should lie as close as possible to its true location.
- *One-response*: a true edge should not give rise to more than one response.

Canny is particularly susceptible to input parameters [6]. These parameters allow for fine-tuning of the edge-detection mechanism, permitting the user to acquire the desired results on an image data set. Canny uses a technique called “*non-maximum suppression*” that relies on

two thresholding values (lower and upper). The lower defines a threshold for all points that should not be considered lying on an edge. The upper defines a threshold for all the points guaranteed to be lying on an edge [6].

To emphasize the main edges in an image, the two thresholds should be large. To find the details of an image, their value should be small. The Canny edge detector was applied with increasing lower and upper thresholds and the resulting images were probed where expected edges should exist within the US images. Canny recommends that the lower threshold should be one third the amount of the upper threshold. Our trials are consistent with the recommended values yielding a 0.2 lower threshold and a 0.6 upper threshold. We also found these thresholds reduce the creation of false edges due to speckle noise in the image without degradation.



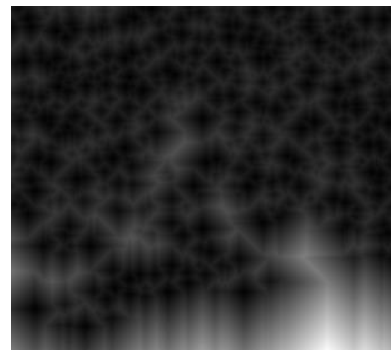
(a)



(b)



(c)



(d)

Figure 2-1: Example of Edge detection. (a) Original carotid US image. (b) Canny edge detected binary image (c) Modified Canny edge detected grayscale image (d) Distance transformed modified Canny edge detected image

Modification to the Canny edge detection algorithm was necessary in order to more accurately integrate this measure into the external energy. The standard Canny edge detector outputs all edges as a binary result. Each point that is lying on a Canny detected edge will not have the same weight following detection; rather it will be replaced with its relative gradient. Figure 2-1(a) shows an example of a carotid artery US image. Figure 2-1(b) shows the US image following the application of a normal Canny edge detector. The result is a binary image with all points having the same weight. Figure 2-1(c) shows the modified Canny edge detector where each point has a designated weight associated with its gradient – hence a gray scale image. Each gradient point is incorporated into the external energy by means of a Manhattan distance transform [17], as shown in Figure 2-1(d). The Manhattan distance transform provides a set of gray level intensities that show the distance to the closest boundary from each point. This provides a path to a better local minimum by avoiding small hazards of unwanted noise. The Manhattan distance of the modified Canny edge map was sufficient for the purpose of this study due to its simplicity and elegance of implementation. The energy will also converge such that it will mimic the behaviour of GVF snakes, since the curve will be forced into boundary concavities.

2.2.3 A-Priori knowledge

It is desirable to incorporate some means of shape to the model without directly involving the user. Automatic shape detection takes place on the initial plots positioned by the user. This would force the active contour to converge closer to the user's first delineated points. This is especially useful in the medical arena where a specialist or technician has a clear understanding of the underlying structure being detected, such as a liver, an artery, or a heart.

Traditional shape priors in snake models tend to take place in the internal energy [12]. However, this knowledge has been incorporated into the external energy in order to influence the shape and the positional information as well – since it is readily available from the user. This shape and position information will also be represented by the Manhattan distance transform in order to properly integrate it within the external energy.

For carotid images, the prior was set to ellipses. A least squares ellipse fitting technique is performed on the points of the initial contour. The initial ellipse is defined using the initial contour placement points of the snake. Continual refinement takes place by attempting to

minimize the geometric error of a series of approximating curves to the initial points. This process continues until a curve with minimal deviation from all snake contour points is found.

Figure 2-2(a) and Figure 2-2(b) shows the active contour being used without and with a-prior knowledge, respectively. Figure 2-2(a) depicts an improper segment of the boundaries, most likely due to poor visualization in the lower region of the image. Figure 2-2(b) takes the same initial plots and builds knowledge around the data by ellipse fitting in order to prevent the collapse of the curve and improve alignment with the true lumen.

2.2.4 Clinical Metrics

The desire to use the proposed technique in the clinical arena is paramount. One such metric is the *North American Symptomatic Carotid Endarterectomy Trial* (NASCET). This is a confirmed clinical test that may benefit patients with high-grade carotid stenosis [14]. The NASCET percent stenosis criterion is measured as: the diameter of lumen at the point of maximal stenosis, subtracted from the diameter of the lumen of the normal internal carotid artery, divided by the normal internal carotid artery multiplied by 100% [14]. The diameter of maximal stenosis is most often found just above the carotid bulb, near the bifurcation of the internal and external carotid arteries. A visual representation of this is shown in 4(a). This test is generally performed by catheter angiography – an invasive technique requiring surgery. In this paper, we propose an alternative method of measurement from a transverse segmented US image.

While, angiography will give a 2D representation on a *longitudinal* view of any given artery, yet it will not reveal any information on the depth of that artery. Depth can be measured by taking a cross-sectional area (*transverse*) slice of the carotid, as shown in Figure 2-3(b). This additional information should improve the traditional NASCET measurements. However, slight modification to our measurements is needed in order to conform to the NASCET standard. Since NASCET percent stenosis is based on artery diameters, where the proposed measure is based on areas, (in a generally elliptic fashion) each contour would be square rooted before the ratio is calculated. This will help to preserve the ratio of percent stenosis in a range that traditional clinicians are already familiar with, rather than introducing an entirely new range for stenosis.

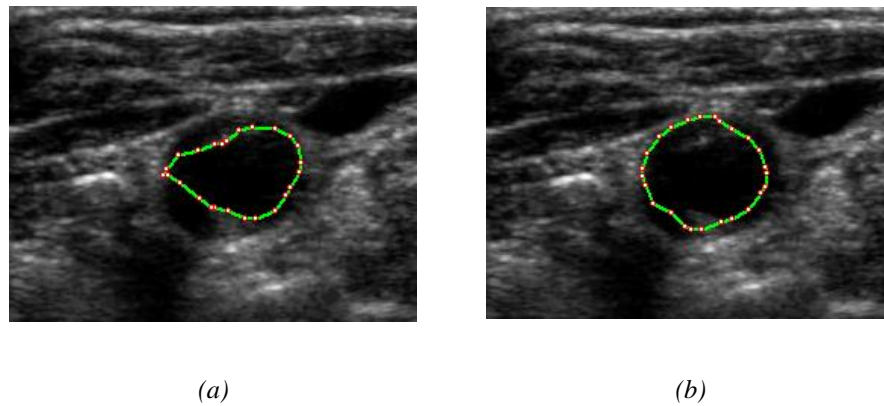
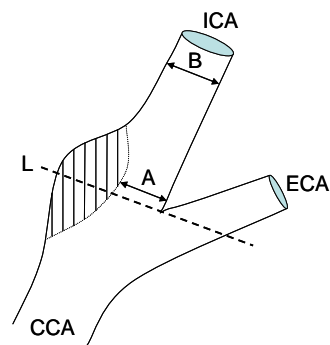
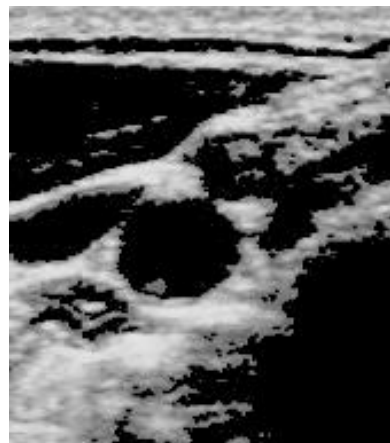


Figure 2-2: Active contour on a carotid ultrasound image. (a) without a-priori knowledge. (b) with a-priori knowledge.



$$\text{NASCET: } \frac{B - A}{B} \times 100\%$$

(a)



(b)

Figure 2-3: (a) Drawing of NASCET criteria for evaluation of carotid stenosis: A is the diameter of the residual lumen at the point of maximal stenosis (vertical lines representing plaque); B is the diameter of the normal artery distal to the stenosis. (CCA, ECA and ICA stand for Common, External and Internal Carotid Artery, respectively) (b) Ultrasound image of a cross-sectional slice, at line L in (a), showing the area of the carotid. Image is histogram equalized for better visualization.

2.3 Results

In this study, 91 carotid artery US images are used. These images include normal and diseased carotid arteries at different positions along the carotid artery, e.g., common carotid, carotid bulb, and internal carotid. Manual carotid lumen segmentation was performed on all of the images by a clinical radiologist. The images were then segmented by the proposed snake algorithm. These images were acquired using a SONOS 5500 by Philips Medical System.

Figure 2-4(a) shows a transverse 2-dimensional US image of the carotid bulb. Figure 2-4(b) represents the manually segmented region of the carotid bulb by a clinical radiologist at the given A position designated by the NASCET measure (as shown in Figure 2-3(a)). Figure 2-4(c) shows an example set of the four initial points plotted by the radiologist as an input to the active contour and the result of initial ellipse extraction. These points should be placed anywhere on the carotid lumen edge. They are required in order to achieve an elliptical approximation and the initial contour. Each point placed is automatically connected to its closest neighbour by means of a direct line of equally distanced points. Figure 2-4(d) shows the result of the active contour following convergence. Similarly, Figure 2-5(a), (b), (c) and (d) show the same for an internal carotid artery image (at location B designated by the NASCET measure). These results were ascertained by using the proposed active contour with parameters σ , l , u , α , β , γ , and τ , as 2.0, 0.2, 0.6, 0.09, 0.01, 0.5 and 0.4, respectively (as defined in Section 2.1).

All images processed by the proposed algorithm were examined and reviewed by a radiologist in a double-blind study in order to insure the segmentations were accurate. Due to the subjectivity in estimating the borders, the radiologist reported that the proposed technique would accurately objectify the inconsistencies among clinical practitioners. This will serve to improve the computation of percent stenosis and other measures used in the clinical arena.

Overall, accuracy of the proposed system was measured by comparing the 91 cases to the expert manual segmentations by the radiologist. These measurements include both type I and type II errors as defined in [18]. Since the images at hand were mainly small segmented foregrounds against vast backgrounds, the system would best be measured by means of its *sensitivity* and *precision rate*. Sensitivity is the number of true positives divided by the

number of true positives plus false negatives. In other words, it classifies how well a binary classification test correctly identifies a condition. Precision rate is the number of true positives divided by the number of true positives plus false positives. In other words, it classifies how accurate the results of the test are versus its inaccuracies. Sensitivity of the system, given a 95% confidence interval, yields $0.871 - 0.916$. Whereas, precision rate, given the same confidence interval, yields $0.866 - 0.903$. It is worth mentioning that these reported performance measures are quite high. This can be attributed to the fact that the initial points to the proposed system were plotted by the specialist.

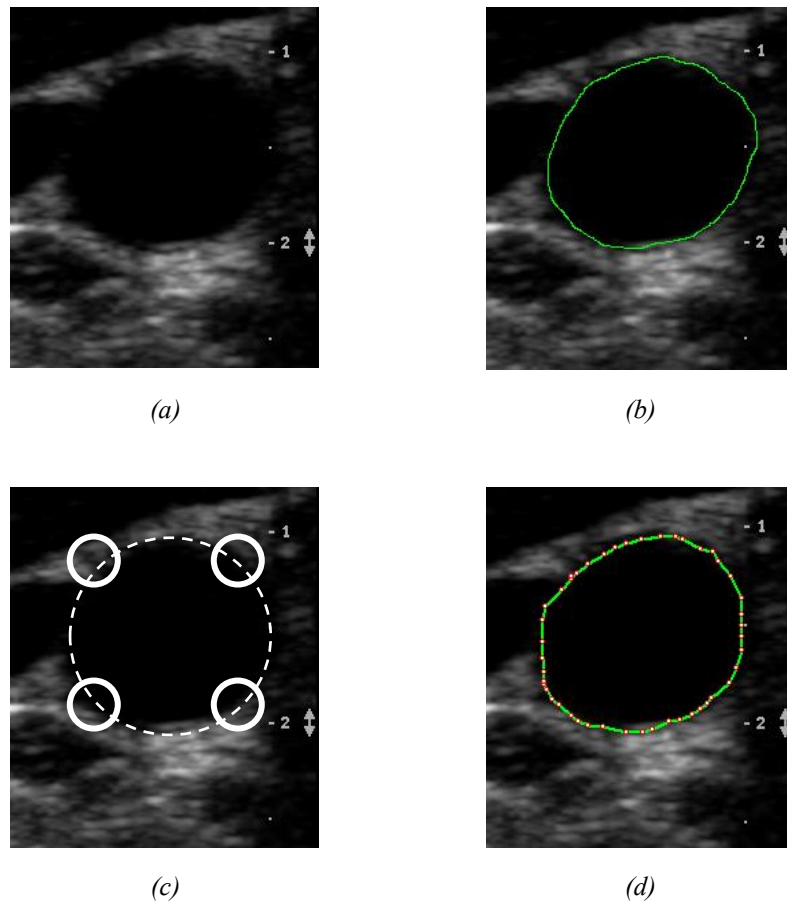


Figure 2-4: Transverse carotid artery US images of the carotid bulb. (a) the original image. (b) the original image manually segmented by a clinical radiologist. (c) original image with four points – white circles – placed by the clinical radiologist as an initial value for the algorithm and the extracted prior ellipse as a dashed line. (d) the resulting segmentation by the proposed active contour algorithm.

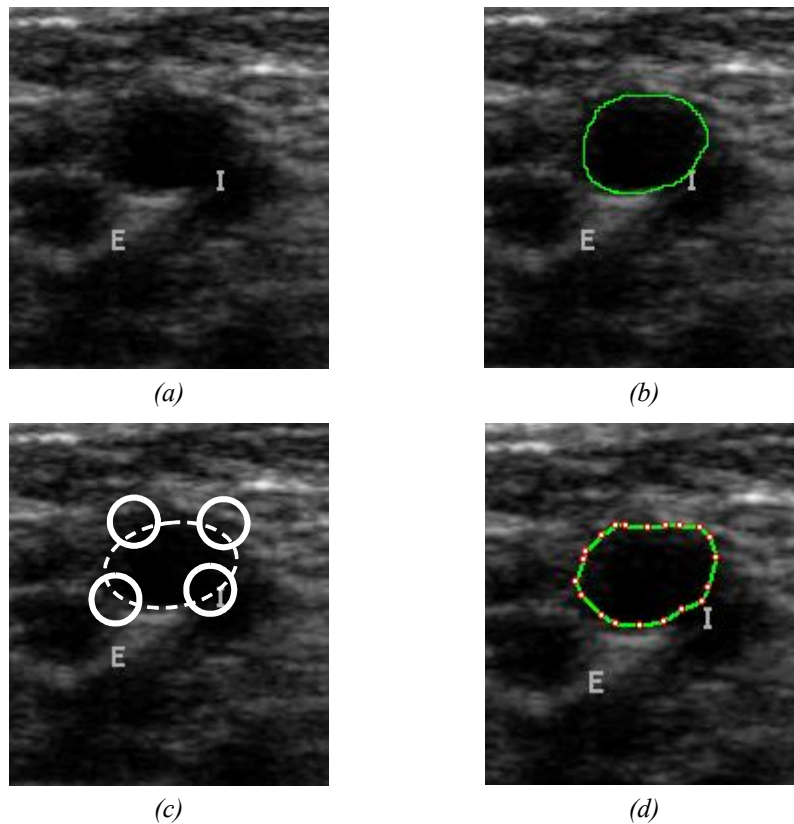


Figure 2-5: Transverse carotid artery US images of the internal carotid artery. (a) the original image (b) the original image manually segmented by a clinical radiologist. (c) original image with four points – white circles – placed by the clinical radiologist as an initial value for the algorithm and the extracted prior ellipse as a dashed line. (d) the resulting segmentation by the proposed active contour algorithm.

2.4 Conclusions

In this paper, a modified DP snake algorithm helped alleviate the inherent difficulties in segmenting ultrasound carotid artery images, such as avoiding speckle noise and contour bleeding. The proposed alterations utilized a modified Canny edge detector and a-priori knowledge. Experimental results show that these alterations tune the original DP snake model in order to be used in the medical arena so that clinical analysis results can be improved.

A radiologist verified that this objective segmentation scheme would improve the calculation of different clinical measures, such as percent stenosis, by reducing the inconsistencies and

variability between clinicians while reducing the time for clinician interaction. We have shown that the segmentation of the carotid artery is robust enough to be used in a clinical setting for specific domain applications.

2.4.1 Contributions

Author contributions are allocated as follows: research, development, implementation and paper writing were done by Ali Hamou, M.Sc., and Mahmoud El-Sakka, Ph.D. Result validation was done by Said Osman, M.D., FRCPC.

2.5 Acknowledgements

This research is partially funded by the *Natural Sciences and Engineering Research Council of Canada* (NSERC). This support is greatly appreciated.

2.6 References

1. A. Abdel-Dayem and M. El-Sakka, "A Novel Morphological-based Carotid Artery Contour Extraction", *Canadian Conference on Electrical and Computer Engineering*, IEEE, pp. 1873-1876, 2004.
2. A. Abdel-Dayem and M. El-Sakka, and A. Fenster, "Watershed Segmentation for Carotid Artery Ultrasound Images," *International Conference on Computer Systems and Applications*, IEEE, pp. 131-139, 2005.
3. A. Abdel-Dayem and M. El-Sakka: "Carotid Artery Ultrasound Image Segmentation Using Fuzzy Region Growing," *International Conference on Image Analysis and Recognition*, pp. 869-878, 2005.
4. P. Abolmaesumi, M. Sirouspour and S. Salcudean, "Real-Time Extraction of Carotid Artery Contours from Ultrasound Images", *Computer Based Medical Systems 2000*, IEEE, pp.181-186, 2000.
5. A. Amini, S. Tenran, and T. Weymouth, "Using dynamic programming for minimizing the energy of active contours in the presence of hard constraints," *2nd International Conference of Computer Vision*, IEEE, pp. 95-99, 1988.
6. X. Bresson, P. Vandergheynst, J. Thiran. "A priori information in image segmentation: energy functional based on shape statistical model and image information," *International Conference on Image Processing*, IEEE, Vol 3 pp. 425-428, 2003.
7. J. Canny, "Finding lines and edges in images," *MIT*, 1983.
8. I. Cohen, "On active contour models and balloons," *Image Understanding*, vol. 53, pp. 211-218, 1991.
9. A. Hamou and M. El-Sakka, "A Novel Segmentation Technique For Carotid Ultrasound Images", *International Conference on Acoustics, Speech and Signal Processing*, IEEE, pp. 521-524, 2004.

10. S. Jespersen, M. Gronholdt, J. Wilhjelm, B. Wiebe, L. Hansen and H. Sillesen, "Correlation Between Ultrasound B-mode Images of Carotid Plaque and Histological Examination," *Ultrasonics Symposium*, IEEE, pp. 1065-1068, 1996.
11. M. Kass, A. Witkin, and D. Terzopoulos, "Snakes: active contour models," *1st International Conference on Computer Vision*, IEEE, pp. 259-268, 1987.
12. M. Leventon, W. Grimson, and O. Faugeras, "Statistical Shape Influence in Geodesic Active Contours," *Computer Vision and Pattern Recognition Conference*, IEEE, pp. 316-323, 2000.
13. F. Mao, J. Gill, D. Downey, A. Fenster, "Segmentation of Carotid Artery in Ultrasound Images", *Engineering in Medicine and Biology Society Conference*, IEEE, pp. 1734-1737, 2000
14. NASCET Team, "North American Symptomatic Carotid Endarterectomy Trial (NASCET)," *Stroke*, vol. 22 pp. 816-817, 1991.
15. J. Neyman and E.S Pearson, "On the Use and Interpretation of Certain Test Criteria for Purposes of Statistical Inference, Part I", *Joint Statistical Papers*, Cambridge University Press, pp.1-66, 1967 (originally published in 1928).
16. T. O'Donnell Jr, L. Erdoes; W. Mackey, J. McCullough, A. Shepard, P. Heggerick, J. Isner, and A. Callow, "Correlation of B-mode Ultrasound Imaging and Arteriography with Pathologic Findings at Carotid Endarterectomy," *Arch Surgery*, vol. 120 pp. 443-449, 1985.
17. A. Rosenfeld and J. Pfaltz. "Distance Functions in Digital Pictures," *Pattern Recognition*, vol. 1, pp 33-61, 1968.
18. J. Sethian, "Level set methods and fast marching methods: evolving interfaces in computational geometry," *Fluid Mechanics, Computer Vision, and Materials Science, Second edition*, Cambridge University Press, 1999.
19. C. Xu, "Deformable Models with Application to Human Cerebral Cortex Reconstruction from Magnetic Resonance Images", *Ph.D. Dissertation, Baltimore Maryland*, 1999.

Chapter 3 – Article 2

3 Active Contours with Optical Flow and Primitive Shape Priors for Echocardiographic Imagery^{*}

Abstract: Accurate delineation of object borders is highly desirable in echocardiography. Among other model-based techniques, active contours (or snakes) provide a unique and powerful approach to image analysis. In this work, we propose the use of a new external energy for a GVF snake, consisting of the optical flow data of moving heart structures (i.e. the perceived movement). This new external energy provides more information to the active contour model to combat noise in moving sequences. An automated primitive shape prior mechanism is also introduced, which further improves the results when dealing with especially noisy echocardiographic image cines. Results were compared with that of expert manual segmentations yielding promising sensitivities and system accuracies.

Keywords: Active contours, deformable models, snakes, gradient vector flow, shape priors, optical flow, echocardiography.

3.1 Introduction

Echocardiography, imaging the heart using ultrasound waves, has become the most widely used modality to observe heart motion and deformation over other modalities (e.g. Positron Emission computed Tomography, Cardiac Magnetic Resonance, Computer Tomography). This is due to the relatively inexpensive cost of the technology along with its non-invasive nature, yielding no known side-effects. Sophisticated enhancements to the acquisition devices over the years have yielded real-time dynamic observation of heart function.

^{*} A version of this chapter has been published: Ali K. Hamou and Mahmoud R. El-Sakka, “Active Contours with Optical Flow and Primitive Shape Priors for Echocardiographic Imagery”, International Conference on Imaging Theory and Applications (IMAGAPP), 2009, pp. 111-118.

Unfortunately, US data still suffers from speckle noise. It may also exhibit occluded borders due to the erratic scattering of its impinging waves (once it encounters various tissue densities). Efforts have been made to compensate for these shortcomings, including filtering [16] and incorporating the speckle noise effect directly into the algorithm [22]. Regardless, boundary detection techniques need to be employed in order to segment a region of interest (ROI). Analysis of these segmented regions has led to various works on endocardial borders [5], stress and strain of the septum [17], and wall motility [1], which all help to accurately diagnose cardiomyopathies.

Many computer vision techniques have been introduced in order to accomplish boundary detection. One such example is the active contour model, also commonly known as snakes [13].

Active contours treat the surface of an object as an elastic sheet that stretches and deforms when external and internal forces are applied to it. These models are physically-based, since their behavior is designed to mimic the physical laws that govern real-world objects [6]. Since this approach relied on variational calculus to find a solution, time complexity was a major drawback. Amini et al. [2] and Williams and Shah [23] proposed algorithms that reduced time complexity making the active contour model feasible for segmentation systems.

Issues with large capture ranges (the failure of curve migration when initialized distant from the ROI to segment) and concavities (high internal energies may inhibit the capture of smaller features) are solved by other advances, which include inflation forces [7], probabilistic models [15], oriented particles [21], and gradient vector flows (GVF) [24]. For the purposes of this study, focus will be placed on those advances best suited for echocardiographic images.

Since the left ventricle represents one of the most important heart functions, many semi-automatic techniques have attempted to segment this region from its surrounding tissue.

Papademetris et al. [19] proposed to measure the stress and strain of cardiac regional deformation of the left ventricle in ultrasound images by using a Markov random field [14]. Texture data was incorporated into their model for use with a tracking algorithm. However, assumptions of uncorrelated data within their model are made (which may lead to a

misclassification of structures due to noise) and complex calculations result in long computation times.

Eusemann et al. [8] proposed the use of a modality independent quantitative visualization of the peak velocities. Though set manually, the technique utilizes a set of polygon meshes to deform by means of the anatomical centerline of the left ventricle.

Jolly [12] proposed a semi-automatic segmentation algorithm with the use of three manually placed landmarks in order to estimate the location of various shape models. However, this system was designed for use on the end-systole and end-diastole images only, rather than the entire cardiac cycle.

Felix-Gonzalez and Valdes-Cristerna [9] proposed a technique using a series of standard algorithms (e.g. mean shift filtering, edge mapping, entropy extraction and confidence mapping) along with an active surface model in order to deal with the speckle. This model is made up of cubic splines and is based on gradient descent, however no explanation is given on parameterization and how the empirical data was set.

Zhou et al. [25] proposed the segmentation of MRI cardiac sequences using a generalized fuzzy GVF map along with a relative optical flow field. Optical flow measurements are computed on the cardiac sequence and a maximum a posteriori probability (MAP) is used as a window for the movement of the curve. The use of optical flow with GVF provides promising results, however since this technique is used exclusively on MRI data, there is no guarantee that it would work with US data given the presence of speckle noise.

In practice, many of the stated segmentation algorithms can be used on normal echocardiographic data. This is true given an adequate amount of user intervention and when such data exhibits low levels of speckle noise (i.e. from newer machines generally found in a research environment under ideal conditions with healthy volunteers). However in a clinical setting, the objective is to be able to accurately identify myocardial borders on problematic echocardiograms with minimal time.

In this paper, we will present an external energy for GVF snakes that takes advantage of the motion data within echocardiographic image cines. Furthermore, we incorporate the use of

primitive shape priors such that the contour placement will improve, especially when dealing with noisy regions and improper initialization.

The rest of the paper is organized as follows. Background information on relevant models will be briefly described in Section 2. The proposed scheme will be outlined in Section 3. Section 4 and Section 5 will contain the experimental results and conclusions, respectively.

3.2 Background

3.2.1 Active Contours

A snake is an energy minimization problem. Its energy is represented by two forces (internal energy, E_{in} , and external energy, E_{ex}) which work against (or independent of) each other. The total energy should converge to a local minimum; ideally at the desired boundary. A snake can be parametrically defined as $v(s) = [x(s), y(s)]^T$, where s belongs to the interval $[0,1]$. Hence, the total energy to be minimized, E_{AC} , to give the best fit between a snake and a desired object shape is:

$$E_{AC} = \int_0^1 E_{in}(v(s)) + E_{ex}(v(s)) ds \quad (1)$$

where E_{in} decreases as the curve becomes smooth and E_{ex} decreases as it approaches the ROI, such as image structures or edges (i.e. areas of high gradient information).

As in [13] the internal energy of the active contour formulation is further defined as:

$$E_{in}(v(s)) = \alpha(s) \times \left| \frac{dv}{ds} \right|^2 + \beta(s) \times \left| \frac{d^2v}{ds^2} \right|^2 \quad (2)$$

where $\alpha(s)$ and $\beta(s)$ are weighting factors of elasticity and stiffness, respectively. The first order term encourages the snake's surface to act like a membrane, whereas the second order term encourages the snake to act like a thin plate. $\alpha(s)$ controls the tension along the spine (stretching a balloon or elastic band) whereas $\beta(s)$ controls the rigidity of the spine (bending a thin plate or wire).

A typical external energy formulation for a given image, $I(x,y)$, to identify edges is:

$$E_{ex}(x, y) = -|\nabla I(x, y)|^2 \quad (3)$$

where ∇ denotes the gradient operator. In the case of a noisier image the edges are further smoothed:

$$E_{ex}(x, y) = -|\nabla[G_\sigma(x, y) * I(x, y)]|^2 \quad (4)$$

where $G_\sigma(x, y)$ is a two-dimensional Gaussian function with standard deviation σ , and $*$ denotes a convolution operator. σ must be large enough to compensate for the image noise that would interfere with the active contour's capture range (the contour may get trapped by the noisy areas of the image).

The standard snake algorithm suffers from poor range due to initialization and the inability to capture concavities. Xu and Prince [24] largely solved this problem by the advent of the GVF snake, which provides a field for guiding the contour to regions of high gradient. The GVF field is used as an external energy and is characterized by the vector field $z(x, y) = [u(x, y), v(x, y)]$ that minimizes the energy functional:

$$E_{GVF} = \iint \mu \times (|\nabla u|^2 + |\nabla v|^2) dx dy + \iint |\nabla f|^2 \times |z - \nabla f|^2 dx dy \quad (5)$$

where $f = -E_{ex}$ is an edge map derived from the image and μ is the degree of smoothness of the field. Figure 3-1 shows an example of a GVF field on a standard U-Image.

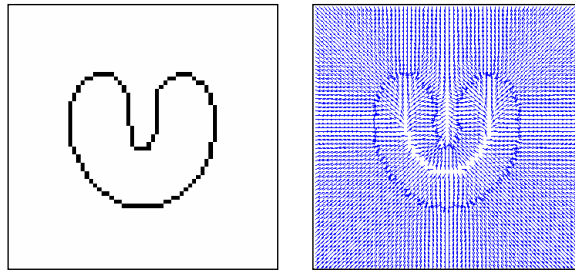


Figure 3-1: An example of the virtual electric field on standard U-Image.

3.2.2 Optical Flow

Optical flow approximates the apparent motion of an object over a series of images (or time). The relationship between the optical flow in the image plane and the velocities of objects in

the three-dimensional world is not necessarily obvious [3]. For the sake of convenience, most optical flow techniques consider a particularly simple world where the apparent velocity of brightness patterns can be directly identified with the movement of surfaces in the scene. This implies that objects maintaining structure with changing intensity would break this assumption.

Consider an image intensity, $I(x,y,t)$ at time t . Time, in this instance, implies that next frame in an image cine. Assuming that at a small distance away, and some time later the given intensity is:

$$I(x + \Delta x, y + \Delta y, t + \Delta t) = I(x, y, t) + \frac{\partial I}{\partial x} \Delta x + \frac{\partial I}{\partial y} \Delta y + \frac{\partial I}{\partial t} \Delta t + \text{higher order terms} \quad (6)$$

Given that the object started at position (x,y) at time t , and that it moved by a small distance of $(\Delta x, \Delta y)$ over a period of Δt , the following assumption can be made:

$$I(x + \Delta x, y + \Delta y, t + \Delta t) = I(x, y, t) \quad (7)$$

The assumption in (7) would only be true if the intensity of our object is the same at both time t and $t + \Delta t$. Furthermore, if our Δx , Δy and Δt are very small, our higher order terms would vanish:

$$\frac{\partial I}{\partial x} \Delta x + \frac{\partial I}{\partial y} \Delta y + \frac{\partial I}{\partial t} \Delta t = 0 \quad (8)$$

Hence dividing (8) by Δt will yield:

$$-\frac{\partial I}{\partial t} = \frac{\partial I}{\partial x} \frac{\Delta x}{\Delta t} + \frac{\partial I}{\partial y} \frac{\Delta y}{\Delta t} \quad (9)$$

$$-I_t = \frac{\partial I}{\partial x} u + \frac{\partial I}{\partial y} v, \quad (10)$$

where $u = \frac{\Delta x}{\Delta t}$ and $v = \frac{\Delta y}{\Delta t}$.

The equation in (10) is known as the optical flow constraint equation, where I_t at a particular pixel location, (x,y) , is how fast its intensity is changing with respect to time, u and v are the spatial rates of change for any given pixel (i.e. how fast an intensity is moving across an image). However, effectively estimating the component of the flow (along with intensity values) cannot directly be solved in this form since it will yield one equation per pixel for every two unknowns, u and v . In order to do so, additional constraints must be applied to this equation.

Horn and Schunck [11] introduced a method for solving this problem using partial derivatives. A global regularization constraint is used which assumes that images consist of objects undergoing rigid motion, and so over relatively large areas the optical flow will be smooth. Figure 3-2 depicts a visual representation of the optical flow of a simple Rubik's cube. Note that the grayscale image has few shadows. This helps to maintain consistency in the luminance of each pixel which in turn yields accurate results.

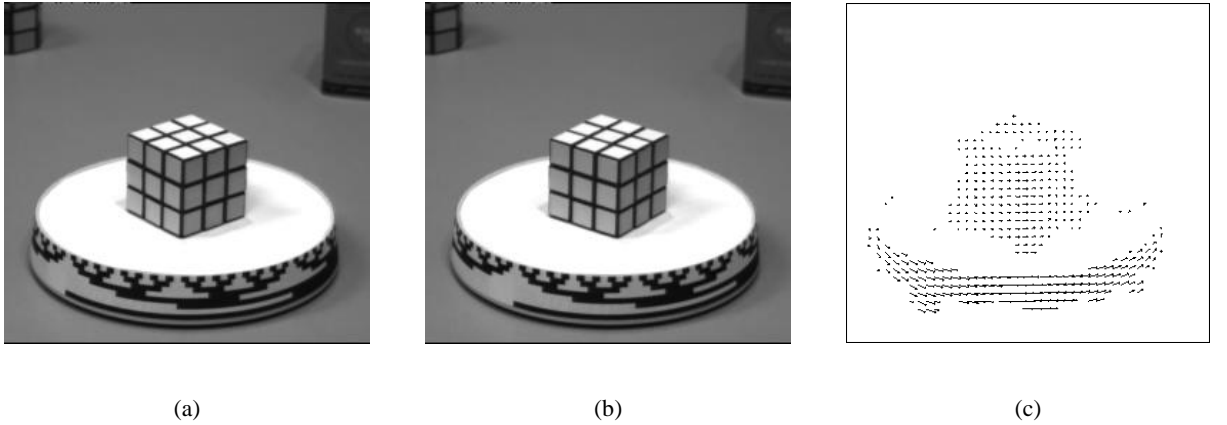


Figure 3-2: An example of an optical flow field on a Rubik's cube rotated image; (a) Rubik's cube at time t ; (b) Rubik's cube at time $t+\Delta t$; (c) optical flow.

3.3 Description of Proposed Model

The use of the GVF snake directly on echocardiograms will not provide an adequate solution due to the complication of noise and other valves that exist within the heart cavity. Hence our scheme will make use of a GVF snake with optical flow measurements. These measurements will be included in E_{GVF} .

By considering each image cine within an echocardiographic video loop, the Horn-Schunck technique [11] is applied in order to detect the motion between various heart structures. These optical flow measurements will further filter noise from the cines since speckle tends to be stable throughout an image. As such, noise will be assigned smaller magnitudes of movement over surrounding structures and hence will be eliminated.

The magnitude of these optical flow estimates are then median filtered and the canny edge map [4] is extracted in order to generate the GVF field for the snake's external energy.

Since the generation of the GVF field is computationally prohibitive using real world data, the external energy is generated using a *virtual electric field* (VEF) of the preprocessed edge map [20]. The VEF is defined by considering each edge as a point charge within an electric field. This can be accomplished by convolving the edge map with the following two masks:

$$g_x(x, y) = \frac{-x}{4\pi\epsilon \times (x^2 + y^2)^{3/2}} \quad (11)$$

$$g_y(x, y) = \frac{-y}{4\pi\epsilon \times (x^2 + y^2)^{3/2}} \quad (12)$$

where ϵ is sufficiently small. Given a sufficient mask size, the resulting field yields a vector flow identical to the GVF field defined in (5), without the high computational cost. For instance, the vector field shown in Figure 3-1 was generated with (11) and (12) with a mask size of 32.

Since many of the anatomical structures (such as the left ventricle of the heart) are known shapes and sizes, prior knowledge information can be directly used to increase the performance of a segmentation algorithm.

Priors based on shape statistical models require modifications to the standard active contour model. An iterative solution can be directly incorporated into any optimization model by using the proposed framework first outlined by [10].

Since it is desirable to incorporate shape priors into the model without directly involving the user,

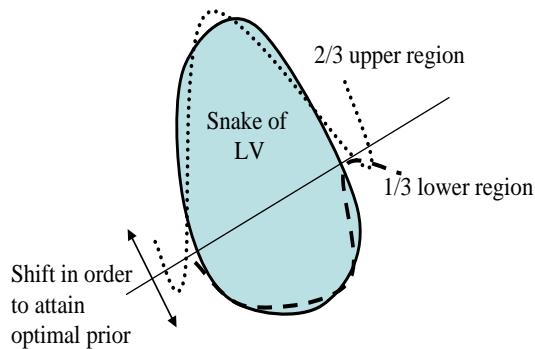


Figure 3-3: Generation of primitive priors on active contour points.

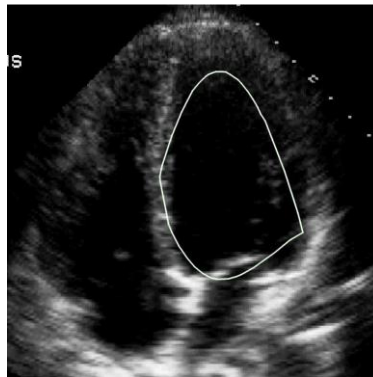


Figure 3-4: An example of a primitive prior formulation on the left ventricle.

automated shape detection takes place on the set of discrete snake points, $v(s)$. This is achieved by replacing E_{ex} of our active contour with a least squares fit polynomial (specifically a third order hyperbola) of the current $v(s)$ points. This allows the fitting of a primitive shape (or a series of primitives as needed for the left ventricle) to the curve set $v(s)$. This will help compensate for the noise that inhibits the snake from migrating past a certain point. The user is able to increase or decrease the effect of the prior knowledge to the snake's convergence cycle.

Depending on the feature of interest to be segmented, different primitive priors can be used in order to improve the robustness of the technique. The priors are not limited to hyperbolas; rather a range of shapes can be selected by the user in order to best fit their feature of interest. This is useful in the medical arena where a specialist has a clear understanding of the

underlying structure being detected, such as a liver, an artery, or a heart. A desired primitive shape can be selected before curve evolution takes place.

Figure 3-3 portrays the means of generating a primitive prior for the left ventricle of the 4 chamber view US heart image. The left ventricle points were split into an upper region and a lower region representing two separate shape fitting equations. This can be tuned to give the best prior by selecting the separation line of the regions with the least amount of distance between the fitted hyperbolas and snake curve. Further advantages are that the prior knowledge is not built on a set of training samples that are expert delineated; rather they are generated from the current active contour control points. Figure 3-4 shows the results of the prior generation scheme on an echocardiogram.

Once the prior is constructed, a VEF is generated of the prior and a single optimization iteration of the snake is executed before returning to the original optimization cycle. This is referred to as an *omega* iteration. This interruption to the snake optimization cycle is repeated throughout the snake's evolution, until it achieves equilibrium. A flow chart of the proposed scheme is shown in Figure 3-5.

3.4 Experimental Results

For this study, a series of B-mode echocardiogram cross sectional videos of the heart have been used to investigate the proposed snake algorithm. These videos were acquired using a SONOS 5500 by Philips Medical System. The transducer frequency was set at 2.5 Mhz in order to insure adequate penetration of tissue, while maintaining image quality with the existing speckle noise. Longitudinal views of the heart, which visualize the left ventricle, were acquired in order to verify the prior knowledge algorithm using more than one primitive shape.

The videos were parsed into image cines and each frame was considered with its direct neighbouring frame. Optical flow calculations for the edge map were completed using the Horn-Schunck technique with a regularization constraint of 0.05 in order to compensate for the general speckle throughout the US images. Mask size for VEF generation was set to 64 and was normalized for active contour use. The initial contour placement was set to a circle of radius 30, which was placed by the user within the left ventricle of the heart.

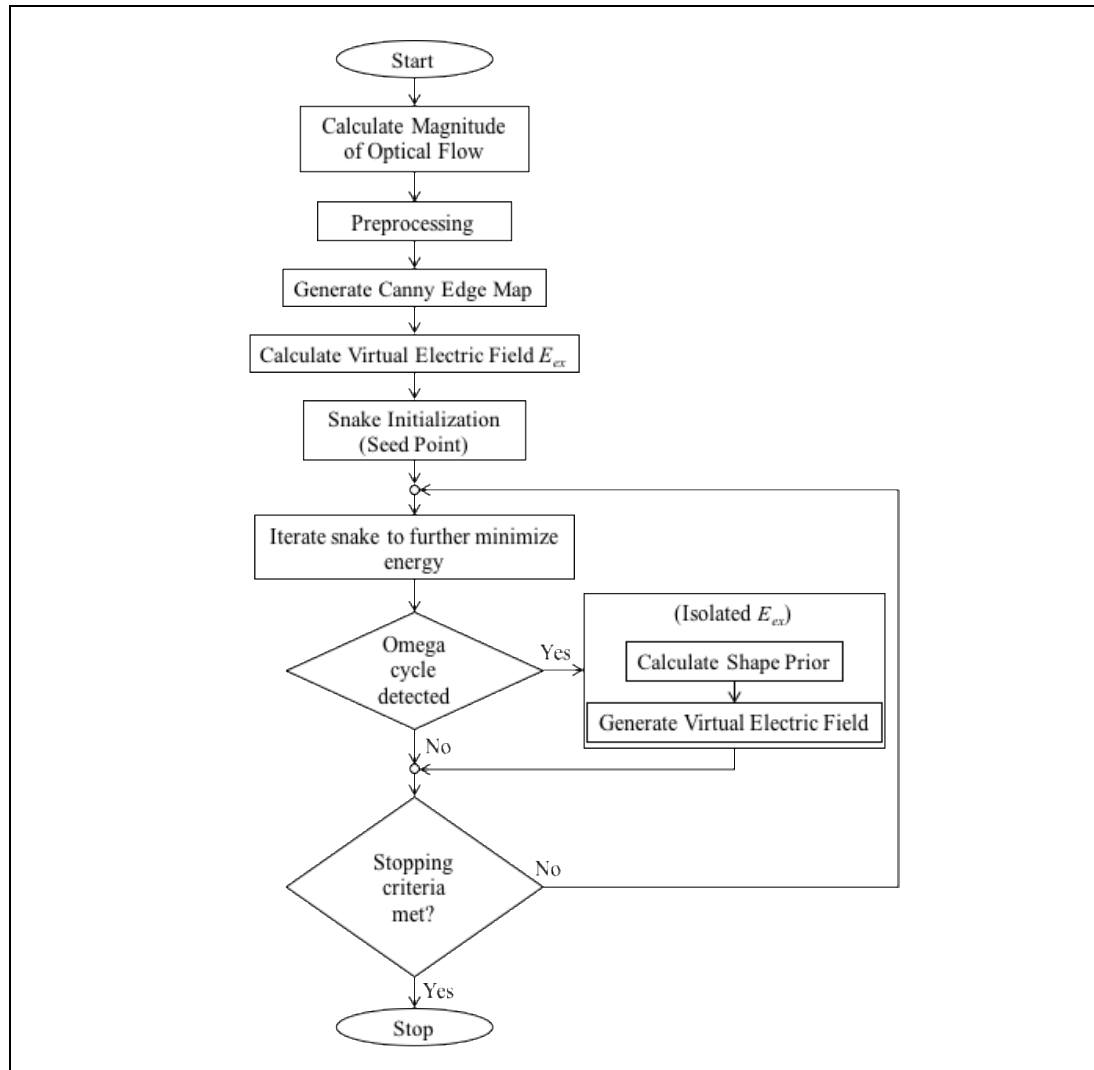


Figure 3-5: Flow Chart of Proposed Algorithm

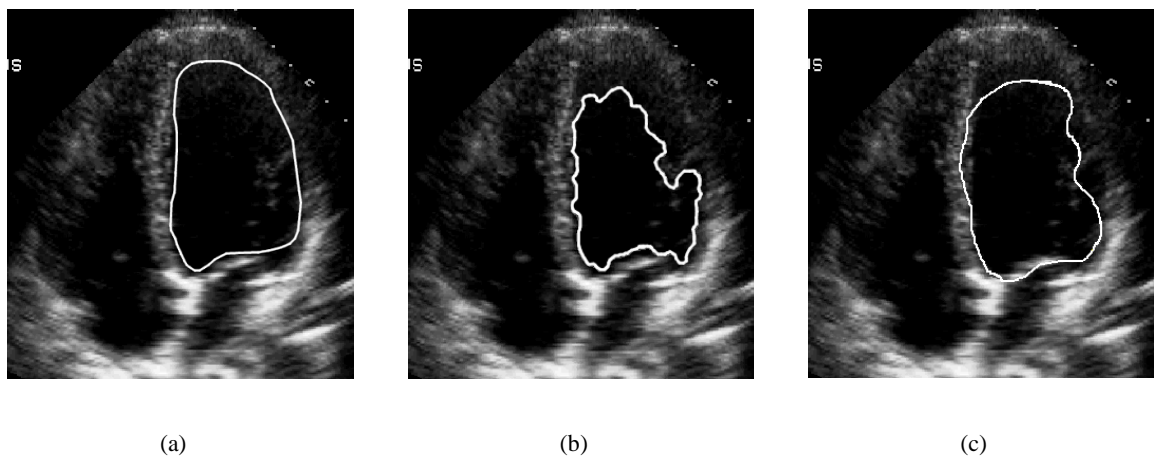


Figure 3-6: Segmenting the left ventricle of the heart (a) Expert manual segmentation (b) standard GVF segmentation (c) GVF-optical flow segmentation with priors.

Snake parameters, α and β , were set to 4 and 0, respectively. α was set to 4 in order to add a substantial amount of weight to the internal energy. β was set to 0 since the second order differential does not influence the snake enough to warrant the added time complexity. Priors (*omega* iteration) were invoked every five iterations of the snake minimization.

Figure 3-6(a) shows an expert manual segmentation of the left ventricle of the heart. Figure 3-6(b) shows the final contour using the traditional GVF snake. Figure 3-6(c) shows the final contour using the optical flow GVF snake with primitive priors. Expert examination of the results reveals that the shape priors improve regularity by allowing the snake to overcome noise, artifacts. This allows for proper delineation of the left ventricular endocardial lining. The optical flow measurements provide the necessary structural information used in the external energy of the snake.

Experiments were run on a complete cardiac cycle with various external energies. The first consisting purely of the optical flow measurements, the second on a combined energy of image gradient vectors and optical flow data.

Overall, accuracy of the proposed system was measured by comparing the 87 indexed images to the expert manual drawn segmentations by a clinician on the actual endocardial borders. These measurements include both type I and type II errors as defined by [18]. Since the images were mainly small segmented foregrounds against vast backgrounds, the system would best be measured by means of its sensitivity and system accuracy.

Sensitivity is the number of true positives divided by the number of true positives plus false negatives. System accuracy is the number of true positives and true negatives divided by the total number of pixels in the image. In other words, it classifies how accurate the results of the test are versus the total image.

The sensitivity of the system, given a 95% confidence interval, yields 0.568-0.610 when using the optical flow exclusively. However, this yield increased to 0.722-0.759 when combined with an image gradient vectors. Whereas, system accuracy, given the same confidence interval, yields 0.940-0.946 for the optical flow energy and 0.954-0.958 for the combined energy, respectively.

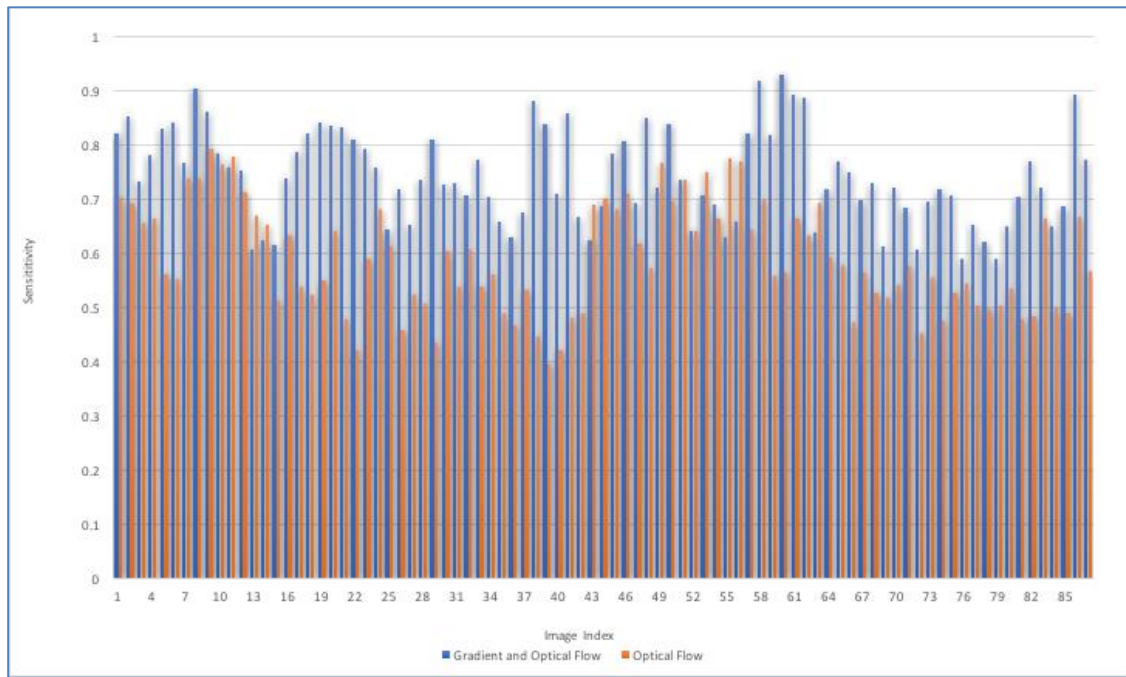


Figure 3-7: Sensitivity using different external energies

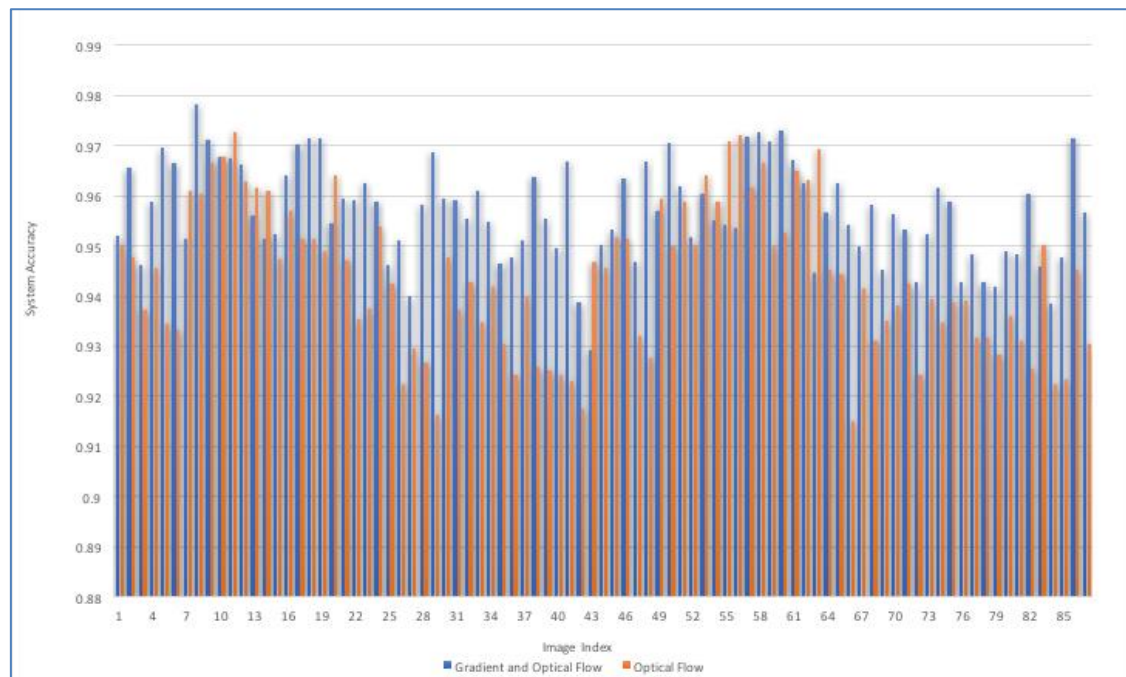


Figure 3-8: System Accuracy using different external energies.

Figure 3-7 shows the sensitivity of the system using various energies. Figure 3-8 shows the system accuracy of the system. We notice that there is a slight improvement when

segmenting using both the optical flow and the image gradient over the optical flow exclusively. This illustrates that the optical flow measurements contribute enough information to the snake in order to segment out the left ventricle.

3.5 Conclusions

In this paper, we have shown that the use of optical flow calculations can be used as an external energy within the GVF active contour framework. By exclusively using the optical flow calculations, we have shown that it is possible that an active contour method can make use of the knowledge derived from the apparent motion of tissue. This strengthens the principle that the movement of tissue masses should be considered within segmentation techniques, where the data facilitates it.

Furthermore, contour regularity and accuracy was improved by using primitive shapes priors. The inherent difficulties in segmenting echo-cardiographic images, such as avoiding speckle noise and valve interference were also overcome by the primitive priors. Results were validated against a gold standard which was manually segmented by a clinician.

3.6 Acknowledgements

This research is partially funded by the Natural Sciences and Engineering Research Council of Canada (NSERC). This support is greatly appreciated.

3.7 References

1. Amini, A., Radeva, P., Elayyadi, M. and Li, D. 1998, 'Measurement of 3D motion of myocardial material points from explicit B-surface reconstruction of tagged MRI data', *Medical Image Computing and Computer-Assisted Intervention*, pp. 110-118.
2. Amini, A., Weymouth, T., and Jain, R. 1990, 'Using dynamic programming for solving variational problems in vision', *IEEE Pattern Analysis in Machine Intelligence*, vol. 12, no. 9, pp. 855-866.
3. Barron, J., Fleet, D. and Beauchemin, D. 1994, 'Performance of optical flow techniques', *International Journal of Computer Vision*, vol. 12, no. 1, pp. 43-77.
4. Canny, J. 1986, 'A computational approach to edge detection', *IEEE Pattern Analysis in Machine Intelligence*, vol. 8, no. 6, pp. 679-698.
5. Choy, M. and Jin, J. 1996, 'Morphological image analysis of left ventricular endocardial borders in 2D echocardiograms', *SPIE Proceedings on Medical Imaging*, vol. 2710, pp. 852-864.

6. Cohen, I. 1991, 'On active contour models and balloons', *Image Understanding*, vol. 53, no. 2, pp. 211-218.
7. Cohen, L. and Cohen, I. 1993, 'Finite-element methods for active contour models and balloons for 2-d and 3-d images', *IEEE Transactions on pattern analysis and Machine Intelligence*, vol. 15, no. 11, pp. 1131-1147.
8. Eusemann C., Ritman E. and Robb R. 2002, '3D visualization of endocardial peak velocities during systole and diastole', *Medical Imaging: Physiology and Function from Multidimensional Images*, vol 4683, pp. 168-175.
9. Felix-Gonzalez, N. and Valdes-Cristerna R. 2006, '3D echocardiographic segmentation using the mean-shift algorithm and an active surface model', *SPIE Medical Imaging 2006: Image Processing*, vol. 6144, pp. 1314-1319.
10. Hamou, A., Osman, S. and El-Sakka, M., 2007, 'Carotid ultrasound segmentation using DP active contours', *International Conference on Image Analysis and Recognition*, vol. 4633, pp. 961-971.
11. Horn, B. and Schunck, B. 1981, 'Determining optical flow', *Artificial Intelligence*, vol. 17, pp. 185-203.
12. Jolly, M. 2006, 'Assisted ejection fraction in B-mode and contrast echocardiography', *Biomedical Imaging: Nano to Macro*, pp. 97-100.
13. Kass, M., Witkin, A. and Terzopoulos, D. 1988, 'Snakes: Active contour models', *International Journal of Computer Vision*, vol. 1, no. 4, pp. 321-331.
14. Kindermann, R and Snell, J. 1980, *Markov random fields and their applications*, American Mathematical Society, Providence, R.I.
15. Mallouche, H., de Guise, J. and Goussard, Y. 1995, 'Probabilistic model of multiple dynamic curve matching for A semitransparent scene', *SPIE Vision Geometry IV*, vol. 2573, pp. 148-157.
16. Mazumdar, B., Mediratta, A., Bhattacharyya, J. and Banerjee, S. 2006, 'A real time speckle noise cleaning filter for ultrasound images', *IEEE Symposium on Computer-Based Medical Systems*, pp. 341-346.
17. Montagnat, J. and Delingette, H. 2000, 'Space and time shape constrained deformable surfaces for 4D medical image segmentation', *Medical Image Computing and Computer-Assisted Intervention*, vol. 1935, pp. 196-205.
18. Neyman, J. and Pearson, E. 1928, 'On the use and interpretation of certain test criteria for purposes of statistical inference, part I', *Biometrika*, vol. 20a, no. 1/2, pp. 175-240.
19. Papademetris, X., Sinusas, A., Dione, D. and Duncan, J. 1999, '3D cardiac deformation from ultrasound images', *Medical Image Computing and Computer-Assisted Intervention*, vol. 1679, pp. 420-429.
20. Park, H. and Chung, M. 2002, 'A new external force for active contour model: virtual electric field', *Visualization, Imaging, and Image Processing*, vol. 364, pp. 90-94.
21. Szeliski, R. and Tonnesen, D. 1992, 'Surface modeling with oriented particle systems', *SIGGRAPH Computer Graphics*, vol. 26, no. 2, pp. 185-194.

22. Tauber, C., Batatia, H. and Ayache, A. 2008, 'Robust B-spline snakes for ultrasound image segmentation', *Springer Journal of Signal Processing Systems*.
23. Williams, D. and Shah, M. 1992, 'A fast algorithm for active contours and curvature estimation', *CVGIP: Image Understanding*, vol. 55, no. 1, pp. 14-26.
24. Xu, C. and Prince, J. 2000, 'Gradient vector flow deformable models', *Handbook of Medical Imaging*, pp. 159-159.
25. Zhou, S., Liangbin and Chen, W. 2004, 'A new method for robust contour tracking in cardiac image sequences', *IEEE Biomedical Imaging: Nano to Macro*, vol. 1, pp. 181-184.

Chapter 4 – Article 3

4 SRAD, Optical Flow and Primitive Prior based Active Contours for Echocardiography*

Abstract: Accurate delineation of object borders is a highly desirable in echocardiography, especially the left ventricle. Among other model-based techniques, active contours (or snakes) provide a unique and powerful approach to image analysis. In this work, we propose the use of a novel external energy for a gradient vector flow (GVF) snake. This energy consists of optical flow estimates of heart sequences along with the use of a speckle reducing anisotropic diffusion (SRAD) operator. This energy provides more information to the active contour model garnering adequate results for noisy moving sequences. Furthermore, an automatic primitive shape prior algorithm was employed to further improve the results and regularity of the snake, when dealing with especially speckle laden echocardiographic images. Results were compared with expert-defined segmentations yielding better sensitivity, precision rate and overlap ratio than the standard GVF model.

Keywords: Image segmentation, active contours, gradient vector flow, optical flow, shape priors, curve fitting, echocardiography.

4.1 Introduction

The assessment of cardiac function has been a major area of interest in the medical field. Normal heart function consists of pumping chambers (known as ventricles) which regulate the systemic and pulmonary circulation systems by delivering blood to the proper areas. Detection of non-normal heart function in the *left ventricle* (LV), for instance, can cause

* A version of this chapter has been published: Ali K. Hamou and Mahmoud R. El-Sakka, "SRAD, Optical Flow and Primitive Prior based Active Contours for Echocardiography", Computer Vision, Imaging and Computer Graphics. Theory and Applications. VISIGRAPP 2009. Communications in Computer and Information Science, 2010, Springer Berlin / Heidelberg, vol. 68, pp. 158-171.

systolic dysfunction, being the reduction in the ability to contract, or diastolic dysfunction, being the inability to fill efficiently. Various heart structures may also fail causing cardiomyopathies, endangering the life of the host individual. Fortunately, many myopathies are treatable (with medication, implanted pacemakers, defibrillators, or ventricular assist devices) given early detection. Echocardiography, imaging the heart using ultrasound waves, facilitates the ability to do so.

The advent of real time ultrasonography provides the ability to image an entire LV and surrounding anatomy within one cardiac cycle (approximately one second). However, depending on the patient's 'photogenicity' (impacting factors include surrounding fatty tissues, calcifications, gender), these images are most likely marred by speckle artifacts. Many computer vision techniques attempt to reduce such speckle noise by means of filtering [16] or incorporating the speckle effect directly into their algorithms [22]. Normally, these ultrasound images are analyzed for area and volume assessment by trapezoidal estimation. Such techniques introduce a large user bias into the calculations and are quite time consuming on the clinicians behalf. The advent of boundary detection techniques can help to automate this task. Boundary detection techniques are employed in order to segment the wanted regions for analyses on the heart structures, such as endocardial borders [5], stress and strain of the septum wall [17], and wall motility [1] to name a few.

Kass et al. [12] first proposed the original active contour model (commonly known as a snake or a deformable model). In their formulation, image segmentation was posed as an energy minimization problem.

Active contours treat the surface of an object as an elastic sheet that stretches and deforms when external and internal forces are applied to it. These models are physically-based, since their behaviour is designed to mimic the physical laws that govern real-world objects [6]. Since this approach relied on variational calculus to find a solution, time complexity was one of the main drawbacks of this original model. *Amini et al.* [2] proposed an algorithm for using dynamic programming, in order to incorporate soft and hard constraints into the formulation, improving time complexity and results. Further improvements to time complexity were proposed by *Williams et al.* [23], by using a greedy algorithm while incorporating a simple curvature approximation. Issues with large capture ranges and

concavities are solved by other advances, which include inflation forces [7], probabilistic models [15], oriented particles [21], and gradient vector flows [24]. For the purposes of this study, focus will be placed on those advances best suited for echocardiographic images.

Since the LV represents one of the most important heart functions, many semi-automatic techniques attempt to segment this region from surrounding tissues [5][7][18]. Yet, no universally accepted standard exists for segmenting echocardiographic images.

Papademetris et al. [18] took advantage of a b-splines parameterized deformable model for segmenting cardiac regions. The external energy consisted of the standard intensity term and a texture-based *markov random field* (MRF) term. The MRF is based on a combination of gradient, regional and curvature data computed from the original image. Initial contours are manually placed for each 2D plane and are passed to a shape tracking algorithm. Displacements are probabilistically computed using a confidence measurement for the entire set. Final displacements are fed into an anisotropic linear elastic model which is computed vis-à-vis a Bayesian estimation framework. The manual placement of the contours makes this technique quite labour intensive.

Felix-Gonzalez et al. [7] proposed a segmentation technique for echocardiographic images using an *active surface model* (ASM). The ASM is made up of cubic splines and is based on a gradient descent procedure. When using gradient descent, the empirical setting of parameters is required based on the quality and types of images used. This makes this proposed technique extremely sensitive to its input. Furthermore, *Felix-Gonzalez et al.*'s work was only tested on two limited datasets.

Leung et al. [13] proposed the use of an *active appearance model* (AAM) and intensity based registration for segmenting multiple 2D image slices. An AAM uses all the information in an image region covered by the target object, rather than just that near modeled edges. An AAM involves the principal component analysis of the various shapes and textures from several manually segmented 2D slices for training. The AAM makes use of the training set to converge the initial set mesh to the best textures on the image. However, this trained set required several manual segmentations of the 2D image slices to tune it to the medium being used.

The *gradient vector flow* (GVF) [24] snake was introduced as a modification to the original snake model in order to overcome the capture range and curve concavity issues. However, using the GVF snake directly on echocardiograms will not provide an adequate solution due to the complication of speckle noise and the existence of valves within the heart cavity, inhibiting a proper segmentation.

Zhou et al. [25] proposed the segmentation of MRI cardiac sequences using a generalized *fuzzy gradient vector flow* (FGVF) map along with a relative optical flow field. Optical flow measurements are computed on the cardiac sequence being considered and a *maximum a posteriori probability* (MAP) was used as a window for the movement of the curve. The use of optical flow with GVF provides promising results, however this technique is used exclusively on clear MRI data, and hence the presence of speckle noise on echocardiographic images would require modifications of this technique. Both GVF and optical flow measurements will be used in the proposed technique.

The proposed segmentation algorithm differs from previous works mainly in that it combines the benefits of multiple data sources within echocardiographic video cines. This includes the collection of motion data (helping to solve the static noise problem), localized detail data (helping to solve the inherent speckle noise problem), and structural data (helping to solve the occluded borders problem), which are represented by the optical flow module, the *speckle reducing anisotropic diffusion* (SRAD) edge map and the primitive priori knowledge module respectively.

The rest of this paper is organized as follows. In Section 4.2, the proposed scheme will be introduced. Results and discussion will be presented in Section 4.3, and Section 4.4 will contain conclusions.

4.2 System and Methods

In this study, we utilize and improve our previous preliminary works [8][9][10]. The proposed scheme will contain a fusion of knowledge about the image in order to improve the automation and inter-variable efficiency of left ventricular segmentation methods. The system will incorporate three distinct elements into the external energy of the active contour.

These elements are SRAD measurements, optical flow estimates and priori knowledge measurements on contour points.

4.2.1 Parametric Active Contour Review

A snake is an energy minimization problem. Its energy is represented by two forces (internal energy, E_{in} , and external energy, E_{ex}) which work against each other. The total energy should converge to a local minimum – in the perfect case – at the desired boundary. The snake is defined as $v(s) = [x(s), y(s)]^T$, where s belongs to the interval $[0,1]$. Hence, the total energy to be minimized, E_{AC} , to give the best fit between a snake and a desired object shape is:

$$E_{AC} = \int_0^1 E_{in}(v(s)) + E_{ex}(v(s)) ds \quad (1)$$

The internal energy decreases as the curve becomes smooth (by incorporating both elasticity and stiffness); whereas the external energy decreases as approaching the features of interest, such as image structures or edges.

The internal energy of the active contour formulation is further defined as:

$$E_{in}(v(s)) = \alpha(s) \left| \frac{dv(s)}{ds} \right|^2 + \beta(s) \left| \frac{d^2v(s)}{ds^2} \right|^2 \quad (2)$$

where $\alpha(s)$ and $\beta(s)$ are weighting factors of elasticity and stiffness terms, respectively. The first order term makes the snake's surface act like a membrane. The weight $\alpha(s)$ controls the tension along the spine (stretching a balloon or elastic band). The second order term makes the snake act like a thin plate. The weight $\beta(s)$ controls the rigidity of the spine (bending a thin plate or wire).

A typical external energy formulation to identify edges for a given image, $I(x,y)$, is:

$$E_{ex}(x, y) = -|\nabla I(x, y)|^2 \quad (3)$$

where ∇ denotes the gradient operator. In the case of a noisier image the edges are further smoothed:

$$E_{ex}(x, y) = -|\nabla(G_{\sigma}(x, y) * I(x, y))|^2 \quad (4)$$

where $G_{\sigma}(x, y)$ is a two-dimensional Gaussian function with standard deviation σ , and $*$ denotes a convolution operator. Since the contour may get trapped by the noisy areas of the image, σ must be large enough to compensate for the image noise that would interfere with the active contour's capture range. The standard snake algorithm also suffers from poor capture range due to initialization and the inability to capture concavities. These problems are largely solved by the advent of the GVF snake [24].

The concavity problem exists since the gradient vectors in an image generally have large magnitudes only in the immediate vicinity of the boundary, and are nearly zero at points further away from the boundary. As such, the capture range of the snake will be quite small. In order to resolve this, the gradient map is extended to points away from boundaries using a computational diffusion process. The GVF field is used as an external energy in the active contour and is characterized by the vector field $z(x, y) = [u(x, y), v(x, y)]^T$ that minimizes the energy functional [24]:

$$E_{GVF} = \iint \mu (|\nabla u|^2 + |\nabla v|^2) + |\nabla f|^2 |z - \nabla f|^2 dx dy \quad (5)$$

where f is an edge map derived from the image, μ is the degree of smoothness of the field, u and v characterize the direction and strength of the field. Hence, when $|\nabla f|$ is small the energy will be dominated by the partial derivatives, yielding a slow field. Alternatively, when $|\nabla f|$ is large, the latter term dominates and the function is minimized by setting $z = \nabla f$.

The external energy for the proposed scheme will be generated using a *virtual electric field* (VEF) [20] of f over the traditional GVF technique. Traditional GVF field generation is performed by optimizing the cost function represented as the different partials shown in (5), which is quite a time consuming process. The VEF is defined by considering each edge pixel as a point charge within an electric field. This can be accomplished by convolving the edge map with the following two masks:

$$g_x(x, y) = \frac{-c \cdot x}{(x^2 + y^2)^{3/2}} \quad (6)$$

$$g_y(x, y) = \frac{-c \cdot y}{(x^2 + y^2)^{3/2}} \quad (7)$$

where $c = (4\pi\varepsilon)^{-1}$ and ε is sufficiently small constant. The resulting field yields a vector flow identical to a GVF field; given the masks are of sufficient size. A smaller mask size would ignore outlying edges that would have little impact on the interested features since their range is quite far. However, since echoardiographic images contain many features throughout the image, quantizing any part of the edge map is not an option.

According to *Park et al.* [19], an area of radius 32 around the feature should provide adequate flow vectors to accurately recreate a GVF field, without suffering from the high computational cost associated with vector flow generation. Figure 4-1(b) shows an example of a vector flow field on the standard U-Image, shown in Figure 4-1(a), using 65×65 masks generated from (6) and (7), which is identical to the original GVF field.

4.2.2 SRAD Measurements

Diffusion is a process that equalizes differing concentrations without creating or destroying an object's mass. Simple diffusion can be defined as

$$\frac{\partial p^t}{\partial t} = \text{div}(D \cdot \nabla p^t) \quad (8)$$

where div is the divergence operator, D is the diffusivity tensor, and p refers to the diffused image at time point t . In *Perona and Malik's* anisotropic diffusion model [20], they defined D for smoothing image data as

$$D = g(\|\nabla p^t\|) = \frac{1}{1 + \left(\frac{\|\nabla p^t\|}{\lambda}\right)^2} \quad (9)$$

where λ is the edge magnitude parameter. Hence, $g(\cdot)$ will yield low values (near zero) for gradient values much greater than λ inhibiting diffusion near edges. Using (9) as the diffusivity coefficient of (8), the model sharpens edges if their gradient value is larger than the edge magnitude parameter λ by inhibiting diffusion. In other words, $g(\cdot)$ acts as a means to standardize edge response across homogeneous regions and non-homogeneous regions.

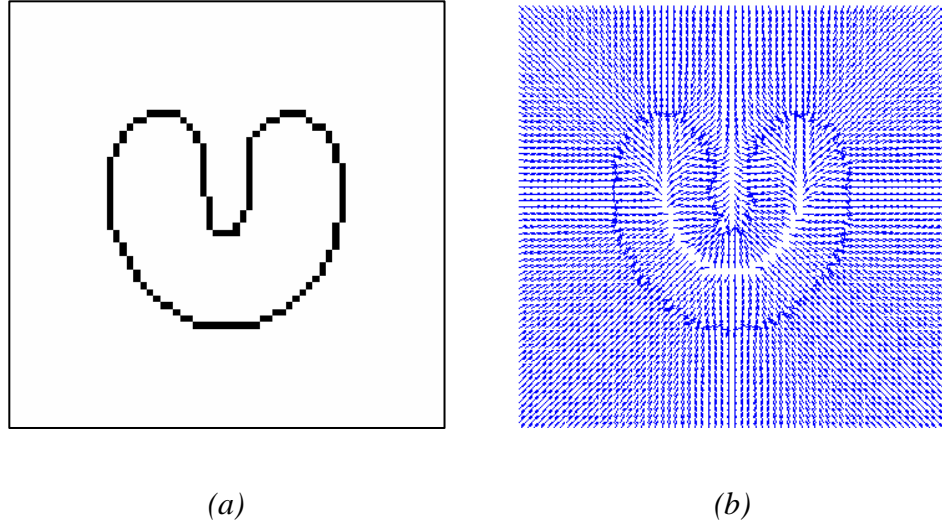


Figure 4-1: Example of gradient vector forces; (a) standard U-Image, and (b) Gradient Vector Flow of U-Image

Yu et al. [25] introduced the *instantaneous coefficient of variation* (ICOV) as a noise-estimating operator. The ICOV operator is defined by

$$ICOV(p') = \frac{\sqrt{\left| \frac{1}{2} \cdot \|\nabla p'\|^2 - \frac{1}{16} \cdot (\nabla^2 p')^2 \right|}}{(p' + 1/4 \cdot \nabla^2 p')} \quad (10)$$

where ∇^2 is the Laplacian operator. By combining the anisotropic diffusion model with the ICOV operator, *Yu et al.* [25] yielded a partial differential equation called the *speckle reducing anisotropic diffusion* (SRAD).

$$SRAD(p') = p^{t+\Delta t} = p' + \frac{\Delta t}{|\eta|} \cdot \text{div}(g(ICOV(p')) \cdot \nabla p') \quad (11)$$

where, $|\eta|$ is the number of pixels in the neighbourhood of pixel x (usually taken to be equal four). *Yu et al.* [26] showed that using (11) provided better results at detecting real borders when faced with high levels of speckle noise.

Applying SRAD on the echocardiograms will help to reduce much of the speckle that impedes the accurate calculation of optical flow, which will be incorporated into the external energy. SRAD edge-maps will also be fed as the gradient estimates for the snake.

4.2.3 Optical Flow Estimates

Optical flow approximates the apparent motion of an object over a series of images (or time). The relationship between the optical flow in the image plane and the velocities of objects in the three-dimensional world is not necessarily obvious [3]. For the sake of convenience, most optical flow techniques consider a particularly simple world where the apparent velocity of brightness patterns can be directly identified with the movement of surfaces in the scene. This implies that objects maintaining structure but changing intensity would break this assumption.

Consider an image intensity, $I(x,y,t)$ at time t . Time, in this instance, implies that next frame in an image cine. Assuming that at a small distance away, and some time later the given intensity is:

$$I(x + \Delta x, y + \Delta y, t + \Delta t) = I(x, y, t) + \frac{\partial I}{\partial x} \Delta x + \frac{\partial I}{\partial y} \Delta y + \frac{\partial I}{\partial t} \Delta t + \text{higher order terms} \quad (12)$$

Given that the object started at position (x,y) at time t , and that it moved by a small distance of $(\Delta x, \Delta y)$ over a period of time Δt , the following assumption can be made:

$$I(x + \Delta x, y + \Delta y, t + \Delta t) = I(x, y, t) \quad (13)$$

The assumption in (13) would only be true if the intensity of our object is the same at time t and $t + \Delta t$. Furthermore, if our $\Delta x, \Delta y$ and Δt are very small, our higher order terms would vanish, i.e.,

$$\frac{\partial I}{\partial x} \Delta x + \frac{\partial I}{\partial y} \Delta y + \frac{\partial I}{\partial t} \Delta t = 0 \quad (14)$$

Dividing (14) by Δt will yield:

$$-\frac{\partial I}{\partial t} = \frac{\partial I}{\partial x} \frac{\Delta x}{\Delta t} + \frac{\partial I}{\partial y} \frac{\Delta y}{\Delta t} \quad (15)$$

$$-I_t = \frac{\partial I}{\partial x} u + \frac{\partial I}{\partial y} v, \quad \text{where } u = \frac{\Delta x}{\Delta t} \text{ and } v = \frac{\Delta y}{\Delta t}. \quad (16)$$

Equation (16) is known as the optical flow constraint equation, where I_t at a particular pixel location, (x,y) , is how fast its intensity at this location is changing with respect to time, u and v are the spatial rates of change for any given pixel (i.e., how fast an intensity is moving across an image). However, effectively estimating the component of the flow (along with intensity values) cannot directly be solved in this form since it will yield one equation per pixel for every two unknowns, u and v . In order to do so, additional constraints must be applied to this equation.

Lucas-Kanade [14] and *Horn-Schunck* [11] introduced two common methods for solving this problem using partial derivatives. The former assumes that the flow field is locally smooth (for a given static window size) and then solves (16) by means of a least squares approximation technique. The latter uses a global regularization parameter which assumes that images consist of objects undergoing rigid motion, resulting in a smooth optical flow over a relatively large area. Figure 4-2 depicts a visual representation of the optical flow of a simple Rubik's cube. Notice that the greyscale image has few shadows, helping to maintain consistency in the luminance of each pixel, hence yielding accurate results.

When dealing with noisy echocardiograms, a global regularization parameter will deal with the speckle better than the static window. This is due to the speckle noise remaining relatively static, lacking fluidity, throughout an image. Hence, the speckle will be 'filtered', since the optical flow calculations will fail to realize it within the frames.

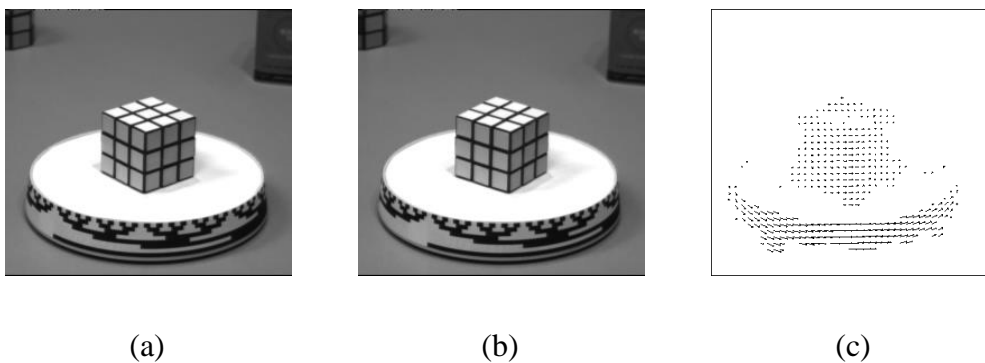


Figure 4-2: An example of an optical flow field on a Rubik's cube rotated image; (a) cube at time t , (b) cube at time $t + \Delta t$, and (c) Optical flow of image (a) to (b) using Lucas-Kanade method (originally published in *Barron et al.* [3]).

Optical flow magnitudes will be combined with the SRAD edge maps (see Section 4.2.5), in order to generate the external energy in (1) of the GVF snake. This will help to reduce artifacts due to static speckle noise, while also providing more information for the contour points to track (i.e., the movement of the tissue mass).

4.2.4 Primitive Shape Measurements on Contour Points

Since we are dealing with structures that have known shapes and sizes, and many real-world models have been already measured, prior knowledge information can be directly used to increase the performance of a segmentation algorithm. Priors based on shape statistical models require modifications to the standard active contour model. An iterative solution can be incorporated directly into any optimization model by using the proposed framework.

Since it is desirable to incorporate shape priors without directly involving the user for training, automatic shape detection takes place on the set of discrete snake points, $v(s)$. This is achieved by first generating the least squares fit polynomial(s) of the current $v(s)$ points. For our left ventricle application, snake points were divided into an upper region and a lower region representing two separate third-order hyperbolas, which will better suit the shape of the left ventricle during both systole and diastole, though any shape prior can be represented by means of simple primitives. Least squares fitting technique is utilized to estimate the two hyperbolas coefficients. The axis separating the two regions is computed by taking the two-thirds upper and one-third lower bounds on all snake points and computing their division. This division can be tuned by shifting it upwards or downwards (either manually by the user or automatically by the system) in order to minimize the distance between the fitted hyperbolas and snake points.

Priors are then generated by joining the fitted primitives to form one solid shape. Primitives are bounded by the furthest easterly and westerly points by the snake points, in order to prevent the possibility of a non-connecting shape.

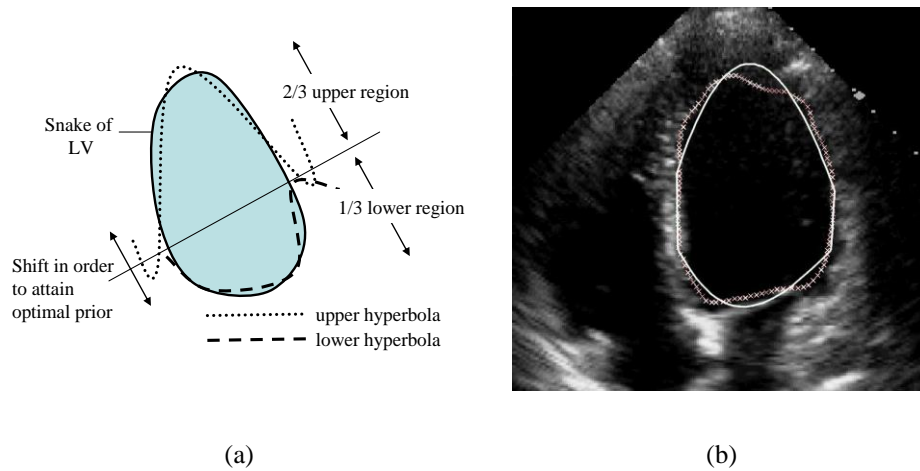


Figure 4-3: Left ventricle primitive shape fitting; (a) primitive shape fitting algorithm using two hyperbolas, and (b) echocardiogram with segmentation overlay; solid line represents primitive whereas X-line represents active contour

Once priors have been generated, its GVF field is computed. This new field will replace the existing external energy of the GVF snake for this specific snake iteration. Figure 4-3 portrays the process of generating a primitive prior for the left ventricle of the 4-chamber view image, where two intersecting hyperbolas are used (default shape for our left ventricle application).

The fitting of a primitive shape (or a series of primitives as needed for the left ventricle) to the snake points, $v(s)$, will help compensate for the noise that inhibits the snake from migrating past a certain point. It will also help retract the snake towards the primitive prior when an occluded border exists; common in many echocardiographic images. The user can control the number of cycles between any two consecutive prior calculation cycles (prior step parameter). This allows for the increase or decrease in the inherent effect of the prior knowledge to the snake's convergence cycle.

This primitive prior module is useful in the medical arena where the specialist or clinician has a clear understanding of the underlying structure being detected, such as a liver, an artery, or a heart. They can choose their desired primitive shape (or series of shapes) before curve evolution takes place.

4.2.5 Fusion Characteristics

The proposed external energy is a fusion of SRAD gradient edge-map information and the optical flow estimates. Figure 4-4 illustrates a top-level block diagram of the proposed system. It starts by calculating the SRAD edge map of the image cines (as explained in Section 4.2.2). The edge maps optical flows are then extracted (as explained in Section 4.2.3). The estimated optical flow is median filtered and are added to the SRAD image edge map following normalization. This result is used to generate the GVF for the snake's external energy. GVF snake evolution (as explained in Section 4.2.1) iterates to further minimize the energy function until a prior cycle condition is satisfied (as explained in Section 4.2.4), at which, the prior cycle is initiated. During the prior cycle, a GVF is generated from the desired primitive and a single optimization evolution of the snake is executed before returning to the original non-primitive snake iterations. This process is repeated until the snake is optimized and equilibrium is achieved.

4.3 Results and Discussion

For this study, a series of B-mode echocardiogram cross-sectional videos of the heart have been used to investigate the proposed snake algorithm. These videos were acquired using a SONOS 5500 by Philips Medical System. The transducer frequency was set at 2.5 MHz in order to insure adequate penetration of tissue, while maintaining image quality with the existing speckle noise. Longitudinal views of the heart, which visualize the left ventricle, were acquired in order to verify the prior knowledge algorithm using more than one primitive shape.

The videos were parsed into image cines and each frame was considered with its direct neighbouring frame. Optical flow calculations for the edge map were completed using the Horn-Schunck technique with a regularization constraint of 0.2 in order to compensate for the general speckle throughout the US images. The initial contour placement was set to a small circle which was placed by the user within the left ventricle of the heart and the prior step parameter was set to 5 cycles.

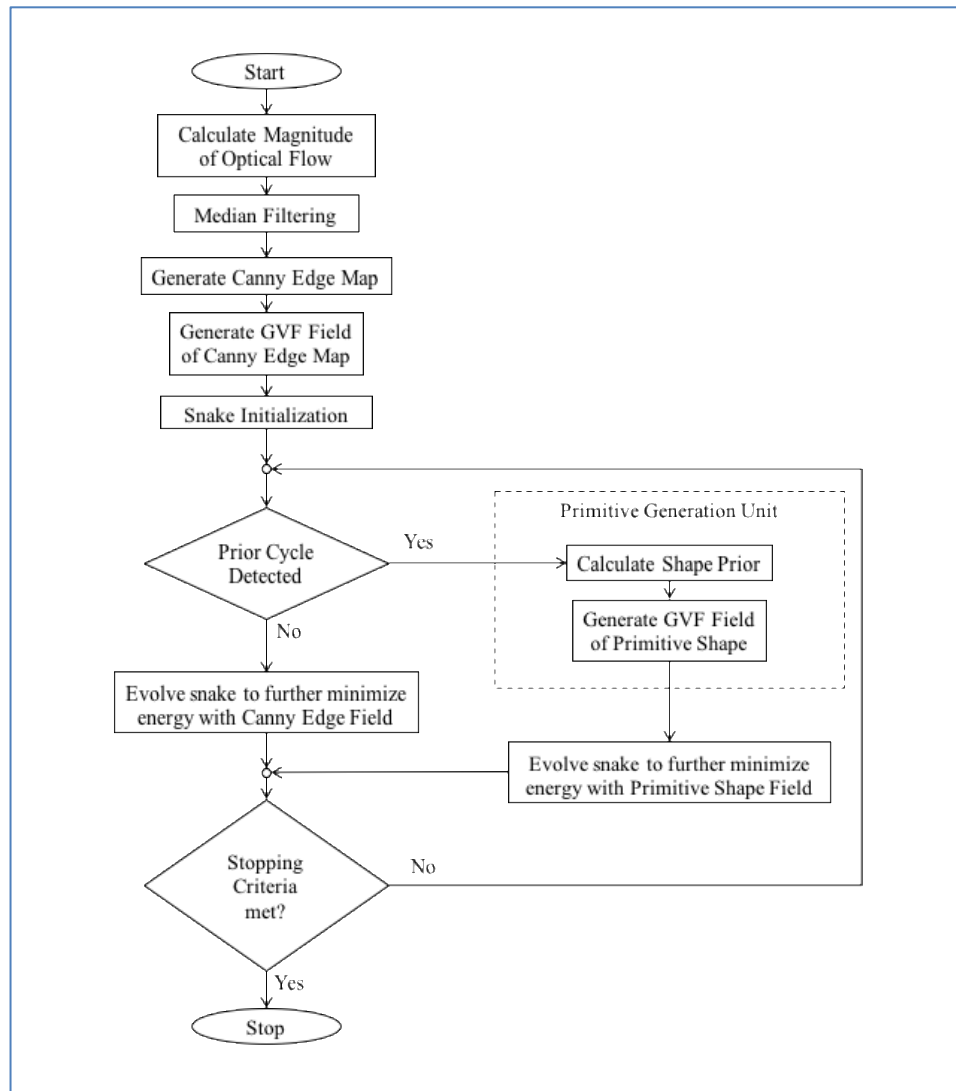


Figure 4-4: Top level block diagram of proposed scheme

Overall, experiments were run on eight complete cardiac cycles from different patients. The performance of the proposed system was measured by comparing 130 indexed segmented image cines from the eight cardiac cycles to the manually delineated segmentations by an expert radiologist, representing the gold standard used. Since the images at hand were mainly small-segmented foregrounds (left ventricular surface area) against vast backgrounds, the system performance would best be measured by means of its sensitivity, precision rate and overlap ratio. Let us consider the following metrics; a true positive pixel is a pixel that is considered part of the left ventricle by both of the proposed method and the gold standard. A false positive pixel is a pixel that is considered part of the left ventricle by the proposed

method but it is not considered as such on the gold standard. A false negative pixel is a pixel that is not considered as part of the left ventricle by the proposed method, yet it is considered to be part of the ventricle according to the gold standard. The sensitivity is the percentage of the number of true positive pixels divided by the sum of the number of true positive pixels and false negative pixels. In other words, it classifies how well a binary classification test correctly identifies a condition.

Precision rate is the percentage of the number of true positive pixels divided by the sum of the number of true positive pixels and false positive pixels. In other words, it classifies how accurate the results of the test when the results are positive. Overlap ratio is the percentage of the number of true positive pixels divided by the sum of the number of true positive pixels, false positive pixels and false negative pixels.

The sensitivity, precision rate and overlap ratio of the proposed system on the 130 segmented cines are shown in Table 4-1. This was generated by combining the total metric aggregates across all 130 cines, and calculating the sensitivity, precision rate and overlap ratio measures. Examination of Table 4-1 shows that the proposed technique outranks the standard GVF snake in all of the metrics shown.

Table 4-1: Sensitivity, precision rate and overlap ratio of the proposed system

	Sensitivity	Precision Rate	Overlap Ratio
Standard GVF Snake	90.4%	70.2%	65.3%
GVF Snake with SRAD	92.9%	77.4%	73.0%
Optical flow and priors			

An example of segmentation results is exhibited in Figure 4-5, where Figure 4-5(b) reveals the SRAD contours used in the external energy of the proposed scheme, Figure 4-5(c) shows the expert manually traced delineation of the left ventricle, (d) shows the segmentation results when utilizing GVF only, and Figure 4-5(e) reveals the segmentation results when utilizing the proposed scheme. As seen in Figure 4-5 (e), the shape priors improve regularity by allowing the snake to overcome various noise artifacts. This allows for proper delineation of the left ventricular endocardial lining. Furthermore, the motion information (optical flow) is used as structural information in the external energy of the snake.

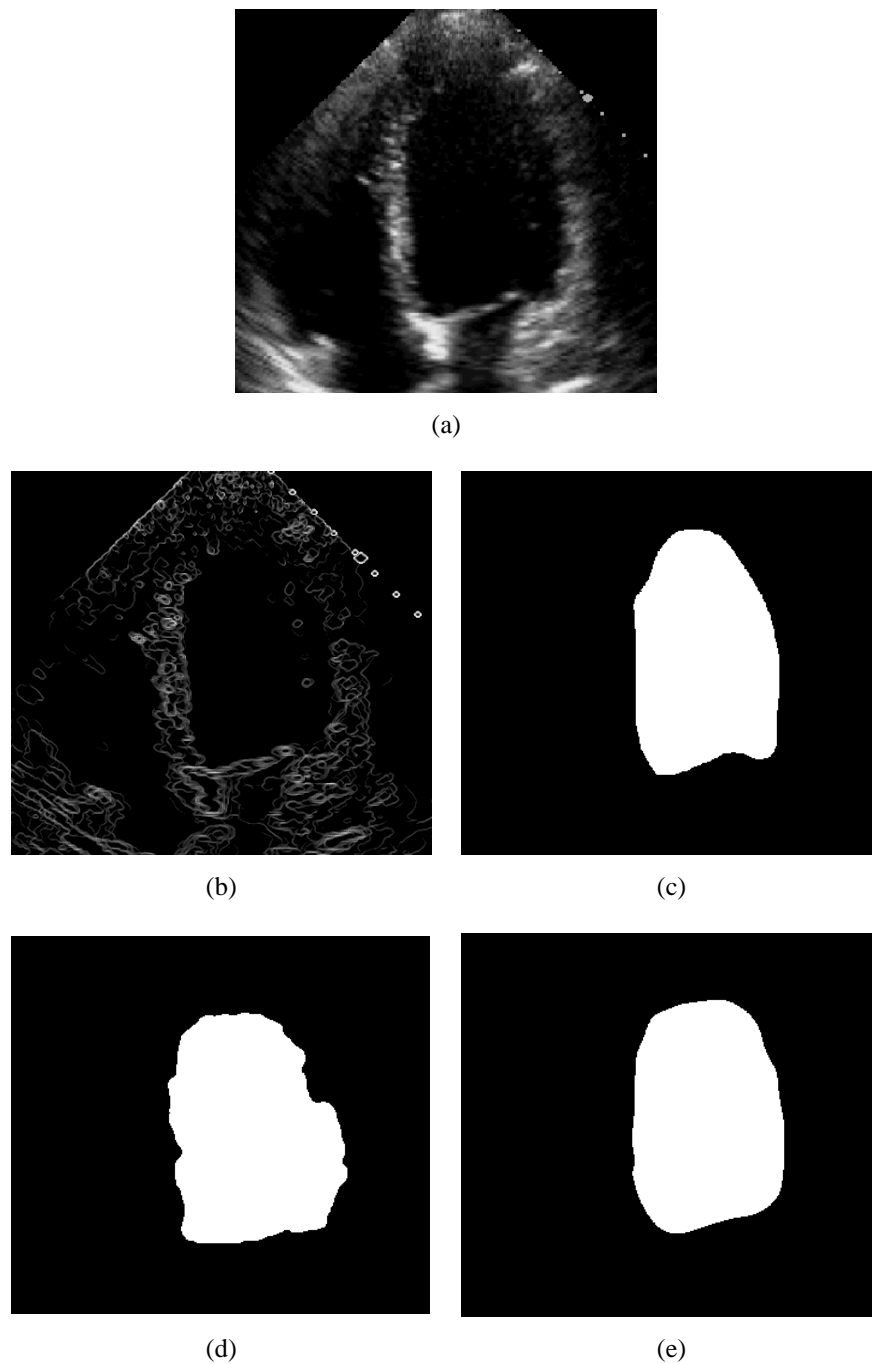


Figure 4-5 Segmentation results; (a) LV echocardiogram, (b) SRAD diffusion of image (a), (c) manual expert delineation of image (a), (d) and (e) segmentations when utilizing GVF only and when utilizing the proposed scheme, respectively.

4.4 Conclusions

In this work, we have shown that the use of optical flow estimations and SRAD diffusion techniques perform well when integrated with a GVF active contour. This scheme helped alleviate the inherent difficulties in segmenting echocardiograms, such as considering speckle noise and contour bleeding. Furthermore, it strengthens the principle that tissue movement should be considered within segmentation techniques, where the data facilitates it.

Contour regularity and accuracy were further improved by using primitive shapes priors. The inherent difficulties in segmenting echocardiographic images, such as avoiding speckle noise and valve interference were also overcome by the primitive priors. Results were validated against a gold standard, which was manually segmented by a clinician and yielded stronger results than the standard GVF snake in sensitivity, precision rate and overlap ratios. Such segmentations would improve the calculation of various clinical measures by reducing the inconsistencies and variability between clinicians while simultaneously reducing the time for clinician interaction.

4.5 Acknowledgements

This research is partially funded by the Natural Sciences and Engineering Research Council of Canada (NSERC). This support is greatly appreciated.

4.6 References

- 1 Amini, A., Radeva, P., Elayyadi, M., Li, D. "Measurement of 3D motion of myocardial material points from explicit B-surface reconstruction of tagged MRI data", Int. Conf. on Medical Image Computing and Computer Assisted Intervention, LNCS vol. 1496, pp. 110-118, 1998.
- 2 Amini, A., Weymouth, T and Jain, R. "Using dynamic programming for solving variational problems in vision", IEEE Trans. on Pattern Analysis in Machine Intelligence, vol. 12(9), pp. 855-866, 1990.
- 3 Barron, J., Fleet, D., and Beauchemin, D. "Performance of optical flow techniques", Int. J. of Computer Vision, vol.12(1), pp. 43-77, 1994.
- 4 Choy, M. and Jin, J. "Morphological image analysis of left ventricular endocardial borders in 2D echocardiograms", SPIE Proceedings on Medical Imaging, vol. 2710, pp. 852-864, 1996.
- 5 Cohen, L. "On active contour models and balloons", Computer Vision, Graphics, and Image Processing: Image Understanding, vol. 53(2), pp. 221-218, 1991.

- 6 Cohen, L. and Cohen, I. "Finite-element methods for active contour models and balloons for 2-D and 3-D images", *IEEE Trans. on Pattern Analysis and Machine Intelligence*, vol. 15(11), pp. 1131-1147, 1993.
- 7 Felix-Gonzalez, N. and Valdes-Cristerna R. "3D echocardiographic segmentation using the mean-shift algorithm and an active surface model", *Medical Imaging, SPIE* vol. 6144, pp. 147-151, 2006.
- 8 Hamou, A. and El-Sakka, M. "An SRAD and optical flow based external energy for echocardiograms", *Int. Conf. of Image Processing*, 2009.
- 9 Hamou, A. and El-Sakka, M. "Active contours with Optical Flow and Primitive Shape Priors for echocardiographic Imagery", *Int. Conf. of Imaging Theory and Applications*, pp. 111-118, 2009.
- 10 Hamou, A., Osman, S., and El-Sakka, M. "Carotid ultrasound segmentation using DP active contours", *Int. Conf. on Image Analysis and Recognition, LNCS* vol. 4633, pp. 961-971, 2007.
- 11 Horn, B. and Schunck, B. "Determining optical flow", *Artificial Intelligence*, vol. 17, pp. 185-203, 1981.
- 12 Kass, M., Witkin, A. and Terzopoulos, D. "Snakes: active contour models", *Int. J. of Computer Vision*, vol. 1(4), pp. 321-331, 1987.
- 13 Leung, K., van Stralen, M., van Burken, G., Voormolen, M., Nemes, A., ten Cate, F., de Jong, N., van der Steen, A., Reiber, J. and Bosch, J. "Sparse appearance model based registration of 3D ultrasound images", *Medical Imaging and Augmented Reality, LNCS* vol. 4091, pp. 236-243, 2006.
- 14 Lucas, B. and Kanade, T. "An iterative image registration technique with an application to stereo vision", *Proceedings of Imaging Understanding Workshop*, pp. 121-130, 1981.
- 15 Mallouche, H., de Guise, J. and Goussard, Y. "Probabilistic model of multiple dynamic curve matching for a semitransparent scene", *Vision Geometry IV*, vol. 2573, pp. 148-157, 1995.
- 16 Mazumdar, B., Mediratta, A., Bhattacharyya, J. and Banerjee, S. "A real time speckle noise cleaning filter for ultrasound images", *IEEE Symposium on Computer-Based Medical Systems*, pp. 341-346, 2006.
- 17 Montagnat, J. and Delingette, H. "Space and time shape constrained deformable surfaces for 4D medical image segmentation", *Medical Image Computing and Computer-Assisted Intervention, LNCS* vol. 1935, pp. 196-205, 2000.
- 18 Papademetris, X., Sinusas, A., Dione, D., and Duncan, J. "3D cardiac deformation from ultrasound images", *Medical Image Computing and Computer-Assisted Intervention, LNCS* vol. 1679, pp. 420-429, 1999.
- 19 Park, H. and Chung, M. "A new external force for active contour model: virtual electric field", *Int. Conf. on Visualization, Imaging and Image Processing*, pp. 103-106, 2002.
- 20 Perona, P. and Malik, J. "Scale space and edge detection using anisotropic diffusion", *IEEE Trans. Pattern Analysis Machine Intelligence*, vol. 12(7), pp. 629-639, 1990.

- 21 Szeliski, R. and Tonnesen, D. "Surface modeling with oriented particle systems", SIGGRAPH: Computer Graphics, vol. 26(2), pp. 185-194, 1992.
- 22 Tauber, C., Batatia, H. and Ayache, A. "Robust B-spline snakes for ultrasound image segmentation", J. of Signal Processing Systems, vol. 54(1), pp. 159-169, 2009.
- 23 Williams, D. and Shah, M. "A fast algorithm for active contours and curvature estimation", Computer Vision Graphics and Image Processing: Image Understanding, vol. 55(1), pp. 14-26, 1992.
- 24 Xu, C. and Prince, J. "Snakes, shapes, and gradient vector flow", IEEE Trans. on Image Processing, vol. 7(3), pp. 359-369, 1998.
- 25 Yu, Y. and Acton, S. "Speckle reducing anisotropic diffusion", IEEE Trans. on Image Processing, vol. 11(11), pp. 1260-1270, 2002.
- 26 Yu, Y. and Acton, S. "Edge detection in ultrasound imagery using the instantaneous coefficient of variation", IEEE Trans. on Image Processing, vol. 13(12), pp. 1640-1655, 2004.
- 27 Zhou, S., Liangbin, Chen, W. "A new method for robust contour tracking in cardiac image sequences", IEEE Int. Symposium on Biomedical Imaging: Nano to Macro, vol. 1, pp. 181-184, 2004.

CLINICAL SCIENCES

Chapter 5

5 Clinical Sciences Introduction

"Clinical informaticians transform health care by analyzing, designing, implementing, and evaluating information and communication systems that enhance individual and population health outcomes, improve patient care, and strengthen the clinician-patient relationship."

Gardner RM et al. Core Content for the Subspecialty of Clinical Informatics

My journey continues onward.

Clinical Informatics is also sometimes referred to as health informatics. [1] It is the study and use of data and information technology to deliver health care services and to improve the patients' ability to monitor and maintain their own health. This results in the definition of new clinical practice guidelines and support for all clinicians, patients, and caregivers.

This field encompasses a wide array of research sub-categories, including:

- Various methods to collect, store, and analyze health care data
- The study of information needs and cognitive processes
- Clinical decision support, including summarization, visualization, and provision of evidence in novel ways
- Information flow and workflow optimization
- Policy creation for information infrastructure, together with privacy and security
- Integration of systems and optimal solutions within healthcare facilities.

Statistical modeling methods were used in the presented clinical research methodologies. Of these, the following are the most relevant to the presented integrated articles:

Cluster analysis [2][3][4] or clustering is the task of grouping a set of objects in such a way that objects in the same group (called a cluster) are more similar (in some sense or another) to each other than to those in other groups (clusters).

Decision tree learning [5] uses a decision tree as a predictive model which maps observations about an item (represented in the branches) to conclusions about the item's target value (represented in the leaves). It is one of the predictive modelling approaches used in statistics, data mining and machine learning.

Markov model [6] is a stochastic model used to model randomly changing systems where it is assumed that future states depend only on the current state not on the events that occurred before it (that is, it assumes the Markov property). Generally, this assumption enables reasoning and computation with the model that would otherwise be intractable.

Stratification [7] is the process of dividing members of the population into homogeneous subgroups before sampling. Each subgroup (or strata) should be mutually exclusive: every element in the population must be assigned to only one stratum. The strata should also be collectively exhaustive: no population element can be excluded.

I have selected four integrated articles in order to expose some of my clinical research publications. In the previous chapters, I improve algorithms via novel pipelines to help identify segments of an image, in these clinical articles, I create novel pipelines to improve models for disease prediction and discovery.

In the first integrated article, which has been cited 8 times as of the submission of this thesis, “Cluster Analysis of MR Imaging in Alzheimer’s Disease using Decision Tree Refinement” [8], the use of novel analytical techniques (such as data clustering and decision trees) that can model and predict patient disease outcomes is presented. This has great potential for assessing disease process and progression in Alzheimer’s disease (AD) and mild cognitive impairment (MCI). For this study, 124 different variables (generated from image data, demographics and data) have been compiled and analyzed using a modified clustering algorithm – by linking variable distance to outcomes. The testing samples included 112 healthy controls, 122 MCI patients, and 120 AD patients. Our aim was to determine the influence of these variables on the incidence of Alzheimer’s and mild cognitive impairment.

Furthermore, we used a decision tree algorithm to model the level of “importance” of variants influencing this decision. These models demonstrate the influence and importance of clinical, biomarker imaging and neuropsychological variables on the patient’s long-term health.

In the second integrated article, which has been cited 2 times as of the submission of this thesis, “A Markov Analysis of Patients Developing Sepsis using Clusters” [9], presents predictive algorithms determining which patients are more likely to develop sepsis, in which early treatment can potentially reduce their risks. This is difficult since there is no “standard” presentation of sepsis, despite many published definitions of this condition. In this work, data from a large observational cohort of patients (4196 patients were randomly selected) – with variables collected at varying time periods – are observed in order to determine whether sepsis develops or not. A cluster analysis approach is used to form groups of correlated data points. This sequence of data points is then categorized on a per person basis and the frequency of transitioning from one grouping to another is computed. The result is posed as a Markov model which can accurately estimate the likelihood of a patient developing sepsis. A discussion of the implications and uses of this model is presented.

In the third integrated article, “A Disease Registry and Disease Management System for Patients with Malignant Melanoma” [10], a unique longitudinal tracking system for the treatment and outcome management for patients with melanoma is presented. The system’s design was informed by healthcare providers, a review of existing systems and published literature. Strategies and interventions designed to better understand melanoma can help reduce the risk and rate of the disease. Current registries and information systems are generic in nature and not tailored to a specialist’s workflow or clinic needs. Efficient data collection systems and application of effective workflow models can lead to significant improvements in quality of healthcare. Several modules have been established to address the concerns of the healthcare clinic, including: patient demographics, imaging, patient surveys, security, reporting and analysis. This framework is capable of displaying disease imaging screens, visually and interactively tracking melanoma sites, automatically computing staging scores, and tracking all surgeries and outcomes. Conditional patient access provides an interactive model of care to the clinic.

Finally, in the last integrated article, “Burden of illness for metastatic melanoma in Canada: 2011–2013” [11], a detailed epidemiology for patients with advanced metastatic melanoma in Canada was presented based on the data collection system presented above. The aim of this study was to demonstrate the presentation, disease characteristics, course, and treatment patterns for malignant melanoma patients. We used data collected via the Canadian Melanoma Research Network (CMRN) Patient Registry. We identified patients who were seen at one of 3 cancer treatment centres between April 2011 and April 30, 2013. A cohort of 810 patients with melanoma was identified from the CMRN registry. The mean age was 58.7 years and the majority were male (60% vs 40%). Factors impacting survival included having unresectable or metastatic melanoma, initial stage at diagnosis, presence of brain metastasis, and BRAF mutation status. The proportion of surviving patients decreased with higher initial disease stages. Using the CMRN registry, we were able to determine detailed epidemiology of patients with melanoma in Ontario, validating the comprehensive and detailed information that can be obtained from these data when using efficient data collection.

This selection of works concludes my clinical research component and has provided me with a window to continue future research studies in the realm of informatics.

5.1 Selection of Papers

The selection of these works demonstrates a progression from dealing with algorithmic techniques and pipelines for improving the modeling and prediction of diseases. It progresses and culminates in the collection of datasets and leveraging them for external parties to do additional research. I have included some of the citations for these integrated articles, though some of which have not been published long enough to be widely cited or leveraged. The expectation of providing a data collection platform that houses granular and longitudinal data sets (as in article 6) sets the stage for further research by external parties along with the continued development of novel techniques and trend discovery for healthcare improvement.

Though the datasets leveraged in the following clinical articles contained medical images from various modalities, the analyses were conducted on a full range of the available dataset, including demographics, genetic, biomarker, etc. This allowed my algorithmic pipelines to encapsulate a greater range of information when modelling outcomes.

Article 4 provides my first view into clinical datasets, I developed a model and analysis pipeline for Alzheimer's disease which was used by other research students within the lab. In order to validate the model, it was applied to a sepsis dataset, which is represented in Article 5. However, this second dataset was riddled with missing data, incomplete timelines and erroneous segments. In order to accommodate the data and the desired output the model was modified and generalized. Once I realized that clinical datasets were not being collected efficiently, I partook in building an informatics toolkit in order to provide longitudinal datasets to other researchers, depicted in Article 6. Article 7 demonstrates some of the data trends and outcomes generated from the collected datasets. This data has been leveraged by at least three other research associates and will grow as the data becomes more complete and robust.

5.2 References

1. Mettler T, Raptis DA. "What constitutes the field of health information systems? Fostering a systematic framework and research agenda", *Health Informatics Journal*. 2012, vol. 18(2), pp. 147-56.
2. Tryon, Robert C. "Cluster Analysis: Correlation Profile and Orthometric (factor) Analysis for the Isolation of Unities in Mind and Personality", *Edwards Brothers*, 1939.
3. Haldar, P., et al. "Cluster Analysis and Clinical Asthma Phenotypes", *American Journal of Respiratory and Critical Care Medicine*, 2008, vol. 178(3), pp. 218-224.
4. Macedo, Luciana G., et al. "Nature and Determinants of the Course of Chronic Low Back Pain Over a 12-Month Period: A Cluster Analysis", *Physical Therapy*, 2014, vol. 94(2), pp. 210-221.
5. Rokach, Lior; Maimon, O. "Data mining with decision trees: theory and applications", *World Scientific Pub Co Inc*, 2008.
6. Baum, L. E.; Petrie, T. "Statistical Inference for Probabilistic Functions of Finite State Markov Chains", *The Annals of Mathematical Statistics*, 1966, vol. 37(6), pp. 1554-1563.
7. Salant, Priscilla, I. Dillman, and A. Don. "How to conduct your own survey", 1994.
8. Ali Hamou, Michael Bauer, Benoit Lewden, Andrew Simmons, Yi Zhang, Lars-Olof Wahlund, Catherine Tunnard, Iwona Kloszewska, Patrizia Mecozzi, Hilkka Soininen, Magda Tsolaki, Bruno Vellas, Sebastian Muehlboeck, Alan Evans, Per Julin, Niclas Sjögren, Christian Spenger, Simon Lovestone, Femida Gwadry-Sridhar, and other participants in the AddNeuroMed consortium, "Cluster Analysis and Decision Trees of MR Imaging in Patients Suffering Alzheimer's", *Trends in Practical Applications of Agents and Multiagent Systems, Advances in Soft Computing*, 2010, vol. 71, pp. 477-484.
9. Femida Gwadry-Sridhar, Michael Bauer, Benoit Lewden, Ali Hamou. "A Markov Analysis of Patients Developing Sepsis Using Clusters", *Knowledge Representation for*

- Health-Care. KR4HC 2010. Lecture Notes in Computer Science, Springer. 2011*, vol. 6512, pp. 85-100.
10. Ali Hamou, Stacey Guy, Alexandria Ratzki-Leewing, Jesse O'Brien, Femida Gwadry-Sridhar, "A Disease Registry and Disease Management System for Patients with Malignant Melanoma", *AHIC – Advances in Health Informatics Conference*, 2012, 4 Pages.
 11. Scott Ernst, Teresa Petrella, Anthony Joshua, Ali Hamou, Marroon Thabane, Sharon Vantyghem, & Femida Gwadry-Sridhar. "Burden of illness for metastatic melanoma in Canada, 2011–2013". *Current Oncology*, 2016, vol. 23(6), pp. 563-570.

Chapter 6 – Article 4

6 Cluster Analysis of MR Imaging in Alzheimer’s Disease using Decision Tree Refinement*

Abstract: The use of novel analytical techniques (such as data clustering and decision trees) that can model and predict patient disease outcomes has great potential for assessing disease process and progression in Alzheimer’s disease and mild cognitive impairment. For this study, 124 different variables (generated from image data, demographics and data) have been compiled and analyzed using a modified clustering algorithm. Our aim was to determine the influence of these variables on the incidence of Alzheimer’s and mild cognitive impairment. Furthermore, we used a decision tree algorithm to model the level of “importance” of variants influencing this decision.

Keywords: Alzheimer's Disease, Mild Cognitive Impairment, Cluster Analysis, Decision Tree Analysis, MRI

Subject Classification Numbers: CCS-H.3.3, CCS-J.3

6.1 Introduction

Mild cognitive impairment (MCI) may be defined as a transitional state between normal aging and *Alzheimer’s disease* (AD) in which memory impairment is greater than expected for age, but general cognitive function and daily living activities are preserved [12]. The rate of progression from MCI to dementia is considerable according to estimates from several

* A version of this chapter has been published: Ali Hamou, Michael Bauer, Benoit Lewden, Andrew Simmons, Yi Zhang, Lars-Olof Wahlund, Catherine Tunnard, Iwona Kloszewska, Patrizia Mecozzi, Hilkkä Soininen, Magda Tsolaki, Bruno Vellas, Sebastian Muehlboeck, Alan Evans, Per Julin, Niclas Sjögren, Christian Spenger, Simon Lovestone, Femida Gwady-Sridhar, and other participants in the AddNeuroMed consortium, “Cluster Analysis and Decision Trees of MR Imaging in Patients Suffering Alzheimer’s”, Trends in Practical Applications of Agents and Multiagent Systems, Advances in Soft Computing, 2010, vol. 71, pp. 477-484.

longitudinal studies: 12% per year for 4 years [12], 40% over 2 years [8], 53% over 3 years [10], 34%–100% over 4–5 years [1, 9], and 100% over 9.5 years [11]. Currently, there is much debate over whether MCI is a separate nosological entity at increased risk of dementia or is an early symptom of AD [15]. Regardless, it is important to develop tools that enable us to predict conversion from MCI into progressive dementia.

The early detection and management of this disorder is important due to the recent availability of drug therapies for mild-to-moderate AD. As therapies with the potential to arrest the progression of Alzheimer’s disease are being developed, identification of people with pre-Alzheimer conditions has become increasingly important to determine whether such individuals can benefit from pharmacologic and non-pharmacologic interventions.

Unfortunately, once fully developed, AD is a devastating illness with a long drawn-out course that results in a diminished quality of life for patients and their caregivers. Treatment strategies targeting the most susceptible individuals (either primary or secondary prevention) are urgently needed. These strategies can provide a means of delaying the progression of the disease to those that are at risk of converting from MCI to AD. Developing analytic tools to support these goals is in the interest of the patient, health care provider and payers, as well as research and development in the pharmaceutical industry. In order to refine treatment strategies and establish early markers of disease, it is important to differentiate features that are prevalent in AD and MCI.

This work deals with the use of modeling techniques to classify patients as AD and MCI, which will improve clinical outcomes by providing an early assessment of potential AD patients. This assessment can change the treatment plans of such patients, which could impact the long-term progression of AD or MCI. Section 2 describes the systems, methods and approaches used in detail and describes implications of the proposed model. Section 3 describes the analysis used on the datasets and Section 4 concludes and summarizes this work.

6.2 Systems and Methods

In order to address these goals, data from the AddNeuroMed study^{*}, (which had institutional review board approval), was used to accurately model AD and MCI. A rich imaging dataset was available, which provided efficacy data and optimized patient selection. Data was collected at baseline (time of recruitment) and then at three month and 12 months follow up visits. In this paper, we describe the methodology used to differentiate patients at baseline.

6.2.1 Dataset Source

AddNeuroMed, a European AD biomarker study, aimed to perform a multi center MRI study similar to that of a drug trial. MRI scans were collected and evaluated at a data coordination centre (DCC) and were correlated to data from other sources (i.e. clinical datasets, data from blood samples, etc). The clinical centers that participated in this study were King's College London, University of Thessaloniki, University of Kuopio, University of Perugia, Medical University of Lodz and University of Toulouse. The DCC was the Karolinska Institutet in Stockholm.

Data management, image quality control and workflow control were guided by the Loris database platform (originally developed at McGill Brain Imaging Centre), and were further customized in this work. Patients were selected based on criteria that established whether they had MCI, AD or neither (i.e. controls). Patients were selected at each of the above centres, and were continuously sampled until the accrual goals were met. Accrued subjects consisted of a balanced sample with 112 healthy control, 122 MCI patients and 120 AD patients.

6.2.2 Tissue Classification and Regional Segmentation

MRI data acquisition took place using six different 1.5T MR systems (4 General Electric, 1 Siemens and 1 Picker). At each site a quadrature birdcage coil was used for RF transmission and reception. Data acquisition was designed to be compatible with the Alzheimer Disease Neuroimaging Initiative (ADNI) [6]. The imaging protocol included a high resolution sagittal

^{*} This study was funded by the European Union of the Sixth Framework program priority FP6-2004-LIFESCIHEALTH-5, Life Sciences, Genomics and Biotechnology for Health.

3D T1-weighted MPRAGE volume (voxel size: $1.1 * 1.1 * 1.2 \text{ mm}^3$) and axial proton density / T2-weighted fast spin echo images. The MPRAGE volume was acquired using a custom pulse sequence specifically designed for the ADNI study to ensure compatibility across scanners [16,17]. Full brain and skull coverage was required for both of the latter datasets and detailed quality control carried out on all MR images [16,17].

We adopted a three-stage approach to quality control. First, MRI scans were regularly acquired at each of the sites using a urethane test object known as a phantom. A phantom design developed by the U.S.-based ADNI consortium was used, which allows precise quantification of the geometric accuracy of a scan, together with other quality control measures, including signal-to-noise ratio and image uniformity using the ImageOwl web-based automated quality control system (<http://www.imageowl.com>) to ensure good performance of each of the scanners during the duration of the study. Second, two volunteers were scanned at each site, and their images were processed using the same analysis tools as the cohort images to ensure compatibility of data [16,17]. Finally, the MRI sites and data coordination center worked closely together with continuous feedback as data was acquired. All MRI centers were trained to perform quality control at their site at the time the images were acquired with particular emphasis on full brain coverage, image wrap around, subject motion artifacts, contrast between gray and white matter, and image nonuniformities [16,17]. All scanners remained within specification for the ADNI phantom throughout the course of the study. The coefficient of variation for whole brain measures for the two volunteers scanned at each of the sites was 1.7% and the mean (sd) of the coefficients of variation for the smaller anatomical regions reported in this paper was 3.4 (1.9)%.

All MR images received a clinical read by an on-site radiologist in order to exclude any subjects with non-AD related pathologies such as brain tumors.

A highly automated structural MRI image processing pipeline which was developed by Fischl and his colleagues was utilized for data analysis [3, 4, 5]. It produced both regional cortical thickness measures and regional volume measures.

Cortical reconstruction and volumetric segmentation included removal of non-brain tissue using a hybrid watershed/surface deformation procedure, automated Talairach transformation, segmentation of the subcortical white matter and deep gray matter volumetric

structures (including hippocampus, amygdala, caudate, putamen, ventricles) intensity normalization, tessellation of the gray matter white matter boundary, automated topology correction, and surface deformation following intensity gradients to optimally place the gray/white and gray/cerebrospinal fluid borders at the location where the greatest shift in intensity defines the transition to the other tissue class. Surface inflation was followed by registration to a spherical atlas which utilized individual cortical folding patterns to match cortical geometry across subjects and parcellation of the cerebral cortex into units based on gyral and sulcal structure.

6.2.3 Variables

The T1 weighted images were used to measure structural changes in the brain. A total of 51 regional volumetric and 70 regional cortical thickness measures were determined. All volumetric measures were normalized by dividing by the intracranial volume. Together with age, gender and the e4 version of the APOE gene (a risk factor for Alzheimer's disease) this yielded 124 variables which were used for the proposed analysis. Table 1 summarises the demographics of the three groups (Alzheimer's disease, mild cognitive impairment and controls).

6.3 Analysis

A cluster analysis algorithm was used in order to determine whether or not partitions, representing AD or MCI states, within the AddNeuroMed dataset could be identified and modeled for subsequent decision making. This technique was further refined using decision trees in order to enhance the cluster predictor.

6.3.1 Cluster Analysis

Cluster analysis, or clustering, is the assignment of a set of observations into subsets (called clusters) such that observations in the same cluster are of similar kind and grouped into respective categories. Clustering is a method of unsupervised learning, and a common technique for statistical data analysis. The clustering method used in this work was developed to serve two purposes, the first was to expose the importance of each variable with respect to the decision making process on the disease. The second was to provide a means of

discovering, given the preliminary image data results, whether or not a subject was likely to have MCI or AD based on cluster belongingness.

A variety of different clustering sizes and algorithms were explored. Empirically, the number of clusters chosen was 12 – resulting in clusters that were neither too large to manage (over fitted), nor ones with too few data points to give an adequate determination of patient status due to lack of separation. A modified k-means clustering algorithm was used in this work due to its speed of execution on large datasets. This algorithm incorporates both the internal consistency of variables within the cluster (distance to the cluster's centroid) and the external distance to all neighboring clusters as its heuristic. The k-means algorithm used is refinement iterative and alternates between assignment (where each variable is assigned to a cluster) and updating (calculation of new means of the cluster centre). By doing so, clusters will eventually incorporate all variables within the closest proximity space.

During cluster generation, the algorithm is applied to every variable within the dataset. Variables are then ranked by influence and probability of defining a cluster and its location within the cluster field (internal consistency measure). Following cluster creation, the cluster fields are grouped based on the internal consistency of the variables within each cluster. The mathematical indicator used to create these groupings is defined as the orthogonal distance between clusters [14].

Since we know whether a patient belongs to the control, MCI or AD group, this information (which is not used in cluster creation) is used to validate the biological plausibility of the separation, in other words, test the cluster field specificity. Hence, the cluster field can be used in order to determine which variable belongs to a respective group, given an internal consistency measure.

Figure 6-1(a) displays a cluster field using the proposed technique with belongingness to the groups indicated by colour. This was generated by using all of the variables (126 for the AddNeuroMed study) available. This technique leads to nicely separated clusters, however there is overlap between groupings (where primary red represents control, primary green represents MCI, and primary blue represents AD). This is evident in Figure 6-1(a), since the colours shown have amalgamated at various places within the proximity space. This is known as grouping overlap within the clusters, and hence makes it difficult to accurately

define what a cluster truly represents – rendering decision making complicated. Accurate variable selection can lead to better defined clusters with less overlap in groupings. Since the grouping results are known, a series of principal component analysis could be used to refine the variables used. Though, since the ultimate goal of the cluster analysis is decision making, decision trees are a more efficient means of refining this process to gain greater precision or sensitivity.

6.3.2 Decision Trees

In order to determine which variables contribute to a higher internal consistency within a cluster (i.e. the belongingness of a cluster to one outcome versus another), a decision tree algorithm was used.

A decision tree is a predictive model, that is, a mapping from observations about an item resulting in conclusions about its target value [13]. In these tree structures, leaves represent classifications and branches represent conjunctions of features that lead to those classifications. A decision tree is made from a succession of nodes, each splitting the dataset into branches. Generally, the algorithm begins by treating the entire dataset as a single large set and then proceeds to recursively split the set. Three popular rules are typically applied in the automatic creation of classification trees. The Gini rule splits off a single group of as large a size as possible, whereas the entropy and two-ing rules find multiple groups comprising as close to half the samples as possible. The algorithms construct the tree from the “top” down until some stopping criterion is met. In our current approach, we have used the gain in entropy, which accurately models the physical system evolving spontaneously toward equilibrium, in order to determine how to best create each node of the tree.

In order to define information gain precisely, we used a measure called entropy, that characterizes the “purity” (or, conversely, “impurity”) of an arbitrary collection of examples. Generally, given a set S , containing only positive and negative examples of some target concept (the so-called two-class problem), the entropy of set S relative to this simple, binary classification is defined as:

$$Entropy(S) = - p_p \log_2 p_p - p_n \log_2 p_n \quad (1)$$

where p_p is the proportion of positive examples in S and p_n is the proportion of negative examples in S .

Given that entropy is a measure of the impurity in a collection of training examples, we can then define the effectiveness of an attribute in classifying the data. The measure we will use, called information gain, is simply the expected reduction in entropy caused by partitioning the examples accordingly. More precisely, the information gain, $Gain(S, A)$ of an attribute A , relative to a collection of examples S , is defined as:

$$Gain(S, A) = Entropy(S) - \sum_{v \in values(A)} \frac{|S_v|}{|S|} Entropy(S_v) \quad (2)$$

where $values(A)$ is the set of all possible values for attribute A , and S_v is the subset of S for which attribute A has value v (i.e., $S_v = \{s \in S \mid A(s) = v\}$). In other words, $Gain(S, A)$ is the information provided about the target attribute value, given the value of some other attribute A .

Continuous variables, such as temperature, require a somewhat special approach. This is accomplished by dynamically defining new discrete attributes that partition the continuous attributes into a discrete set of intervals. In particular, for an attribute A that is continuous, the algorithm can dynamically create a new Boolean attribute A_c that is true if $A < c$ and false otherwise. The only question is how to best select the value for the threshold c . This is accomplished by selecting values for the threshold based on the existing values of the attribute A and computing the gain. The threshold c that produces the greatest information gain is then chosen (as shown in Equation 3).

$$Result = \max_{c \in A_i} \{Gain(S, A)\} \quad (3)$$

The process of selecting a new attribute and partitioning the training examples is then repeated for each non-terminal descendant node in the tree, only the training examples associated with that node. Attributes that have been incorporated higher in the tree are excluded, so that any given attribute can appear at most once along any path through the tree. This process continues for each new leaf node until either every attribute has already been

included along this path through the tree, or the training examples associated with this leaf node all have the same target attribute value (i.e., their entropy is zero).

The customized decision tree algorithm is defined below, where:

S_i represents the current working subset of the original dataset

A represents one attribute from the set S_i .

The gain is calculated as described in Equation 2.

Algorithm Start

```

1.0      Initialize  $S_i$  to be the full data set
2.0      While  $S_i$  is not empty
2.1      Loop through select  $A$  in  $S_i$ 
2.1.1    If  $A$  is discrete
2.1.1.1  Compute the simple gain (handling missing values)
2.1.2    If  $A$  is continuous
2.1.2.1  Resolve missing values by substituting most common learned values
2.1.2.2  Find the best threshold for  $c$  resolving the maximum gain (eq. 3)
2.1.2.3  Substitute the discrete conversion of  $A$  (using  $c$ ) and calculate gain
2.2      Select the  $A$  with the maximum gain
2.3      Split  $S_i$  using the chosen  $A$ 

```

Algorithm End

This algorithm would halt when S_i has achieved the maximum number of splits. In order to identify the leaves, the algorithm analyzes the structure of the remaining set. If the set contains only one remaining type of data (or only a pre-set proportion of such types) no further splits are required. Leaf nodes are created when the set S_i splits with the same A twice. An example of a resulting decision tree illustrating nodes of attributes between the Alzheimer's patients and normal control is shown in Figure 6-2.

For each grouping, the decision tree algorithm was run on the variables. During tree creation, the variables with the greatest importance, based on external proximity between groups, were used to create the branches. The probability at the resulting nodes indicated whether or not that variable influenced a grouping. The variables that had an influence of greater than 80% were allocated greater priority in cluster creation. By using the results of the decision tree weights and applying them to the cluster analysis, Figure 6-1(b) shows an updated render of the dataset on a 3D space proximity grid. It is apparent that the colours of Figure 6-1(b) are elemental and hence represent a better separation of stages (MCI vs. AD).

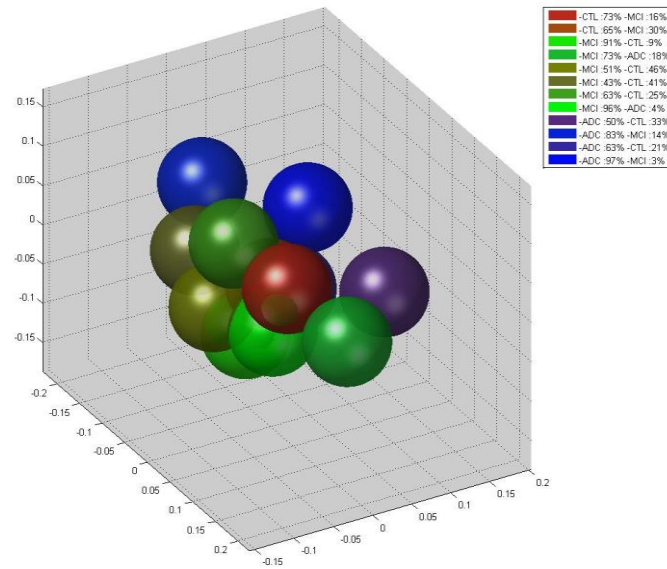
6.4 Discussion and Conclusions

The utilization of clustering and decision trees has potential to provide models which demonstrate the influence and importance of clinical, biomarker imaging, and neuro-

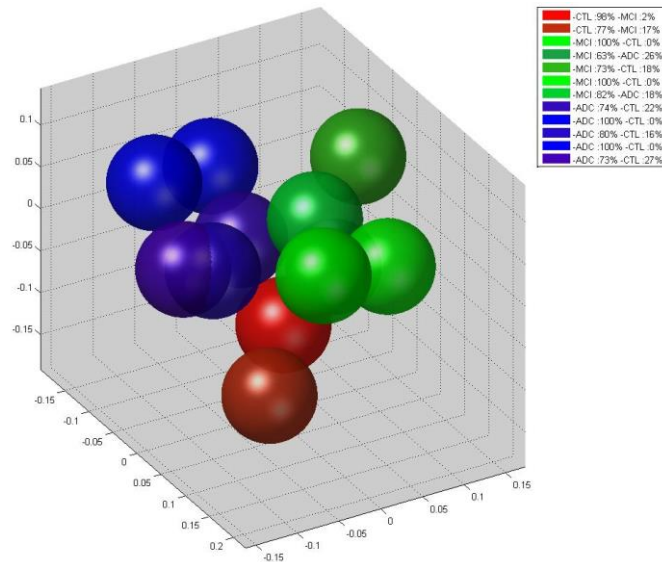
psychological variables on a patient's long term health. This research focused on exploring whether such techniques could be applicable to MRI measures from AD and MCI. Using the proposed techniques, we believe that it will be possible in the future to aid the early detection of AD/MCI patients and allow the application of new drug therapies with the potential to arrest or retard the progression of Alzheimer's disease.

For this study, a modified k-means clustering algorithm was used to partition data into control, MCI and AD sets. Decision tree models were used to identify the level of "importance" of covariates within each cluster. The algorithm provided adequate separation of groups where decision making is possible using this model. Consider the resulting cluster analysis that is rendered in a 3D proximity space (eg. Figure 6-1(a)) where the colours are distinct and their separation gives rise to a grouping). The legend indicates the percentage of patients with a specific outcome within the group. Groups with greater than 80% of the outcome provide insight into variables that tend to collect or accumulate together within that group. Decision trees allow us to expose the strongest variables within each grouping and hence give more weight to these variables during cluster creation.

Future improvements and refinements to the clustering algorithm will include the analysis of each covariate, by calculating the distance of each variable to the centre of the cluster. Ours is one of the first studies to consider clustering in order to help partition variables on the basis of clinical and biological importance. The implications for future drug development and application are supported by our early findings.



(a)



(b)

Figure 6-1 Cluster analysis of AddNeuroMed dataset modeled on 3D space proximity grid. (a) Full variable selection to create a cluster fields. (b) Using only the variables determined to be of value by decision trees. (Implementations of clustering and graphing were applied using C++ and Matlab)

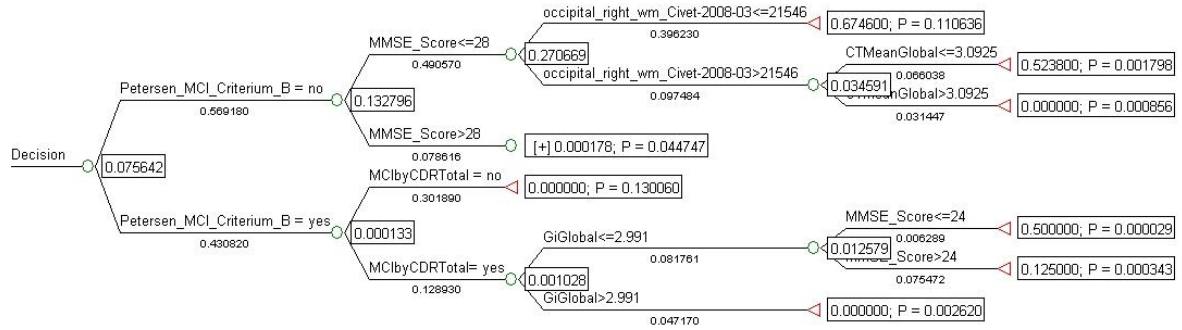


Figure 6-2: Decision tree comparison of normal patients and categorized Alzheimer's patients

Table 6-1: Demographics of AddNeuroMed dataset

Variable	Alzheimer's Disease	Mild Cognitive Impairment	Control
Number	120	122	112
Gender - F/M	77/43	63/59	63/49
Age	75.5 ±6.1	74.4 ±5.7	73.0 ±6.7
MMSE	20.9 ±4.8	26.8 ±3.0	29.0 ±1.2
CDR	1.2 ±0.5	0.5 ±0.1	0
Years of Education	8.1 ± 4.0	8.9 ±4.3	10.7 ±4.8

Data is represented as average ± standard deviation, MMSE = Mini Mental State Examination, CDR = Clinical Dementia Rating (validated measures).

6.5 References

1. Bennett, DA, Wilson, RS, Schneider, JA, Evans, DA, Beckett, LA, Aggarwal, NT, Barnes, LL, Fox, JH and Bach, J. 2002. *Natural history of mild cognitive impairment in older persons*. Neurology. Vol. 59. pp.198–205.
2. Collins, D, Holmes, C, Peters, T and Evans, A. 1995. *Automatic 3D model-based neuroanatomical segmentation*. Human Brain Mapping, Vol. 3:3, pp. 190-208.
3. Fischl B and Dale AM. *Measuring the thickness of the human cerebral cortex from magnetic resonance images*. Proc Natl Acad Sci U S A Vol. 97:11050-11055.
4. Fischl B, Salat DH, Busa E, Albert M, Dieterich M, Haselgrove C, van der Kouwe A, Killiany R, Kennedy D, Klaveness S, Montillo A, Makris N, Rosen B, Dale AM. 2002. *Whole brain segmentation: automated labeling of neuroanatomical structures in the human brain*. Neuron Vol. 33:341-355.
5. Fischl B, Salat DH, van der Kouwe AJ, Makris N, Segonne F, Quinn BT, Dale AM. 2004. *Sequence-independent segmentation of magnetic resonance images*. Neuroimage Vol. 23 Suppl 1:S69-84.

6. Jack CR, Jr., Bernstein MA, Fox NC, Thompson P, Alexander G, Harvey D, Borowski B, Britson PJ, J. W, Ward C, Dale AM, Felmlee JP, Gunter JL, Hill DL, Killiany R, Schuff N, Fox-Bosetti S, Lin C, Studholme C, DeCarli CS, Krueger G, Ward HA, Metzger GJ, Scott KT, Mallozzi R, Blezek D, Levy J, Debbins JP, Fleisher AS, Albert M, Green R, Bartzokis G, Glover G, Mugler J, Weiner MW. 2008. *The Alzheimer's Disease Neuroimaging Initiative (ADNI): MRI methods*. J Magn Reson Imaging; Vol. 27:685-691.
7. Johnson, KA, Jones, K, Holman, BL, Becker, JA, Spiers, PA, Satlin, A, Albert and MS. 1998. *Preclinical prediction of Alzheimer's disease using SPECT*. Neurology. Vol. 50. pp. 1563–1571.
8. Kim, JS, Singh, V, Lee, JK, Lerch, J, Ad-Dab'bagh, Y, MacDonald, D, Lee, JM, Kim, SI, Evans, A. 2005. *Automated 3-D extraction and evaluation of the inner and outer cortical surfaces using a Laplacian map and partial volume effect classification*. NeuroImage, Vol. 27:1, pp. 210-221.
9. Krasuski, JS, Alexander, GE, Horwitz, B, Daly, EM, Murphy, DG, Rapoport, SI and Schapiro, MB. 1998. *Volumes of medial temporal lobe structures in patients with Alzheimer's disease and mild cognitive impairment (and in healthy controls)*. Biol Psychiatry. Vol. 43. pp. 60–68.
10. McKelvey, R, Bergman, H, Stern, J, Rush, C, Zahirney, G and Chertkow, H. 1999. *Lack of prognostic significance of SPECT abnormalities in non-demented elderly subjects with memory loss*. Can J Neurol Sci. Vol. pp. 26:23–28.
11. Morris, JC, Storandt, M, Miller, JP, McKeel, DW, Price, JL, Rubin, EH and Berg, L. 2001. *Mild cognitive impairment represents early-stage Alzheimer disease*. Arch Neurol. Vol. 58. pp. 397–405.
12. Petersen, RC, Smith, GE, Waring, SC, Ivnik, RJ, Tangalos, EG and Kokmen, E. 1999. *Mild cognitive impairment: clinical characterization and outcome*. Arch Neurol. Vol 56. pp. 303–308; correction: 56:760.
13. Quinlan, JR. 1986. *Induction of decision trees*. Machine Learning. Vol. 1, pp. 81-106.
14. Redding NJ. 2000, *Implicit Polynomials, Orthogonal Distance Regression, and the Closest Point on a Curve*. IEEE Trans. On Pat Anal and Mach. Intel. Vol. 22:2 pp.191-199.
15. Ritchie, K and Touchon, J. 2000. *Mild cognitive impairment: conceptual basis and current nosological status*. Lancet. Vol. 355. pp. 225–228.
16. Simmons A, Westman E, Muehlboeck S, Mecocci P, Vellas B, Tsolaki M, Kloszewska I, Wahlund LO, Soininen H, Lovestone S, Evans A, Spenger C. 2009. *MRI measures of Alzheimer's disease and the AddNeuroMed study*. Ann N Y Acad Sci Vol. 1180:47-55.
17. Simmons A, Westman E, Muehlboeck S, Mecocci P, Vellas B, Tsolaki M, Kloszewska I, Wahlund LO, Soininen H, Lovestone S, Evans A, Spenger C. 2010. *The AddNeuroMed framework for multi-centre MRI assessment of longitudinal changes in Alzheimer's disease: experience from the first 24 months*. Int J Ger Psych. In press.
18. Sled, JG, Zijdenbos, AP and Evans, AC. 1998. *Nonparametric method for automatic correction of intensity nonuniformity in MRI data*. IEEE Trans. Med. Imag. Vol. 17. pp. 87–97.

Chapter 7 – Article 5

7 A Markov Analysis of Patients Developing Sepsis using Clusters*

Abstract: Sepsis is a significant cause of mortality and morbidity. There are now aggressive goal oriented treatments that can be used to help patients suffering from sepsis. By predicting which patients are more likely to develop sepsis, early treatment can potentially reduce their risks. However, diagnosing sepsis is difficult since there is no “standard” presentation, despite many published definitions of this condition.

In this work, data from a large observational cohort of patients – with variables collected at varying time periods – are observed in order to determine whether sepsis develops or not. A cluster analysis approach is used to form groups of correlated data points. This sequence of data points is then categorized on a per person basis and the frequency of transitioning from one grouping to another is computed. The result is posed as a Markov model which can accurately estimate the likelihood of a patient developing sepsis. A discussion of the implications and uses of this model is presented.

Keywords: Sepsis, Markov Chains, Cluster Analysis, Predictive Modelling.

7.1 Introduction

Sepsis is defined as an infection with systematic manifestations of an infection [7]. Severe sepsis is considered present when sepsis co-exists with sepsis-induced organ dysfunction or tissue hypoperfusion [7]. This can result in mortality and morbidity, especially when associated with shock and/or organ dysfunction [3]. Sepsis can be associated with increased

* A version of this chapter has been published: Femida Gwadry-Sridhar, Michael Bauer, Benoit Lewden, Ali Hamou. “A Markov Analysis of Patients Developing Sepsis Using Clusters”, Knowledge Representation for Health-Care. KR4HC 2010. Lecture Notes in Computer Science, Springer. 2011, vol. 6512.

hospital resource utilization, prolonged stays in intensive care units (ICU) and hospital wards, decreased long-term health related quality of life and an economic burden estimated at \$17 billion USD (equivalent to \$17.49 billion CAD) each year in the United States alone [5, 17, 21]. In Canada, there is limited data on the burden of severe sepsis; however, costs in Quebec may be as high as \$73 million CAD per year [13] which contributes to the estimate of total Canadian cost of approximately \$325 million CAD per year.

Patients with severe sepsis generally receive their care in an ICU. A multinational study of sepsis in teaching hospitals found that severe sepsis or septic shock is present or develops in 15% of ICU patients [1]. However, diagnosing sepsis is difficult since there is no “standard” presentation despite many published definitions for sepsis [2, 14]. In the STAR registry [15] (containing a mix of teaching and community hospitals across Canada), the total rate for severe sepsis was 19%. Of these, 63% occurred after hospitalization.

The management of severe sepsis requires prompt treatment within the first six weeks of resuscitation [7]. Intensivists currently support the use of early goal-directed resuscitation of patients. This has shown to improve survival in patients presenting to emergency rooms with septic shock [7].

Given the many advances in medicine today, there now exist aggressive goal oriented treatments that can be used to help patients with sepsis and severe sepsis [4, 16, 18]. If researchers could predict which patients may be at risk for sepsis, treatment may be started early and potentially reduce the risk of mortality and morbidity. Therefore, methods that help with the early diagnosis of patients who either have or are at risk for sepsis within hospitals are in dire need and in fact may result in better prognosis if interventions are initiated early.

7.1.1 Analytic Techniques

A variety of analytical techniques can be used to establish relationships and assess the strength of these relationships among a set of measured variables or quantities. Researchers commonly use univariate or multivariable regression models to estimate the association between prognostic variables and a clinical outcome (such as sepsis). Multivariable regression models are frequently used in studies where clinical outcomes are included. These

models can use both categorical and continuous variables, but the use of uncritical modeling techniques can lead to erroneous conclusions and resultant imprecision [9].

In this work, our primary goal is to determine patients at risk of a particular clinical diagnosis – sepsis being the reference case. Many approaches exist for analyzing patients with and without sepsis [8]. These approaches generally use regression models, which assume the existence of an identifiable, singular set of variables (or variables) for prediction. Hence, if there exist multiple sets of variables that appear in several independent traits, then prediction with this method becomes difficult. The current literature illustrates some of the limitations with univariable and multivariable models [8, 18, 19]. In order to address such limitations, alternative approaches to simplify the multi-faceted nature of predicting sepsis need to be investigated.

In this paper, we construct a Markov model to predict sepsis using patient data from 12 Canadian Intensive Care Units (ICU’s). Our model differs fundamentally from those previously used for predicting an outcome. Outcome probabilities are generated by the use of a k-means cluster analysis algorithm to group variables into correlated datapoints and then use these to define the “states” in a Markov model. Transitions in the model are determined based on successive values of the datapoints for individual patients. The transition model assumes that patient’s risk changes dependent on their state of health.

Section 2 describes the approach in detail and depicts examples and implications of the proposed model. Section 3 describes the results and Section 4 explores the model’s repercussions and future initiatives. Section 5 concludes and summarizes this work.

7.2 Methods

7.2.1 Data Acquisition

We obtained data that was collected from 12 Canadian ICU’s that were geographically distributed and included a mix of medical and surgical patients [15]. The study was approved by the University of Western Ontario Research Ethics Board and the need for informed consent was waived. Data was collected on all patients admitted to the ICU who had a stay greater than 24 hours or who had severe sepsis at the time of admission. Patients who did not receive active treatment were excluded. We screened over 23,000 patients for sepsis (of

which 4,196 were randomly selected for this study). Patients with confirmed sepsis were classified as “septic.” It is normal practice in the ICU to treat patients with suspected sepsis as septic until blood cultures are available.

Hospitals routinely collect a minimum data profile on all eligible patients admitted to the ICU [6]. This includes demographic information, admission data, source of admission, diagnosis, illness severity, outcome and length of ICU and hospital duration. Table 1 presents a summary of the variables collected in this data profile for this study. This table also shows the influence of each variable on sepsis output when analyzed with a simple logistic regression model (since the variables were Boolean – or binary in terms of the analysis). We have previously reported this analysis. [8]. Illness severity scores were calculated using a validated formula from data obtained during the first 24 hours in the ICU [11, 12]. All patients were subsequently assessed on a daily basis for the presence of infection and severe sepsis. Hence, for patients with stays longer than 24 hours, a repeated measures of the variables in Table 1 were collected and averaged on their daily condition. The characteristics of the variables are a part of standard ICU testing protocol and have been described elsewhere [15].

7.2.2 Model Formulation

Our patient data is modeled in the following format:

$$\begin{aligned} p_1 &: d_{11}, d_{12}, \dots, d_{1n_1} \\ p_2 &: d_{21}, d_{22}, \dots, \dots, \dots, d_{2n_2} \\ p_3 &: d_{31}, d_{32}, \dots, \dots, d_{3n_3} \\ &\dots \end{aligned}$$

where p_i represents a patient in our data set, and d_{ij} represents a datapoint, each consisting of measurements for the 25 variables identified in Table 1 (where i represents the patient and j represents the data collection variable). A non-predetermined number of datapoints hence exists for each patient. These datapoints progressed time-wise from initial admittance to the ICU/ward until departure or death. The time period between datapoints typically fell on consecutive days, though this was not always the case (dependent on hospital protocols and staff availability).

Table 7-1: Sepsis Study: 25 variables collected to form a single datapoint

Variables	P value	Exp(B)
Anaerobia culture	0.122	0.317
Abdominal diagnosis	0.000	15.027
Blood diagnosis	0.000	3.574
Lung diagnosis	0.000	10.360
Other diagnosis	0.000	8.492
Urine diagnosis	0.000	7.280
Chest X-ray and purulent sputum	0.000	2.756
Gram negative infection culture	0.047	0.679
Gram positive infection culture	0.001	0.533
Heart rate > 90bpm	0.000	16.933
No culture growth	0.000	0.103
PaO ₂ /FiO ₂ < 250	0.000	12.305
pH < 7.30 or lactate > 1.5 upper normal with base deficit > 5	0.141	1.242
Platelets < 80 or 50% decrease in past 3 days	0.000	5.665
Respiratory rate > 19, PaCO ₂ < 32 or Mechanical ventilation	0.000	8.866
SBP < 90 or MAP < 70 or Pressure for one hour	0.000	9.963
Abdominal culture	0.259	1.872
Blood culture	0.000	2.311
Lung culture	0.724	0.932
Other site culture	0.614	0.869
Urine culture	0.100	1.450
Temperature < 36 or > 38	0.000	8.246
Urinary output < 0.5 mL/kg/hr	0.000	3.166
WBC > 12 or < 4 or > 10% bands	0.000	6.281
Yeast culture	0.011	0.492
Constant	0.000	0.000

Analysis of the collected data was especially challenging for several reasons:

- *The number of datapoints per patient varied. For instance, some patients had two or three datapoints, while for others there was a dozen or more.*
- *The time periods between datapoints for a patient occasionally varied.*
- *The conditions of patients when admitted were extremely diverse; some were severely ill, already showing signs of sepsis, while others showed none. Hence, the first datapoint of two separate patients would not correspond to the same stage of illness.*

Clustering. Since the datapoints across the patient dataset is not aligned, as stated above, we had to address this by considering all datapoints independently for an initial cluster analysis.

In our previous work [8], cluster analysis had been used to group patients with and without sepsis based on their initial datapoint. This proved to be a useful approach for grouping patients. In this instance, the clustering would group similar datapoints as well – one could consider the datapoints within the same cluster as representing the same “state” of a patient. That is, similar datapoints would be clustered regardless of their position within a timeframe for an individual patient. Though not considered in this initial clustering algorithm, timeframe measurement data will be considered when such datapoints are placed within the Markov model.

A variety of different clustering sizes and algorithms were explored. Data clustering algorithms can be hierarchical. Hierarchical algorithms find successive clusters using previously established clusters. Hierarchical algorithms can be agglomerative (“bottom-up”) or divisive (“top-down”). Agglomerative algorithms begin with each variable as a separate cluster and merge them into successively larger clusters. Divisive algorithms begin with the whole set and proceed to divide it into successively smaller clusters.

A modified k-means clustering algorithm (which was modeled to be agglomerative) was used in this work due to its speed of execution on large datasets (over hierarchical for instance). This algorithm incorporates both the internal consistency of variables within the cluster (distance to the cluster’s centroid) and the external distance to all neighboring clusters as its heuristic. The k-means algorithm used is refinement-iterative and alternates between assignment (where each variable is assigned to a cluster) and updating (calculation of new means of the cluster centre). By doing so, clusters will eventually incorporate all variables within the closest proximity space. In general, the correct choice of k (being the number of clusters) is often ambiguous, with interpretations depending on the shape and scale of the distribution of points in a data set and the desired clustering resolution of the user. However, for this study the number of clusters was chosen to be 12 – resulting in clusters that were neither too large to manage (over fitted), nor ones with too few datapoints to give an adequate determination of patient status due to lack of separation. k was achieved by examining the percentage of variance of a function of the number clusters. Hence, adding greater than 12 clusters didn’t achieve better modeling of the results given the modifications to the clustering algorithm (i.e. custom distance measures).

During cluster generation, the algorithm is applied to every variable within the dataset. Variables are then ranked by influence and probability of defining a cluster and its location within the cluster field (internal consistency measure). The mathematical indicator used to create these groupings is defined as the orthogonal distance between clusters. Each variable was essential a discrete point in a space which has its own dimension and base (the dimension of each variable is simply the number of categories available). For example, if a variable can take two distinct values then our base for this space becomes $(1,0)(0,1)$. These two vectors are orthogonal to each other and therefore are a base for this particular space.

Since our datapoints were binary categorized, each binary variable was normalized along its matrix length and squared. Furthermore, in the event of datapoints that were equidistant to multiple centroids, the internal consistency of each cluster was measured and the tighter field was chosen. This prevented the ballooning of the cluster sets. Based on this consistency measure, each cluster is labelled either sepsis or non-sepsis depending on the different distributions of the datapoints within.

The algorithm behaves very close to the standard k-means algorithm:

- **Initialization:**
 - Select first datapoint as the first centroid.
 - Calculate distance between centroid and all other points, select the furthest point as second centroid (based on the distance calculated above).
 - Choose the furthest point from the first two centroids as the third.
 - Continue until N centroids (clusters) are achieved.
- **Iterate:**
 - Each datapoint is sent to its closest cluster.
 - Recalculate cluster centres. (The centre minimizes the distance from itself and each point. Hence, the distance between the centre and each point is minimized by assigning it the most common category among its cluster).
 - Repeat until no change

The proposed algorithm also varies by compensating for “attraction points” such that clusters smaller than 0.05% of the total size were removed at the end of each iteration and a new centroid was determined based on calculating the point furthest away from the other centroids. Furthermore, datapoints containing missing values were not considered suitable candidates for any centroid positions.

Markov Model. Following the cluster computation, each individual patient within the dataset was analyzed. The individual datapoints, for instance, $d_{11}, d_{12}, \dots, d_{1nl}$, were considered separately. If d_{11} was in cluster C_i and d_{12} was in cluster C_j , then a transition from C_i to C_j was created. The frequency of each transition was also tracked and so the total number of transitions from C_i to any cluster, including C_i could be determined. This resulted in each cluster being considered its own “state” and revealing the probability of a transition from one cluster to another. Hence neighbouring datapoints will be represented by the transitions between states.

All transition points were created by comparing each datapoint to every other datapoint occurring in the future. This provides a temporal compliance (or normalization), such that the time between $d_1 - d_3$ for a patient might be the same as the time between $d_1 - d_2$ for another patient (or that the evolution of the infection during this “period” could be the same, in other words the duration of $d_1 - d_3$ may equate $d_1 - d_2$.)

In order to complete the model, the following metrics were also recorded for each datapoint within a cluster: (a) whether the patient did or did not have sepsis; (b) whether this was the last datapoint associated with the patient or not and if it was the last datapoint what the outcome was – namely discharged or deceased.

7.3 Results

A Markov graph with 14 states – 12 states corresponding to the clusters and 2 additional states – one for patients that had been discharged (Alive as represented in Figure 7-1) and one for those that were deceased was generated. The partial model for one Markov transition graph is represented by the in Figure 7-1. (The remaining 11 transition graphs were left out for efficiency and clarity – however they can be seen in the originally published work). Transitions are represented by arrows to the new states (which are demarked as “Clusters”).

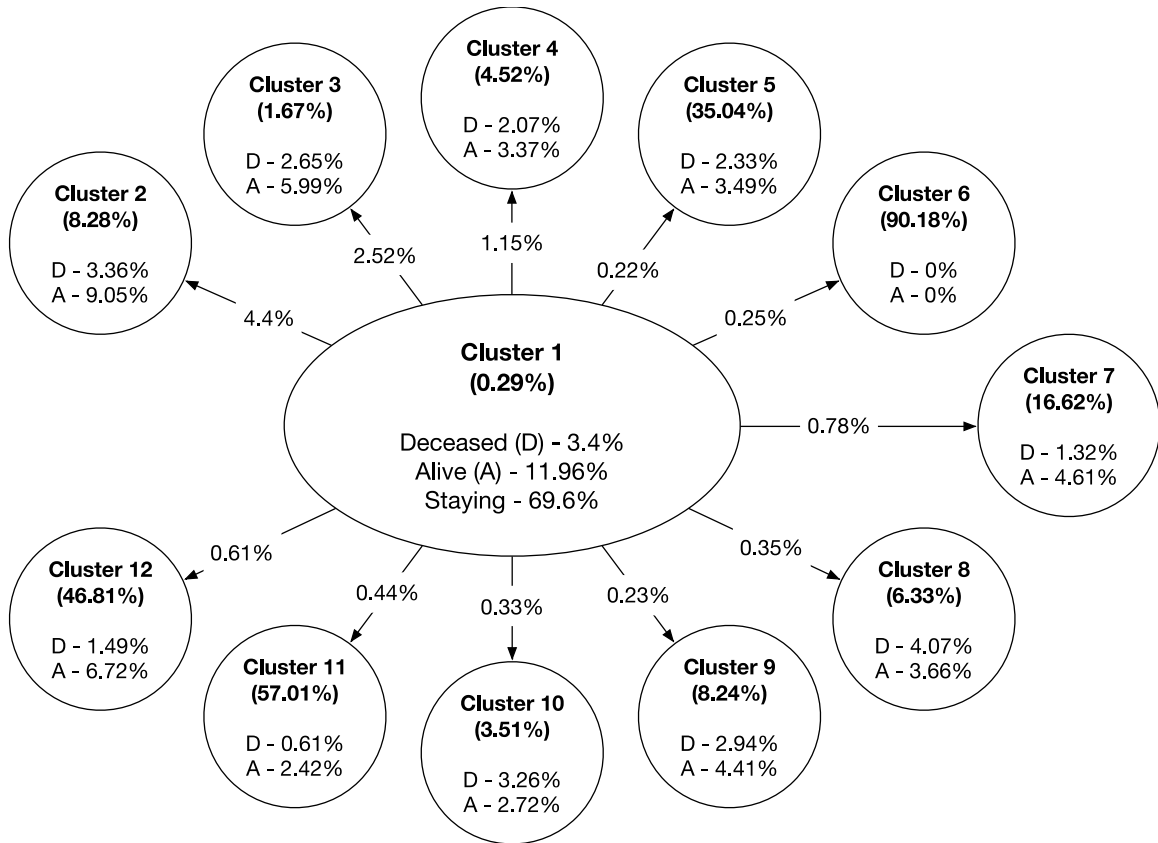


Figure 7-1: Markov transition graph represented by first cluster

However, in order to simplify an explanation of the results, Figure 7-2 illustrates a portion of the graph for 3 states: states #1, #5, and #6. The two final gray nodes represent the “deceased” state and the “discharged” state. What is not shown in the graph is the percent of patients that had been diagnosed with sepsis at the time their datapoints were included. These are 0.3%, 35.0% and 90.18% for nodes #1, #5 and #6, respectively.

Note that a significant portion (57.8%) of the datapoints that were assigned to state #1, were followed by their adjacent datapoint which was also assigned to state #1. Given the very low percentage of patients diagnosed with sepsis within this cluster, this is likely a state indicative of patients being admitted, never developing sepsis symptoms, remaining for several days, and finally being discharged.

Node #5 can be considered representative of a patient developing sepsis (hidden or apparent, depending on variable characteristics), or a patient recovering from it, as most patients have a 35% chance of sepsis in this state. It is not relevant which, as the model will provide a predictor to which its next state will be.

Node #6 represents a state which can be thought of as one characterizing a patient with sepsis, since 90.18% of the patients having datapoints in this cluster were diagnosed with sepsis. Interestingly, 25.9% return to state #1, where relatively few patients were identified with sepsis. It is also interesting to note that from state #6 no patients died or were discharged. This is likely due to aggressive treatment of sepsis when symptoms become severe and apparent.

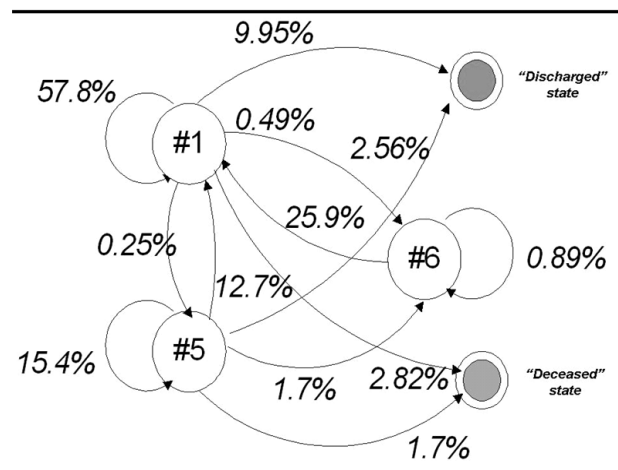


Figure 7-2: Portion of Markov Graph

7.3.1 Further Implications

There are many clinical applications where this model can be used. Consider the following scenario where there exists a datapoint (the 25 variable set) for a patient admitted to an ICU. This datapoint can be matched to a cluster, i.e., a “state”. From this state in the model, the probability of the patient transitioning to a new state can be determined at the next “time point”. For each “next state”, there exists a probability that the patient will develop sepsis. Order is not implied in the model and is left to the transition probabilities, giving rise to a powerful predictor. Finally, the likelihood of the patient developing sepsis by summing over all possible transitions can easily be computed.

For example, assume that Figure 7-1 represents the entire Markov graph. If a patient’s datapoint ends up in state #1, the patient’s estimated probability of developing sepsis is calculated as follows:

$$\begin{aligned}
 \text{Probability of Sepsis} &= 0.578*0.0129 + 0.0025*0.3504 + 0.0049*0.9018 \\
 &= 0.012648, \text{ or } 1.26\%
 \end{aligned}$$

This is only a one-step approximation – since it only considers a transition from state #1 to its adjacent states by multiplying the transition probabilities by the state sepsis ones. In this example, the one-step approximation illustrates the probability of the patient developing sepsis using paths of length one. In general, one could compute paths of any length (limited by the longest stay of any patient in the hospital in the dataset). Similarly, the probability of a patient not developing sepsis, becoming discharged or becoming deceased, can also be computed using the same algebraic technique.

7.3.2 Validation

In this study, 4,196 patients were selected in order to test the accuracy of the proposed method. In total, 23,547 datapoints were available from the patient dataset. Testing the precision of the clustering was achieved by first randomly selecting 10% of the datapoints and removing them from the dataset for testing. Cluster generation followed by training on this sub-sampled dataset, and testing on the removed datapoints, by matching them to the trained clusters. These datapoints were then analysed to see whether they were repatriated to a cluster that represented their end state (sepsis versus non-sepsis) – as if they were part of the original training set.

For sepsis patients, an 80.01% precision rate was achieved (when recursive training and testing was applied to the datapoints during cross-validation – in this instance, 1000 datapoints were swapped for each train/test run). For non-sepsis patients, a 94.69% precision rate was achieved, partly because non-sepsis patients represented a larger sample size throughout.

7.3.3 Future Work

The proposed technique will be thoroughly tested against other ICU patient cohorts in Europe. Clusters will be used in conjunction with decision trees models in order to identify which variables truly influence the development of sepsis versus non-sepsis in patients. Furthermore, the non-homogeneous feature-based classification ability of decision trees and the temporal break sequence modeling based on the Markov process should improve results

significantly. *Kim and Oh's* [10] proposed algorithm will be modified and utilized in future works to further improve the model.

7.4 Conclusions

Multiple methods of analyzing clinical data provide different perspectives on assessing patient health. We have demonstrated the use of cluster analysis as an efficient and relatively swift method for identifying patients at risk – or not at risk – of a clinical condition, being sepsis. The reliability and the validity of these clusters increases based on sample size and based on testing across different datasets. Cluster analysis can be used as an effective tool to supplement the daily monitoring of patients. By utilizing the transitioning probabilities through a Markov model, clinicians can have a greater awareness regarding a patient who is no longer at risk of contracting sepsis. This gives the clinician the ability to make a more informed decision on treatment. Utilizing multi-faceted mathematical modeling is a useful clinical informatics approach to support clinical decision making, the utilization of evidence based treatment and efficiencies in health resource utilization.

7.5 References

1. Alberti C, Brun-Buisson C, Burchardi H, Martin C, Goodman S, Artigas A, et al. Epidemiology of sepsis and infection in ICU patients from an international multicentre cohort study. *Intensive Care Med.* 2002;28(2):108-21.
2. American College of Chest Physicians/Society of Critical Care Medicine Consensus Conference: definitions for sepsis and organ failure and guidelines for the use of innovative therapies in sepsis. *Crit Care Med* 1992;20(6):864-74.
3. Angus DC, Linde-Zwirble WT, Lidicker J, Clermont G, Carcillo J, Pinsky MR. Epidemiology of severe sepsis in the United States: analysis of incidence, outcome, and associated costs of care. *Crit Care Med.* 2001;29(7):1303-10.
4. Bernard GR, Vincent JL, Laterre PF, LaRosa SP, Dhainaut JF, Lopez-Rodriguez A, et al. Efficacy and safety of recombinant human activated protein C for severe sepsis. *N Engl J Med.* 2001;344(10):699-709.
5. Brun-Buisson C, Doyon F, Carlet J, Dellamonica P, Gouin F, Lepoutre A, et al. Incidence, risk factors, and outcome of severe sepsis and septic shock in adults. a multicenter prospective study in intensive care units. French ICU Group for Severe Sepsis. *JAMA.* 1995;274(12):968-74.
6. Chen LM, Martin CM, Morrison TL, Sibbald WJ. Interobserver variability in data collection of the APACHE II score in teaching and community hospitals. *Crit Care Med.* 1999;27(9):1999-2004.

7. Dellinger RP, Levy MM, Carlet JM, Bion J, Parker MM, Jaeschke R, et al. Surviving sepsis campaign: international guidelines for management of severe sepsis and septic shock: 2008. *Crit Care Med.* 2008;36(1):296-327.
8. Gwadry-Sridhar F, Lewden B, Mequanint S, Bauer M. Comparison of analytic approaches for determining variables: a case study in predicting the likelihood of sepsis. In *HEALTHINF 2009. Proceedings of INSTICC*; Jan 14-17 January 2009; Porto, Portugal; 2009;90-6.
9. Harrell FE, Jr., Lee KL, Mark DB. Multivariable prognostic models: issues in developing models, evaluating assumptions and adequacy, and measuring and reducing errors. *Stat Med* 1996;15(4):361-87.
10. Kim SH, Oh SS. Decision-tree-based Markov model for phrase break prediction. *ETRI Journal.* 2007;29(4):527-9.
11. Knaus WA, Draper EA, Wagner DP, Zimmerman JE. APACHE II: a severity of disease classification system. *Crit Care Med.* 1985;13(10):818-29.
12. Knaus WA, Wagner DP, Draper EA, Zimmerman JE, Bergner M, Bastos PG, et al. The APACHE III prognostic system. risk prediction of hospital mortality for critically ill hospitalized adults. *Chest* 1991;100(6):1619-36.
13. Letarte J, Longo CJ, Pelletier J, Nabonne B, Fisher HN. patient characteristics and costs of severe sepsis and septic shock in Quebec. *J Crit Care* . 2002;17(1):39-49.
14. Levy MM, Fink MP, Marshall JC, Abraham E, Angus D, Cook D, et al. 2001 SCCM/ESICM/ACCP/ATS/SIS International Sepsis Definitions Conference. *Crit Care Med.* 2003;31(4):1250-6.
15. Martin CM, Priestap F, Fisher H, Fowler RA, Heyland DK, Keenan SP, et al. A prospective, observational registry of patients with severe sepsis: The Canadian Sepsis Treatment and Response Registry. *Crit Care Med.* 2009;37(1):81-8.
16. Minneci PC, Deans KJ, Banks SM, Eichacker PQ, Natanson C. Meta-analysis: the effect of steroids on survival and shock during sepsis depends on the dose. *Ann Intern Med.* 2004;141(1):47-56.
17. Pittet D, Rangel-Frausto S, Li N, Tarara D, Costigan M, Rempe L, et al. Systemic inflammatory response syndrome, sepsis, severe sepsis and septic shock: incidence, morbidities and outcomes in surgical ICU patients. *Intensive Care Med* 1995;21(4):302-9.
18. Riaño, D. and Prado, S. A Data Mining Alternative to Model Hospital Operations: Filtering, Adaption and Behaviour Prediction. *Medical Data Analysis LNCS.* 2000: 1933(1):132-154.
19. Riaño, D. and Prado, S. The Analysis of Hospital Episodes. *Medical Data Analysis. LNCS.* 2001: 2199(1):231-237.
20. Rivers E, Nguyen B, Havstad S, Ressler J, Muzzin A, Knoblich B, et al. Early goal-directed therapy in the treatment of severe sepsis and septic shock. *N Engl J Med.* 2001;345(19):1368-77.

21. Salvo I, de CW, Musicco M, Langer M, Piadena R, Wolfler A, et al. The Italian SEPSIS Study: preliminary results on the incidence and evolution of SIRS, sepsis, severe sepsis and septic shock. *Intensive Care Med.* 1995;21(Suppl 2):244-249.

Chapter 8 – Article 6

8 A Disease Registry and Disease Management System for Patients with Malignant Melanoma*

Abstract: Strategies and interventions designed to better understand melanoma can help reduce the risk and rate of the disease. Current registries and information systems are generic in nature and not tailored to a specialist's workflow or clinic needs. Efficient data collection systems and application of effective workflow models can lead to significant improvements in quality of healthcare. We have developed a unique longitudinal tracking system for the treatment and outcome management for patients with melanoma. The system's design was informed by healthcare providers, a review of existing systems and published literature. Several modules have been established to address the concerns of the healthcare clinic, including: patient demographics, imaging, patient surveys, security, reporting and analysis. This framework is capable of displaying disease imaging screens, visually and interactively tracking melanoma sites, automatically computing staging scores, and tracking all surgeries and outcomes. Conditional patient access provides an interactive model of care to the clinic.

Keywords: Information storage and retrieval; Electronic health record; Information systems

8.1 Introduction

The past decade has seen a dramatic increase in the incidence of malignant melanoma, with an estimated 1.97% of people being diagnosed within their lifetime [1-5]. As the leading cause of death from skin disease, malignant melanoma accounts for approximately 1.2% of all cancer death with an estimated 8,790 disease-related deaths in 2011 [4,6,7].

* A version of this chapter has been published: Ali Hamou, Stacey Guy, Alexandria Ratzki-Leewing, Jesse O'Brien, Femida Gwadry-Sridhar, "A Disease Registry and Disease Management System for Patients with Malignant Melanoma", AHIC – Advances in Health Informatics Conference, 2012.

Despite efforts to allay the impact and incidence of melanoma, disease-related mortality has remained relatively unimproved over the past decade. The current 5 year survival rate for people with advanced disease, or who have relapsed after initial treatment is less than 5% [2]. Strategies and interventions designed to better understand melanoma can help reduce the risk and rate of the disease.

The growing complexity of medical care has triggered the use of computers for acquisition, storage, and retrieval of medical information. Efficient data collection systems and application of effective workflow models can lead to significant improvements in the quality of healthcare, namely an increase in patient safety and a reduction in healthcare costs [8-12].

Most electronic patient record platforms are generic in nature (i.e. are not based on specialist workflow) creating cumbersome controls for specific clinic needs. By developing a platform with these characteristics in mind, we have created a platform that inherently improves the patient clinical experience and facilitates direct patient engagement through the use of portals.

Utilizing these building blocks we designed an electronic, longitudinal tracking system for the treatment and outcomes management for patients with melanoma. We felt that the data collection and analysis facilitated by this system could provide critical data markers that help improve the care of clinical processes.

This paper describes the development and design of an electronic clinical management system for a melanoma clinic in Ontario, Canada.

8.2 Methods

8.2.1 System Design

We have developed a longitudinal data tracking framework which utilizes a MySQL backend database management system (DBMS) and PHP with an AJAX front end web platform. We established several modules to address the concerns of healthcare institutions including: patient demographics, imaging, patient surveys of patient important outcomes, security and secure authentication, reporting, and analysis. To establish relevant data parameters, we worked with an oncologist with expertise in this area; conducted a review of the literature

and reviewed other melanoma data collection systems, globally. Data was collected on patients, registration, diagnosis, pathology (with imaging), staging, treatment, surgeries, sentinel node biopsies, node dissection, radiotherapy, systemic therapy, outcome and/or follow-up, and current patient status.

By creating a high quality interactive customized workflow based on intuitive data collection screens and a clinical tracking tool, we have helped standardize the data representation similar to a standard melanoma clinical workflow. This approach helps minimize tool adoption rate times and reduces the need for paper-based tracking systems, reducing data entry errors and increasing clinical efficiency. Our system is capable of displaying disease imaging screens, visually and interactively tracking melanoma sites, automatically computing staging scores, and tracking all surgeries and outcomes. Conditional patient access provides an interactive model of care to the clinic.

8.2.2 Collecting Patient Information

In a traditional system, baseline information is typically manually collected by a healthcare provider. These forms are transcribed or coded into an electronic database of patient records. Direct data entry leads to various quality control issues. To address this challenge, our lab designed the platform to be used not only with kiosk systems, but with web capable tablet systems as well.

We have established various techniques to improve quality control and to ensure accuracy of patient records. First, demographic data can be directly imported into the database onsite by the patient or nurse. Second, field validation is used to ensure that no data is missing or incorrectly filled (i.e., values out of permissible range). Administrators are able to designate these fields and form validation on each entry. Third, data collection forms are clinical workflow oriented, with built-in data validation (data flagging), auto-complete, and dropdowns to facilitate fewer entry mistakes as shown in Figure 8-1. The resulting increase in quality control ensures accurate patient record entry—the more accurate the demographics, the more accurate the statistical analysis.

Figure 8-1 shows clinical workflow oriented data collection forms with auto-complete and dropdowns for fewer entry mistakes as well built-in data validation (data flagging).

The image shows two data collection forms. The top form is titled "Radiotherapy" and contains a "Treatments" list with dates 2010-08-04 and 2010-08-21. To the right are fields for Indication (Adjuvant), Date of First Dose (2010-08-04), Oncologist (Engel), Site (Skin), Dose (cGy, # of fractions), and Energy (Electrons, Photons, Other). A "Save Treatment" button is at the bottom. The bottom form is titled "Systemic Therapy" and contains an "Adjuvant Therapy (Static Form)" section with fields for Date of first dose (2011-11-08), Indication (T4), Adjuvant Regimen (Temosolomide), and a list of complications (Headaches, Nausea/vomiting, Renal insufficiency, Lymphopenia, Ototoxicity, Psychiatric dysfunction, Asthenia, Abnormal liver function, Neutropenia, Thrombocytopenia, Neurotoxicity, other). A "Completed Prescribed Regimen" dropdown is set to "yes". A "Save Adjuvant Therapy" button is at the bottom. Below this is a "Metastatic Treatment" section with a "Treatments" list showing 2014-02-11, Date of First Dose (2014-02-11), Symptoms (Yes), and Sites of Metastatic Disease (Brain).

Figure 8-1: Data collection forms

A patient portal module was also created to collect and easily store feedback and data on patient quality of life. Based on the results of the quality of life survey (filled out by each patient), educational information is displayed back to the patient regarding disease-specific issues such as the effects of their medications. This module can also be used to collect and monitor patient knowledge, medication compliance, satisfaction with the platform, and health-related quality of life. Additionally, patients can use this module to visually indicate the location of any pain which can be viewed by a clinician to determine cause and treatment.

These surveys can be completed in a patient waiting room using either a web-enabled tablet or kiosk—these devices can be reserved for waiting rooms and used to simultaneously collect patient feedback, educate patients on their illness, and even indicate to patients when the clinician is ready to see them. Patients can also provide an email address or mobile phone number so they can continue to receive educational material after their visit.

8.2.3 Imaging

An imaging platform with all associated patient diagnostic images is located within each patient record (Figure 8-2). By including images in the electronic patient record our platform provides an additional layer of comprehensiveness. Clinicians can access the platform and analyze the images with all associated test results to verify findings; images are downloadable to a clinician's personal device if further analysis is required. Users can also highlight and focus on selected areas of the image via simple imaging tools such as magnify and reorient. The interactive visual displays of our platform offer screen demarcation of melanoma site, variable sizing and coloring option, and information regarding initial diagnosis. A collapsible on-screen imaging module accompanied with information and measurements is available for pathology and the general patient.

Figure 8-2 shows a collapsible on-screen imaging module accompanied with the measurements related to the images being shown.

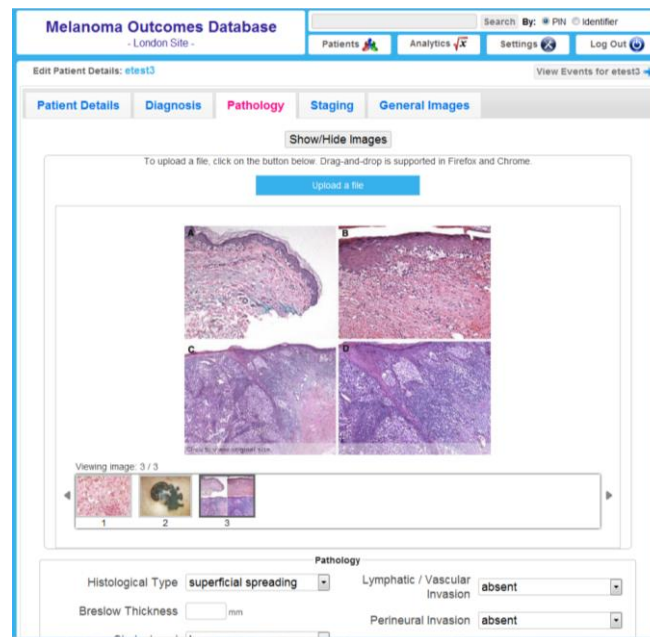


Figure 8-2: Imaging for pathology and general patient

8.2.4 Access and Security

The platform utilizes sftp and https (SSL-enabled authentication) encrypted pages to prevent intrusion from external malicious attacks. A social access control mechanism was also

established within the system to prevent internal attacks; this was partially accomplished by assigning each user with a level of access within their domain. A hospital grade firewall housed and secured the internal database and all data was backed-up nightly in case of failure or corruption; system retractibility is also ensured by tracking and logging all database actions via transactions.

8.2.5 Reporting and Analysis

The platform supports reporting and analysis features, which can display any dataset in various forms for ease of representation. The analysis module of the platform provides real-time on-demand Staging frequencies on patients, filtering options on stage, information on medication and complications; and customizable graphing and plotting interfaces (Figure 8-3). In the event that the built-in tools do not have the desired functionality, datasets in various common formats (CSV, Excel, SAS) can be extracted for further analysis of patterns and trends.

Figure 8-3 shows real-time on-demand Staging Frequencies on patients with filtering options on stage, drug, complications etc. and customizable graphing and plotting interfaces.

8.3 Conclusions

Developing and establishing effective and dynamic data collection systems can lead to the elimination of physical chart-pulls; a reduction in medical errors and prescription clarification with pharmacies; the implementation of electronic review of patient medical history from a single, accessible location; the notification of required tests, exams, or follow-ups for patient care; an improvement in reporting on patients and practices and communications between healthcare personnel; and the trending of patient vital and/or test results.

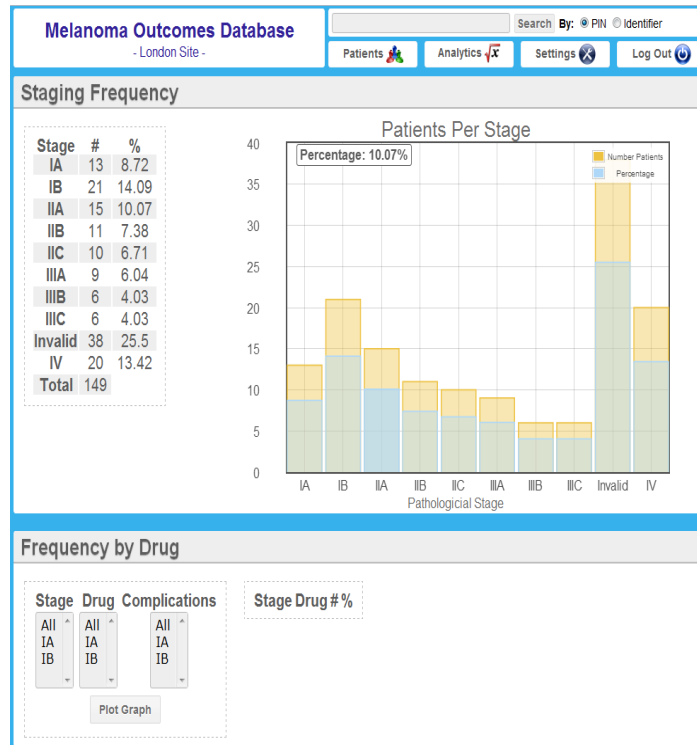


Figure 8-3: Analytics Module

Electronic data collection has the potential to significantly improve the quality of today's healthcare systems leading to improved patient safety and reduced healthcare costs [10-12]. However, while digitized systems enable easier and more efficient data extraction than traditional manual systems, it is important to promote the standardization of backend systems and to ensure that data not be held in silos and defined by large legacy systems where valuable information can remain uncultivated.

Our platform provides an interface for data subsets within a common platform view. By providing an interface for imaged data (X-RAYS, MRIs, CT scans etc.), we can use conventionally recorded clinical data to enhance review and analysis. Additionally, our interface can help inform clinical decision making by conducting preliminary disease or risk modeling using multiple datasets with other relevant databases.

8.4 Acknowledgements

This work was made possible by Dr. Scott Ernst that provided the initial platform framework to create our platform from.

8.5 References

1. Public Health Agency of Canada. 2001. Melanoma skin cancer facts and figures. Available at: http://www.phac-aspc.gc.ca/cd-mc/cancer/melanoma_skin_cancer_figures-cancer_peau_melanome_figures-eng.php. Accessed December, 2011.
2. Ernst DS, Eisenhauer E, Wainman N, Davis M, Lohmann R, Baetz T, Belanger K, Smylie M. Phase II study of perifosine in previously untreated patient with metastatic melanoma. *Investigational New Drugs* 2011;23:569-575.
3. Melanoma Center. Melanoma basics: melanoma statistics. 2010. Available at: <http://www.melanomacenter.org/basics/statistics.html>. Accessed December, 2011.
4. Howlader N, Noone AM, Krapcho M, Neyman N, Aminou R, Waldron W, et al. SEER Cancer Statistics Review, 1975-2008. 2010. Available at: http://seer.cancer.gov/csr/1975_2008/. Accessed December, 2011.
5. U.S. National Library of Medicine. 2011. A.D.A.M. medical encyclopedia: Melanoma. Available at: <http://www.ncbi.nlm.nih.gov/pubmedhealth/PMH0001853/>. Accessed: December, 2011.
6. American Cancer Society. 2002. Available at: www.cancer.org. Accessed December, 2011.
7. Public Health Agency of Canada. 2011. Melanoma skin cancer. Available at: http://www.phac-aspc.gc.ca/cd-mc/cancer/melanoma_skin_cancer-cancer_peau_melanome-eng.php. Accessed December, 2011.
8. Ames E, Ciotti V, Mathis B. Meaningful abuse: the rush toward EHR implementation. *Health Financ Manage* 2011;65(2):70-73.
9. Bell B, Thornton K. From promise to reality: achieving the value of an EHR. *Healthc Financ Manage* 2011;65(2):50-56.
10. Agarwal R, Gao G, DesRoaches C, Jha AK. Research commentary - The digital transformation of healthcare: current systems and the road ahead. *Information Systems* 2010;21(4):796-809.
11. Bowens FM, Frye PA, Jones WA. Health information technology: integration of clinical workflow into meaningful use of electronic health records. *Health Inf Manag* 2010;1.
12. Hillestad R, Bigelow J, Bower A, Girosi F, Meili R, Scoville R, et al. Can electronic medical records systems transform health care? Potential health benefits, savings, and cost. *Health Affairs (Millwood)* 2005;24(5):1103-1117.

Chapter 9 – Article 7

9 Burden of illness for metastatic melanoma in Canada: 2011–2013*

Abstract: Background - Detailed epidemiology for patients with advanced metastatic melanoma in Canada is not well characterized. We conducted an analysis of patients with this disease in the province of Ontario, with the aim being to study the presentation, disease characteristics and course, and treatment patterns for malignant melanoma.

Methods - In this Canadian observational, prospective, and retrospective study of patients with malignant melanoma, we used data collected via the Canadian Melanoma Research Network (CMRN) Patient Registry. We identified patients who were seen at one of 3 cancer treatment centres between April 2011 and April 30, 2013. Patient data from 2011 and 2012 were collected retrospectively using chart records and existing data in registries. Starting January 2013, data were collected prospectively. Variables investigated included age, sex, initial stage, histology, mutation type, time to recurrence, sites of metastases, resectability, and previous therapies.

Results - A cohort of 810 patients with melanoma was identified from the CMRN registry. The mean age was 58.7 years and the majority were male (60% vs 40%). Factors impacting survival included having unresectable or metastatic melanoma, initial stage at diagnosis, presence of brain metastasis, and *BRAF* mutation status. The proportion of surviving patients decreased with higher initial disease stages.

* A version of this chapter has been published: Scott Ernst, Teresa Petrella, Anthony Joshua, Ali Hamou, Marroon Thabane, Sharon Vantyghem, & Femida Gwadry-Sridhar. “Burden of illness for metastatic melanoma in Canada, 2011–2013”. *Current Oncology*, 2016 vol. 23(6), pp. 563-570.

Conclusions - Using the CMRN registry, we were able to determine detailed epidemiology of patients with melanoma in the Canadian province of Ontario, validating the comprehensive and detailed information that can be obtained from these data.

Keywords: Metastatic melanoma, epidemiology, burden of disease, cancer registry

9.1 Introduction

Melanoma is a malignant tumour that arises from melanin-producing cells called melanocytes [1-4]. Approximately 90% of melanoma are cutaneous, but they can also occur at any anatomical location (eg, eye, mucosal, head and neck surfaces, and along gastrointestinal and genitourinary tracts) [2,5,6]. Cutaneous malignant melanoma (CMM) is responsible for the vast majority (60% to 80%) of skin cancer-related deaths [4,7-11]. It was estimated that in 2012, over 232,000 people worldwide were diagnosed with CMM and over 55,400 died of this disease [12]. In Canada, an estimated 6,800 new cases of cutaneous melanoma and 1,150 related deaths are predicted for 2015 [13]. In addition, evidence suggests that the incidence of CMM across Canada is increasing, a trend that has also been seen in other countries worldwide [13-20].

The average 5-year survival rates are 90% and up to 70% for patients presenting with stage I or II disease, respectively [2,11]. Traditionally, survival rates fell to approximately 40% amongst those diagnosed with stage III melanoma, whilst the 1-year survival rate after stage IV melanoma diagnosis was 26% [2,21,22]. Patients with stage IV disease have very poor prognosis, with fewer than 10% alive at 5 years [2,23-26], although recent advances in targeted and immunotherapies have significantly improved these numbers [27-32]. Although the activity of targeted therapies and immunotherapies in melanoma have been promising, the prognosis for long-term, disease-free survival among those with metastatic and recurrent disease remains poor [33,34]. Thus, there remains an urgent unmet medical need for effective therapies in patients with advanced melanoma.

The objectives of this study were to determine the presentation, disease characteristics, disease course, and treatment patterns of CMM in Ontario.

9.2 Methods

9.2.1 Epidemiologic Analysis: Melanoma-Related Disease Characteristics

This was a Canadian multicentre, observational, prospective, and retrospective study of patients with CMM, using data collected from the Canadian Melanoma Research Network (CMRN) Patient Registry. Patients with CMM who were seen at 1 of 3 cancer centres were identified between April 2011 and April 30, 2013. Patient data were collected retrospectively in 2011 and 2012 using chart records as well as existing data in registries, and all data from January 2013 onward were collected prospectively. The study investigated disease distribution among patients with melanoma according to age, sex, body region, tumour site, initial stage, histological classification, mutation type, time to recurrence, sites of metastatic disease, resectability, and previous adjuvant and systemic therapies. All patients with confirmed melanoma and at least 12 months of follow-up data who were seen at any 1 of the 3 participating treatment centres were eligible for entry into the study. Patients who had less than 12 months' follow-up could be included, provided they were defined as such. Patients without histological confirmation of melanoma were excluded.

9.2.2 Statistical Methods

Logistic regression models used for survival analysis were generated with survival at 1 year, survival at 2 years, disease-free survival at 1 year, and disease-free survival at 2 years as dependent binary variables, and a selection of variables, which included patient age and sex, body region, stage, and *BRAF* mutation status, as independent variables.

All analyses were 2-tailed, with $P < .05$ set as the threshold for statistical significance, except for inclusion/exclusion of variables in multivariate models, for which $P < .10$ was used.

Statistical analyses were performed in consultation with the principle investigators, using SPSS version 20 statistical software (IBM Corp, Armonk, NY, USA).

9.3 Results

9.3.1 Patient Characteristics

From the CMRN Patient Registry, a cohort of 810 patients with CMM, diagnosed from 1964 to 2013 at 3 urban cancer treatment centres in Ontario, was identified. Patient characteristics

are detailed in Table 9-I. The cohort had a mean age of 58.7 ± 14.8 years and was predominantly male (60% vs 40%). At initial presentation, a broad spectrum of melanoma stages were represented, from stage 0 to stage IV (Figure 9-1). The mean time to recurrence for all patients in the cohort was approximately 5 years.

Seventy-eight patients (9.6%) had stage IV disease at diagnosis. Of these, 13 patients (1.6% of the entire cohort) had distant skin metastases with normal lactate dehydrogenase levels (M1A), 16 (2.0%) had lung metastases with normal lactate dehydrogenase levels (M1B), and 49 (6.0%) had metastases in other organs or any metastasis with high levels of lactate dehydrogenase (M1C).

The most common sites of primary disease, regardless of initial stage at diagnosis, were extremities (27.2%), trunk (25.9%), head (16.9%), and neck (4.8%). At the time of this study, 356 of the 810 patients (44%) had metastatic melanoma and 454 (56%) had non-metastatic disease. In addition, 704 (87%) had resectable disease, 106 (13%) had unresectable disease, 367 (45%) had unresectable or metastatic disease, and 51 (6%) had a *BRAF* mutation. It should be noted that *BRAF* testing was not routinely performed for most of the time period covered by the study and that data was only available for patients with unresectable and metastatic disease.

9.3.2 Treatment Modalities

At the time covered by this analysis, 356 of the 810 patients in the cohort had metastatic disease, of whom 341 (95.8%) had received prior systemic therapy, and 454 patients had non-metastatic disease, of whom 147 (32.4%) had received prior systemic therapy. Therefore, a total of 488 (60.2%) of the 810 patients had previously received systemic therapy at the time covered by this analysis.

Of the 367 patients with metastatic or unresectable disease at the time covered by this analysis, 346 (94.3%) had received prior systemic therapy, including 22.3% who had received ipilimumab, 19.9% who had received dacarbazine (DTIC) monotherapy, and 17.9% who had received an investigational drug in a clinical trial. Most patients with unresectable or metastatic disease had received DTIC monotherapy as first-line therapy and ipilimumab as second- and other-line therapy (Table 9-II).

Of the 147 patients with non-metastatic disease at presentation who had received systemic therapy by the time of this study, 24.5% had received an investigational drug in a clinical trial, 22.5% had received ipilimumab, and 17.7% had received DTIC monotherapy.

In all 810 patients identified, treatment modalities such as radiotherapy, surgery, and systemic therapy had been commonly used. At the time covered by this analysis, more patients had undergone radiotherapy (90.1%) than surgery (37.7%) or systemic therapy (23.5%), and few patients had undergone all 3 treatments (8.9%). For the 182 patients who presented with stage III or stage IV disease at diagnosis, both radiotherapy and surgery were most commonly utilized.

9.3.3 Factors Affecting Survival

9.3.3.1 Unresectable or Metastatic Disease

At the time covered by this analysis, 367 patients had unresectable or metastatic disease. The most common initial histological subtypes for patients with metastatic or unresectable disease was superficial spreading (42.2%) and nodular (18.5%) melanoma. At the time covered by this analysis, the proportion of patients with unresectable or metastatic disease still alive was approximately 51%, and the estimated median survival time was 63.7 months (95% CI, 48.3 to 79.2 months; Figure 9-2A).

9.3.3.2 Stage of Disease

Of the 182 patients who had stage III or IV disease at the time of initial diagnosis, 65% had metastatic disease and 58% had unresectable (presence of a extranodal distant metastasis or lymphovascular or perineural invasion) disease. The proportions of the 182 patients who had newly diagnosed vs recurrent disease at presentation were 48% and 52%, respectively, showing no statistical significance ($P = .350$). The proportion of surviving patients across progressing disease stages decreased. At the end of the study, 79.9% of patients who initially presented with stage 0-IIIC disease were still alive, compared with 71.0% of those who initially presented with stage III disease and 52% of those who initially presented with stage IV disease. The median survival times by initial disease stage were 109.1 months (95% CI, 95.7 to 122.5 months), 50.8 months (95% CI, 13.6 to 88.0 months), and 33.0 months (95% CI, 10.2 to 55.8 months) for stages 0-IIIC, III, and IV, respectively (Figure 9-2B, Table 9-IV).

The mean time to recurrence across all initial disease stages was 47.4 months (95% CI, 39.0 to 55.7 months).

9.3.3.3 BRAF Mutation Status

Of the 367 patients with unresectable or metastatic disease, 107 (29.2%) were tested for *BRAF* mutations. In these unresectable metastatic patients with known *BRAF* mutation status, 41 (38.3%) were *BRAF* mutation–positive, 8 (19.5%) of which were in the stage IV M1C classification. Of the patients who tested positive for *BRAF* mutation, the proportion surviving at the study end was 83.8%, with a median survival time of 83.3 months (95% CI, 28.2 to 138.3 months; Figure 2C). The proportion of patients surviving at study end who tested negative for *BRAF* mutation was 46.7%; their median survival time was 61.4 months (95% CI, 45.4 to 77.4 months). Overall, survival for patients with unresectable metastatic disease tested for *BRAF* mutation was 50.9% and the median survival time was 64.6 months (95% CI, 48.9 to 80.3 months).

Cumulative survival decreased more steadily in patients without *BRAF* mutation than those with the mutation, causing a rapid decline in survival over months (Figure 9-2C).

9.3.3.4 Brain Metastases

The brain metastasis cohort includes all patients who had brain radiotherapy. The proportion of the 367 patients with unresectable or metastatic disease with brain metastasis was 22.9%. Of these patients, 17.9% had brain metastasis at initial presentation 82.1% had brain metastasis subsequently. The proportion of surviving patients with brain metastases was 50.0% at initial presentation and 50.8% at subsequent presentation. The median survival time was 14.8 months (95% CI, 0 to 35.4 months) at presentation, and 61.2 months (95% CI, 16.4 to 106 months) subsequently. On average, patients with brain metastases had significantly lower survival time than other patients (Figure 9-2D).

9.3.3.5 Cox Proportional Model

A Cox proportional model developed to predict survival identified stage, unknown primary status, and brain metastases as significant predictors of survival at 1 year (Table 9-III), and male sex as an additional adverse prognostic factor for 2-year survival (Table 9-IV).

9.4 Discussion

The objective of this study was to provide a detailed epidemiological overview of patients with melanoma whose data were entered into the CMRN from 3 separate cancer treatment centres.

The population studied appears to be similar to that in other melanoma registries (eg, overall melanoma incidence trends for sex, age, and/or disease sites). [35-41] The mean age was 58.7 years and the cohort was predominantly male (60% vs 40%). There was a broad spectrum of initial stage representation, although there was an intentional preponderance of patients with unresectable and metastatic disease at the time covered by this analysis. The 3 clinical investigators from whose practices the patients were principally identified are medical oncologists and therefore tend to manage patients with advanced disease.

The molecular characterization of melanoma is proving critical in its subsequent management. The use of BRAF testing at all 3 centres has been available outside of clinical trials only over the past 2 years in Ontario. Consequently, the BRAF testing rate in this study is low, 29%. Testing rates are expected to sharply increase going forward as patients are considered for targeted therapies; it is now standard of care in Canada to test all patients with unresectable or metastatic disease for their *BRAF* mutation status. In our analysis, among the patients who underwent BRAF testing, 38.3% had *BRAF*-mutant tumours, which is consistent with other epidemiological reports [35,36]. Furthermore, the availability of BRAF inhibitors is also relatively recent, and therefore the impact of BRAF status and targeted therapy on survival cannot be assessed in this report.

Patients with brain metastases represented another important subgroup in this study, 18% of whom presented with brain metastasis at initial diagnosis. The overall rate of brain metastasis in all patients with advanced disease was 23%, which is also consistent previous reports [37]. The overall survival of patients with brain metastases was significantly inferior to that of patients without brain metastases, which underscores the importance of central nervous system involvement as a poor prognostic factor in melanoma and the unmet need for more effective treatments for this patient population.

Survival rates across initial disease stages outlined in this study are congruent with rates described in other large cohorts of patients [2,11,21,22]. In the Cox proportional model, the study identified that stage, unknown primary status, and brain metastases were significant predictors of survival at 1 year. For 2-year survival, male sex was an additional adverse prognostic factor, a result that is also consistent with previous findings [38,39]. Although other factors, such as treatment and mutational status, may potentially be important prognostic variables, the registry has yet to be populated with sufficient numbers of patients with adequate treatment and follow-up data to explore potential outcome variables. However, this is expected to change as the registry is expanded to include additional patients and lengthened follow-up information.

The primary limitation of this study is in the retrospective nature of an analysis of a limited cohort of patients. The inclusion of patients was based on the availability of data and was not intended to provide a comprehensive overview of all patients or of a specific subset of patients. Patient selection was therefore intrinsically biased by data availability and was limited to 3 geographical sites. Missing data were also an inherent problem of the study, which relied upon the presence of information in patient records. For example, up to 103 (12.7%) of patients from the total population of 810 and 25 (6.8%) of patients from the unresectable metastatic population of 367 were excluded from several survival analyses due to missing values \pm outliers. Furthermore, the time limits of the study reduced the ability to observe the impact of new diagnostic and treatment modalities. The proportion of patients who had undergone BRAF testing within the time period we observed was not as comprehensive as we would now see.

Notwithstanding, the study allowed for detailed accounting of the demographics and clinical outcomes of a large cohort of patients who were seen at 3 different institutions, and it also enabled the collection of relevant data sequentially over time, providing the ability to observe the impact of multiple sequential interventions over time.

The CMRN now includes 11 cancer treatment centres across Canada. As additional data are collected from these 11 centres, a better treatment utilization profile will become available, one that includes the newer agents and captures the prevalence of genomic testing. With the increased interest in personalized medicine, the ability to link treatment to genetic testing and

to collect prospective data will be valuable because it will allow for the comparative evaluation of multiple agents' effectiveness. Utilization of our patient portal to collect health utility and health-related quality of life data will also provide a better view of the impact that both the disease and the treatment have on cost-effectiveness.

9.5 Conclusions

This study validates the comprehensive and detailed information that can be obtained from the CMRN Patient Registry. Although extrapolations of these findings from urban centres in Ontario to the entire Canadian melanoma population would be premature, it appears that the initial patient base of the CMRN registry can be extremely informative. The platform can provide the basis for the development of a wide variety of hypotheses that can be explored both retrospectively and prospectively. As additional data become available from other institutions, the CMRN registry will be able to provide a better profile of the melanoma population, including their treatments and outcomes, and will be an invaluable resource in advancing the management of melanoma.

9.6 Acknowledgments

The Global Melanoma Research Network and Pulse Infoframe Inc, received funding from GlaxoSmithKline to conduct this study. Employees of GlaxoSmithKline participated in the protocol development, analysis, and interpretation of results, and in manuscript writing as reviewers. Editorial support was provided by Amanda L. Kauffman, PhD, of Articulate Science and funded by GlaxoSmithKline. We also thank Dew Das for editorial review of the manuscript.

9.7 Conflict of Interests Disclosure

We have read and understood *Current Oncology's* policy on conflicts of interest disclosure and declare the following interests: SE received no direct funding from GlaxoSmithKline at the time of the study; TP received honoraria for participation in advisory boards for GlaxoSmithKline; MT and SV were employees of GlaxoSmithKline at the time of the study; FGS, AH, and AJ have nothing to disclose.

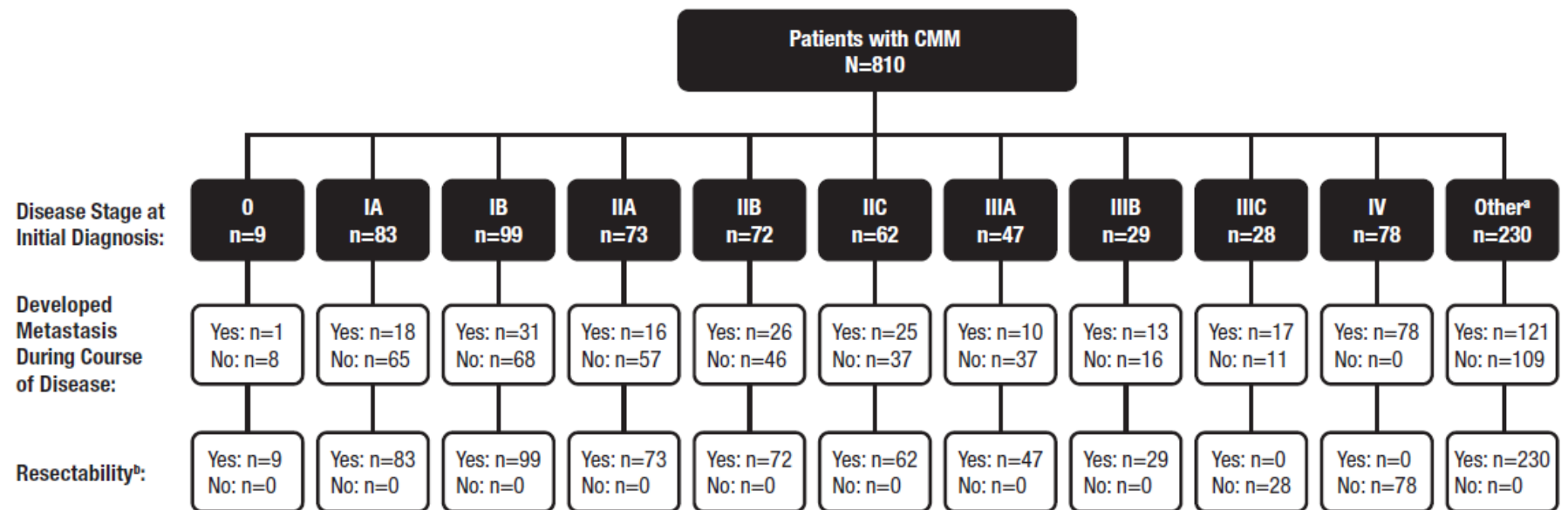


Figure 9-1: Flow diagram of metastases developed during the course of disease and resectability by disease stage at initial diagnosis.

^a Comprises ocular melanoma (n = 4), no primary site determined at staging (n = 26), and stage unknown (n = 200).

^b Unresectability was defined as the presence of a distant metastasis that is extranodal or the presence of lymphovascular or perineural invasion.

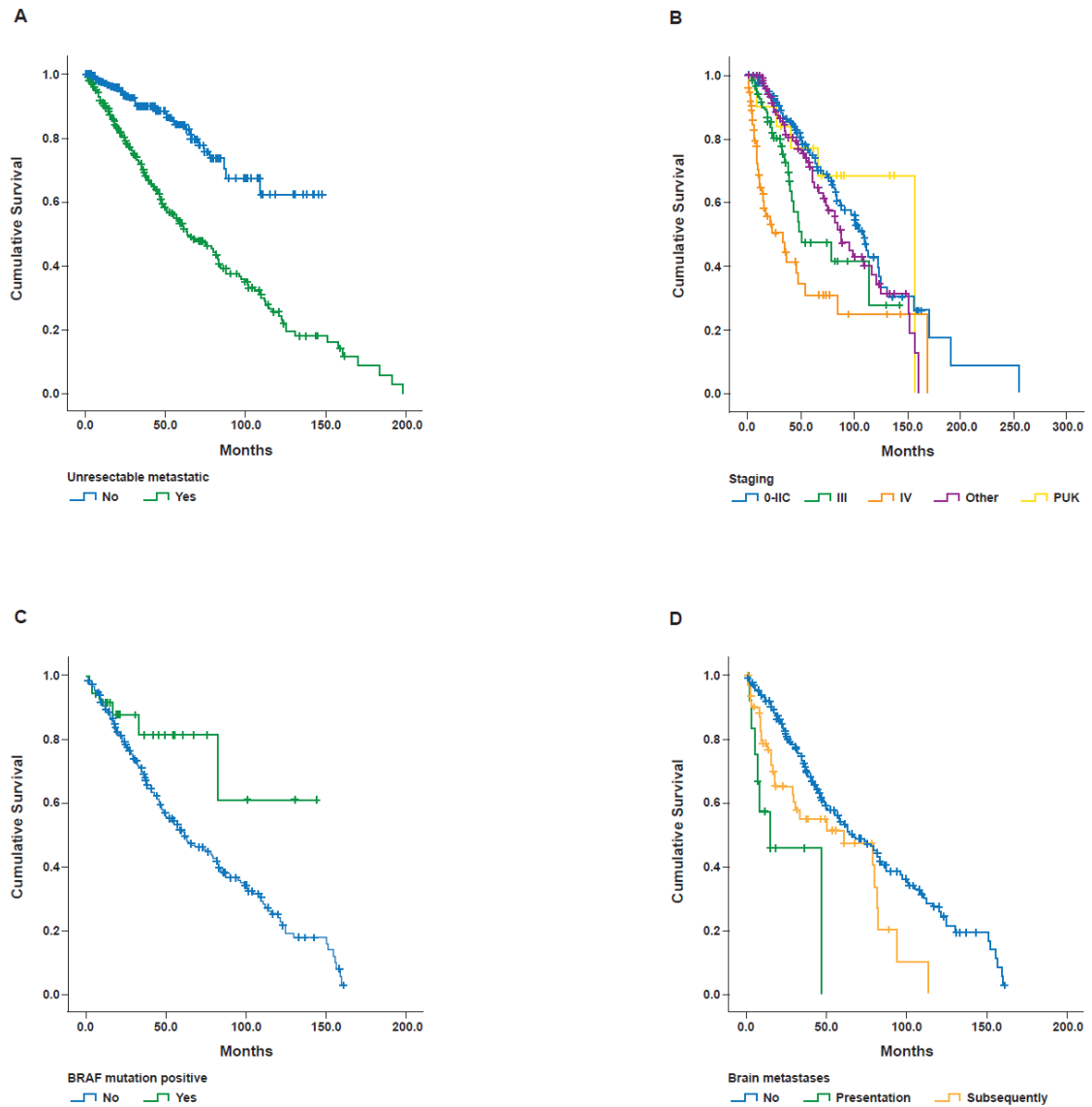


Figure 9-2: Kaplan-Meier survival curves for (A) patients with unresectable or metastatic disease vs all other patients in the entire cohort; (B) entire cohort by disease stage; (C) patients with unresectable or metastatic disease by presence or absence of BRAF mutation; and (D) patients with unresectable or metastatic disease by presence or absence of brain metastasis.

MEK	0	0	0	0	0	0	0	0	0	0	0	0
GNAO	0	0	0	0	0	0	0	0	0	0	0	0
GNA11	0	0	0	0	0	0	0	0	0	0	0	0
Metastatic status, n (%)												
Metastatic	356 (44.0)	1 (0.3)	18 (5.1)	31 (8.7)	16 (4.5)	26 (7.3)	25 (7.0)	10 (2.8)	13 (3.7)	17 (4.8)	78 (21.9)	121 (34.0)
Non metastatic	454 (56.1)	8 (1.8)	65 (14.3)	68 (15.0)	57 (12.6)	46 (10.1)	37 (8.1)	37 (8.1)	16 (3.5)	11 (2.4)	0	109 (24.0)
Resectability status, n (%)												
Resectable	704 (86.9)	9 (1.3)	83 (11.8)	99 (14.1)	73 (10.4)	72 (10.2)	62 (8.8)	47 (6.7)	29 (4.1)	0	0	230 (32.7)
Unresectable	106 (13.1)	0	0	0	0	0	0	0	0	28 (26.4)	78 (73.6)	0

^a Comprises ocular melanoma (n = 4, 0.5%), no primary site determined at staging (n = 26, 3.2%), and stage unknown (n = 200, 24.7%).

Table 9-2: Number of patients with unresectable or metastatic disease utilizing treatment modalities by line of treatment

	Line of Therapy, n (%)		
Treatments	First Line	Second Line	Other
n = 346	n = 210	n = 107	n = 29
Abraxane	2 (0.95)	1 (0.93)	1 (3.45)
Carboplatin + paclitaxel	35 (16.67)	14 (13.08)	6 (20.69)
Clinical trial	44 (20.95)	13 (12.15)	5 (17.24)
DTIC + cisplatin	10 (4.76)	5 (4.67)	0
DTIC + cisplatin + tamoxifen	0	1 (0.93)	0
DTIC alone	58 (27.62)	9 (8.41)	2 (6.9)
Imatinib	0	1 (0.93)	0
Ipilimumab	24 (11.43)	43 (40.19)	10 (34.48)
Paclitaxel	1 (0.48)	0	0
Temozolomide	9 (4.29)	3 (2.8)	1 (3.45)
Vemurafenib	23 (10.95)	9 (8.41)	1 (3.45)
Other	1 (0.48)	4 (3.74)	2 (6.9)
Unknown	3 (1.43)	4 (3.74)	1 (3.45)

DTIC, dacarbazine.

Table 9-3: Variables in the Cox proportional model for survival at 1 year

Variable	coef	exp(coef)	se(coef)	z	Pr(> z)	95% CI	
						Lower Bound	Upper Bound
Stage 0	1.45E+00	4.26E+00	6.88E-01	2.105	0.035276	1.10511	16.41
Stage IA	1.54E+00	4.67E+00	4.22E-01	3.649	0.000264	2.03997	10.675
Stage IB	1.38E+00	3.97E+00	4.07E-01	3.389	0.000701	1.78802	8.8
Stage IIA	1.37E+00	3.95E+00	4.52E-01	3.036	0.002395	1.62729	9.586
Stage IIB	9.51E-01	2.59E+00	4.69E-01	2.029	0.042466	1.03285	6.485
Stage IIC	2.96E-01	1.35E+00	4.98E-01	0.595	0.551885	0.50682	3.568
Stage IIIA	6.23E-01	1.87E+00	6.90E-01	0.903	0.366291	0.48238	7.213
Stage IIIB	-5.19E-01	5.95E-01	7.98E-01	-0.65	0.515434	0.12452	2.844
Stage IIIC	-1.40E+00	2.47E-01	1.06E+00	-1.315	0.188404	0.03073	1.985
Other at staging	-3.57E-01	7.00E-01	1.07E+00	-0.334	0.738226	0.08646	5.668
Stage IV	-9.47E-01	3.88E-01	5.74E-01	-1.649	0.099194	0.12592	1.196
PUK at staging	-1.58E+01	1.40E-07	3.03E+03	-0.005	0.995848	0	Inf
Sex (Male)	-3.32E-01	7.18E-01	1.96E-01	-1.694	0.090347	0.48862	1.054

Inf, infinity; PUK, unknown primary status.

Table 9-4: Variables in the Cox proportional model for survival at 2 years

Variable	coef	exp(coef)	se(coef)	z	Pr(> z)	95% CI	
						Lower Bound	Upper Bound
Stage 0	1.902	6.6993	0.5735	3.317	0.000911	2.17717	20.614
Stage IA	1.8446	6.3255	0.323	5.711	1.12E-08	3.35858	11.913
Stage IB	1.5345	4.6389	0.3136	4.893	9.94E-07	2.50879	8.578
Stage IIA	1.1826	3.2627	0.3426	3.452	0.000556	1.6672	6.385
Stage IIB	0.9165	2.5005	0.3493	2.624	0.008699	1.26093	4.959
Stage IIC	0.3141	1.369	0.4045	0.776	0.437478	0.61959	3.025
Stage IIIA	0.6687	1.9518	0.428	1.562	0.118219	0.84348	4.516
Stage IIIB	0.5425	1.7202	0.4648	1.167	0.243145	0.6918	4.278
Stage IIIC	-1.744	0.1748	1.0355	-1.684	0.092141	0.02297	1.33
Other at staging	-0.4679	0.6263	1.0357	-0.452	0.651414	0.08226	4.768
Stage IV	-0.3465	0.7072	0.4644	-0.746	0.455613	0.28461	1.757
Ocular at staging	0.9495	2.5845	1.0417	0.912	0.362017	0.3355	19.91
PUK at staging	0.6024	1.8266	0.6393	0.942	0.345997	0.52178	6.394
Sex (Male)	-0.1018	0.9032	0.1619	-0.629	0.529615	0.65763	1.241

PUK, unknown primary status.

9.8 References

1. Boyle GM. Therapy for metastatic melanoma: An overview and update. *Expert Rev Anticancer Ther* 2011 May;11(5):725-37.
2. Balch CM, Buzaid AC, Soong SJ, Atkins MB, Cascinelli N, Coit DG, Fleming ID, Gershenwald JE, Houghton A, Jr, Kirkwood JM, McMasters KM, Mihm MF, Morton DL, Reintgen DS, Ross MI, Sober A, Thompson JA, Thompson JF. Final version of the american joint committee on cancer staging system for cutaneous melanoma. *J Clin Oncol* 2001 Aug 15;19(16):3635-48.
3. Houghton AN, Polsky D. Focus on melanoma. *Cancer Cell* 2002 Oct;2(4):275-8.
4. Bandarchi B, Ma L, Navab R, Seth A, Rasty G. From melanocyte to metastatic malignant melanoma. *Dermatol Res Pract* 2010;2010:10.1155/2010/583748. Epub 2010 Aug 11.
5. Wilkins DK, Nathan PD. Therapeutic opportunities in noncutaneous melanoma. *Ther Adv Med Oncol* 2009 Jul;1(1):29-36.
6. Tas F, Keskin S, Karadeniz A, Dagoglu N, Sen F, Kilic L, Yildiz I. Noncutaneous melanoma have distinct features from each other and cutaneous melanoma. *Oncology* 2011;81(5-6):353-8.
7. American Cancer Society. Cancer Facts & Figures 2015 [Internet]. Atlanta, GA, USA: American Cancer Society cited May 2015]. Available from: <http://www.cancer.org/acs/groups/content/@editorial/documents/document/acspc-044552.pdf>
8. Cancer Research UK. Skin cancer mortality statistics. 2015
9. Radovic-Kovacevic V, Pekmezovic T, Adanja B, Jarebinski M, Marinkovic J, Tomin R. Survival analysis in patients with cutaneous malignant melanoma. *Srp Arh Celok Lek* 1997 May-Jun;125(5-6):132-7.
10. Miller AJ, Mihm MC, Jr. Melanoma. *N Engl J Med* 2006 07/06;355(1533-4406; 0028-4793; 1):51-65.
11. Diepgen TL, Mahler V. The epidemiology of skin cancer. *Br J Dermatol* 2002 Apr;146 Suppl 61:1-6.
12. Ferlay J, Soerjomataram I, Ervik M, Dikshit R, Eser S, Mathers C, Rebelo M, Parkin DM, Forman D, Bray F. GLOBOCAN 2012 v1.0, cancer incidence and mortality worldwide: IARC CancerBase no. 11 [internet]. 2013
13. Canadian Cancer Society. Canadian cancer statistics 2015. 2015
14. McLean DI, Phillips N, Zhou Y, Gallagher R, Lee TK. 40-year trends in skin cancer in british columbia, canada, 1973 to 2003. *J Cutan Med Surg* 2012 Mar-Apr;16(2):83-91.
15. Nevins T, Su Y, Doucette S, Kanigsberg N. Incidence of cutaneous malignant melanoma in the ottawa region: 1996 to 2006. *J Cutan Med Surg* 2008 Nov-Dec;12(6):276-81.
16. Golger A, Young DS, Ghazarian D, Neligan PC. Epidemiological features and prognostic factors of cutaneous head and neck melanoma: A population-based study. *Arch Otolaryngol Head Neck Surg* 2007 May;133(5):442-7.

17. Haider A, Mamdani M, Shear NH. Socioeconomic status and the prevalence of melanoma in ontario, canada. *J Cutan Med Surg* 2007 Jan-Feb;11(1):1-3.
18. Howlett AL, Dewar RA, Morris SF. The epidemiology of cutaneous malignant melanoma in nova scotia. *Can J Plast Surg* 2006 Winter;14(4):211-4.
19. Ulmer MJ, Tonita JM, Hull PR. Trends in invasive cutaneous melanoma in saskatchewan 1970-1999. *J Cutan Med Surg* 2003 Nov-Dec;7(6):433-42.
20. Boyle P, Levin B. World cancer report 2008. *International Agency for Research on Cancer* 2008
21. Agarwala SS. Current systemic therapy for metastatic melanoma. *Expert Rev Anticancer Ther* 2009 May;9(5):587-95.
22. Korn EL, Liu PY, Lee SJ, Chapman JA, Niedzwiecki D, Suman VJ, Moon J, Sondak VK, Atkins MB, Eisenhauer EA, Parulekar W, Markovic SN, Saxman S, Kirkwood JM. Meta-analysis of phase II cooperative group trials in metastatic stage IV melanoma to determine progression-free and overall survival benchmarks for future phase II trials. *J Clin Oncol* 2008 02/01;26(1527-7755; 0732-183; 4):527-34.
23. Huncharek M, Caubet JF, McGarry R. Single-agent DTIC versus combination chemotherapy with or without immunotherapy in metastatic melanoma: A meta-analysis of 3273 patients from 20 randomized trials. *Melanoma Res* 2001 02;11(0960-8931; 0960-8931; 1):75-81.
24. Lin H, Wong RP, Martinka M, Li G. Loss of SNF5 expression correlates with poor patient survival in melanoma. *Clin Cancer Res* 2009 Oct 15;15(20):6404-11.
25. Manola J, Atkins M, Ibrahim J, Kirkwood J. Prognostic factors in metastatic melanoma: A pooled analysis of eastern cooperative oncology group trials. *J Clin Oncol* 2000 Nov 15;18(22):3782-93.
26. Trinh VA. Current management of metastatic melanoma. *Am J Health Syst Pharm* 2008 Dec 15;65(24 Suppl 9):S3-8.
27. Hodi FS, O'Day SJ, McDermott DF, Weber RW, Sosman JA, Haanen JB, Gonzalez R, Robert C, Schadendorf D, Hassel JC, Akerley W, van den Eertwegh AJ, Lutzky J, Lorigan P, Vaubel JM, Linette GP, Hogg D, Ottensmeier CH, Lebbe C, Peschel C, Quirt I, Clark JI, Wolchok JD, Weber JS, Tian J, Yellin MJ, Nichol GM, Hoos A, Urba WJ. Improved survival with ipilimumab in patients with metastatic melanoma. *N Engl J Med* 2010 Aug 19;363(8):711-23.
28. McArthur GA, Chapman PB, Robert C, Larkin J, Haanen JB, Dummer R, Ribas A, Hogg D, Hamid O, Ascierto PA, Garbe C, Testori A, Maio M, Lorigan P, Lebbé C, Jouary T, Schadendorf D, O'Day SJ, Kirkwood JM, Eggermont AM, Dréno B, Sosman JA, Flaherty KT, Yin M, Caro I, Cheng S, Trunzer K, Hauschild A. Safety and efficacy of vemurafenib in BRAF^{V600E} and BRAF^{V600K} mutation-positive melanoma (BRIM-3): Extended follow-up of a phase 3, randomised, open-label study. *Lancet Oncol* 2014 Mar;15(3):323-32.
29. Hauschild A, Grob JJ, Demidov LV, Jouary T, Gutzmer R, Millward M, Rutkowski P, Blank CU, Miller WH, Jr., Kaemgen E, Martin-Algarra S, Karaszewska B, Mauch C, Chiarion-Sileni V, Martin A-, Swann S, Haney P, Mirakhur B, Guckert ME, Goodman V,

- Chapman PB. Dabrafenib in BRAF-mutated metastatic melanoma: A multicentre, open-label, phase 3 randomised controlled trial. *Lancet* 2012 06;380(9839):358-65.
30. Flaherty KT, Robert C, Hersey P, Nathan P, Garbe C, Milhem M, Demidov LV, Hassel JC, Rutkowski P, Mohr P, Dummer R, Trefzer U, Larkin JM, Utikal J, Dreno B, Nyakas M, Middleton MR, Becker JC, Casey M, Sherman LJ, Wu FS, Ouellet D, Martin AM, Patel K, Schadendorf D. Improved survival with MEK inhibition in BRAF-mutated melanoma. *N Engl J Med* 2012;367(2):107-14.
 31. Long GV, Stroyakovskiy D, Gogas H, Levchenko E, de Braud F, Larkin J, Garbe C, Jouary T, Hauschild A, Grob JJ, Chiarion-Sileni V, Lebbe C, Mandalà M, Millward M, Arance A, Bondarenko I, Haanen JBAG, Hansson J, Utikal J, Ferraresi V, Kovalenko N, Mohr P, Probst A, Schadendorf D, Nathan P, Robert C, Ribas A, DeMarini DJ, Irani JG, Swann S, Legos JL, Jin F, Mookerjee B, Flaherty K. Dabrafenib and trametinib versus dabrafenib and placebo for Val600 BRAF-mutant melanoma: A multicentre, double-blind, phase 3 randomised controlled trial. *Lancet* 2015;386(9992):444-51.
 32. Robert C, Karaszewska B, Schachter J, Rutkowski P, Mackiewicz A, Stroiakovski D, Lichinitser M, Dummer R, Grange F, Mortier L, Chiarion-Sileni V, Drucis K, Krajsova I, Hauschild A, Lorigan P, Wolter P, Long GV, Flaherty K, Nathan P, Ribas A, Martin AM, Sun P, Crist W, Legos J, Rubin SD, Little SM, Schadendorf D. Improved overall survival in melanoma with combined dabrafenib and trametinib. *N Engl J Med* 2015 Jan 1;372(1):30-9.
 33. Menaa F. Latest approved therapies for metastatic melanoma: What comes next? *J Skin Cancer* 2013;2013:735282.
 34. Khattak M, Fisher R, Turajlic S, Larkin J. Targeted therapy and immunotherapy in advanced melanoma: An evolving paradigm. *Ther Adv Med Oncol* 2013 Mar;5(2):105-18.
 35. McCarron CE, Ernst S, Cao JQ, Zaric GS. Population-based estimates of survival and cost for metastatic melanoma. *Curr Oncol* 2015 Oct;22(5):326-32.
 36. Johnson-Obaseki SE, Labajian V, Corsten MJ, McDonald JT. Incidence of cutaneous malignant melanoma by socioeconomic status in Canada: 1992-2006. *J Otolaryngol Head Neck Surg* 2015 Dec 2;44:53,015-0107-1.
 37. Erdmann F, Lortet-Tieulent J, Schuz J, Zeeb H, Greinert R, Breitbart EW, Bray F. International trends in the incidence of malignant melanoma 1953-2008--are recent generations at higher or lower risk? *Int J Cancer* 2013 Jan 15;132(2):385-400.
 38. Geller AC, Clapp RW, Sober AJ, Gonsalves L, Mueller L, Christiansen CL, Shaikh W, Miller DR. Melanoma epidemic: An analysis of six decades of data from the Connecticut tumor registry. *J Clin Oncol* 2013 Nov 20;31(33):4172-8.
 39. Marrett LD, Nguyen HL, Armstrong BK. Trends in the incidence of cutaneous malignant melanoma in New South Wales, 1983-1996. *Int J Cancer* 2001 May 1;92(3):457-62.
 40. Pruthi DK, Guilfoyle R, Nugent Z, Wiseman MC, Demers AA. Incidence and anatomic presentation of cutaneous malignant melanoma in central Canada during a 50-year period: 1956 to 2005. *J Am Acad Dermatol* 2009 Jul;61(1):44-50.

41. Severi G, Giles GG, Robertson C, Boyle P, Autier P. Mortality from cutaneous melanoma: Evidence for contrasting trends between populations. *Br J Cancer* 2000 Jun;82(11):1887-91.
42. Lovly CM, Dahlman KB, Fohn LE, Su Z, Dias-Santagata D, Hicks DJ, Hucks D, Berry E, Terry C, Duke M, Su Y, Sobolik-Delmaire T, Richmond A, Kelley MC, Vnencak-Jones CL, Iafrate AJ, Sosman J, Pao W. Routine multiplex mutational profiling of melanomas enables enrollment in genotype-driven therapeutic trials. *PLoS One* 2012;7(4):e35309.
43. Inamdar GS, Madhunapantula SV, Robertson GP. Targeting the MAPK pathway in melanoma: Why some approaches succeed and other fail. *Biochem Pharmacol* 2010 Sep 1;80(5):624-37.
44. Flanigan JC, Jilaveanu LB, Faries M, Sznol M, Ariyan S, Yu JB, Knisely JP, Chiang VL, Kluger HM. Melanoma brain metastases: Is it time to reassess the bias? *Curr Probl Cancer* 2011 Jul-Aug;35(4):200-10.
45. Joosse A, Collette S, Suci S, Nijsten T, Patel PM, Keilholz U, Eggermont AM, Coebergh JW, de Vries E. Sex is an independent prognostic indicator for survival and relapse/progression-free survival in metastasized stage III to IV melanoma: A pooled analysis of five european organisation for research and treatment of cancer randomized controlled trials. *J Clin Oncol* 2013 Jun 20;31(18):2337-46.
46. Mervic L. Time course and pattern of metastasis of cutaneous melanoma differ between men and women. *PLoS One* 2012;7(3):e32955.

Chapter 10

10 Concluding Thoughts

Throughout this thesis, several published articles have been examined to represent my transition from basic sciences research to clinical informatics research. In one way or another, the techniques described build on each other, and have fostered the nurturing of my skills to continue in the world of clinical informatics.

In the research of basic sciences, I began with the use of ultrasound imaging to present novel techniques in the segmentation of left ventricular function, the representation of tissue characterization, and the accurate measure of ejection fraction. These techniques leverage fundamental algorithms in active contouring, optical flow mechanics, and A-prior knowledge representation. I have shown that these novel techniques have made a quantitative improvement over the original methodologies presented and have made an impact in the research community. These articles have cumulatively been referenced 35 times.

Leveraging the medical understanding garnered in the basic science investigations, I branched off into clinical informatics studies, where I was able to accurately create models for representing and predicting Sepsis patients and Alzheimer's Disease patients. These studies were constructed on the foundations of cluster analysis, the use of decision tree generation, and hidden Markov modelling. Following this, I designed an efficient data capture model for progressive and chronic diseases, specifically Melanoma. This platform collects data directly from patients and clinicians, leverages external heterogeneous data sets, and allows for the meaningful extraction of information in real-time. As a result, the use of this model currently allows for meaningful studies to be disseminated in relative short order, as other researchers are now publishing using the resulting datasets.

10.1 Transition

The transition from basic science research to clinical informatics was an arduous and evolutionary learning experience. Initially, my sentiment towards all clinical research was one of deficiency and it genuinely not deserving the label “research contribution.” It is very apparent to me how wrong I was. Clinical informatics research is absolutely fundamental to the betterment of our society at large, and is in fact, a research tract that is critical to the *academic continuum* or *pathway*. If anything, clinical informatics research is the key way of applying fundamental basic science research efficiently to real world situations (in the cases presented above for clinical practice guidelines and the improvement of patient care). It is not simply the teasing of data sets for scholarly purposes, rather, it takes ingenuity and insight to understand what quantifiable data sets represent and why they are yielding results in a clinical capacity.

The paradigm shift to the world of clinical informatics has provided an introspective change on how I personally conduct my research today. Through this transition, a fundamental ‘stepping stone’ to better research understanding was provided. I believe that this provides a greater level of respect for the time and effort that is spent on studies that present the essential foundations for all future work. When I began this journey, the idea of interpreting my results based on arbitrary clinical impact or a practice guideline was foreign to me. I now know, that such research impacts real-world treatment patterns and helps to create models that provide predictions for interventions of care. This could potentially improve the quality of life of a patient or even save that life. This was the change that I wanted to be a part of and will continue to contribute to.

Now that my transition is complete, I will continue on this research tract and do my utmost to positively impact the world around me.

10.2 Future Outlook

The clinical informatics research presented in this thesis was based on fundamental mathematical models, that are in essence, basic research outcomes, applied in novel ways to deal with the real-world problems needing efficient solutions. Rather than continue to try and apply these models to several other disease domains, there is a genuine need to improve the

capture of data at its inception. This data is generated from patients, clinicians, laboratory tests, wearables, procedural outcomes, and a horde of other heterogeneous sources which all live in silos. This creates a seemingly overwhelming problem of how to consolidate and harmonize data sets without losing a large amount of granularity in the process. This heterogeneous data problem, if solved, can provide a multitude of useful information where silos are broken down in order to provide real guidance on patient outcomes and improvement of care.

As shown, I have already started to embark on this line of multidisciplinary research, and publishing works on disease costing and impact, effective data collection and deeper pipelines of clinical outcomes. This work includes elements from human computer interaction exploration for efficient visual interfaces, ontological language generation for data harmonization, and naturally, clinical domain knowledge for the speciality itself. I intend to continue on this research tract, as I believe it will have a great impact on the ever rich and growing data world.

Appendix

Copyrighted Materials and Permissions

All journals and conferences have provided written statements in their policies (Copyright forms) that give the author the right to include the published integrated articles, in full or in part, in this dissertation.

Curriculum Vitae

NAME: Ali K Hamou

EDUCATION:

- 2017 **Ph.D.**, Department of Computer Science, University of Western Ontario, London, Canada (Expected)
- 2003 **M.Sc.**, Department of Computer Science, University of Western Ontario, London, Canada
- 2001 **Hons B.Sc.**, Computer Science with a Minor in Theoretical Mathematics, University of Western Ontario, London, Canada

AWARDS AND SCHOLARSHIPS:

Academic/Research:

- 2012 Techcellence Innovation Award
- 2009 – 2011 Ontario Neurotrauma Foundation Mentor-Trainee New Investigator
- 2004 – 2008 Ontario Graduate Scholarship (OGS)
- 2007 UWO Research in Computer Science Best Presentation Award
- 2005 – 2006 Western Research Graduate Scholarship
- 2005 UWO Research in Computer Science Best Presentation Award
- 2002 – 2003 Ontario Graduate Scholarship in Science and Technology
- 2002 Ontario Students Opportunity Grant
- 1999 – 2000 Laurence Paterson Scholarship
- 1999 – 2000 Canadian Millennium Scholarship
- 1998 – 1999 Deans Honour Roll
- 1997 Neilson and Associates Computer Science Scholarship
- 1997 University of Western Ontario Entrance Scholarship

Teaching:

- 2006 – 2007 Nominated for SOGS Best Teaching Assistant Award
- 2006 Faculty of Science Best Teaching Assistant Award

PROFESSIONAL EXPERIENCE:

- 2011 – 2016 **CTO, Head of Analytics & Co-Founder**
Pulse Inframe Inc.
- 2009 – 2014 **Research Associate**
I-THINK Research Health Informatics Labs
Lawson Health Research Institute, Canada
- 2003 – 2004 **Instructional Support Coordinator**
The University of Western Ontario

TEACHING EXPERIENCE:

- 2010** **Course Instructor:** *Distributed Systems and Parallel Computing*
The University of Western Ontario (Fourth Year Level)
- 2008** **Course Instructor:** *Software Tools and Systems Programming*
The University of Western Ontario (Second Year Level)
- 2003** **Course Instructor:** *Advanced Computer Networks*
The University of Western Ontario (Fourth Year / Graduate Level)
- 2005 – 2008** **Teaching Assistant**
The University of Western Ontario
- 09/07 – 04/08: *Game Development Project (Fourth Yr)*
- 09/07 – 04/08: *Software Maintenance and Configuration Management (Second Yr)*
- 03/07 – 04/07: *Object-Oriented Design and Analysis (Third Yr)*
- 09/06 – 12/06: *Advanced Image Compression (Fourth Yr)*
- 09/05 – 12/07: *Software Engineering (Third Yr)*
- 05/05 – 08/05: *C++ Fundamentals (Third Yr)*
- 09/02 – 12/02: *Advanced Computer Networks (Fourth Yr)*
- 01/02 – 04/02: *Distributed Systems (Fourth Yr)*
- 09/01 – 12/01: *Java Fundamentals (First Yr)*

PUBLICATIONS:

1. Scott Ernst, Teresa Petrella, Anthony Joshua, **Ali Hamou**, Marroon Thabane, Sharon Vantyghem, & Femida Gwadry-Sridhar. “Burden of illness for metastatic melanoma in Canada, 2011–2013”. *Current Oncology*, 2016 vol. 23(6), pp. 563-570.
2. **Ali Hamou**, Stacey Guy, Alexandria Ratzki-Leewing, Jesse O’Brien, Femida Gwadry-Sridhar, “A Disease Registry and Disease Management System for Patients with Malignant Melanoma”, *AHIC – Advances in Health Informatics Conference*, 2012.
3. **Ali Hamou**, Jesse O’Brien, Femida Gwadry-Sridhar, “Comprehensive Web-Based Patient Data Collection Systems with Integrated Imaging Functionality”, *MICCAI - Medical Image Computing and Computer Assisted Intervention, High Performance and Distributed Computing for Medical Imaging Workshop*, 2011.
4. **Ali Hamou**, Jesse O’Brien, Stacey Guy, Femida Gwadry-Sridhar, “InfoFrame – An Intelligent Informatics Data Collection Framework”, *IEEE Computer Based Medical Systems*, 2011, pp. 1-6.
5. **Ali Hamou**, Andrew Simmons, Michael Bauer, Benoit Lewden, Yi Zhang, Lars-Olof Wahlund, Eric Westman, Megan Pritchard, Iwona Kloszewska, Patrizia Mecozzi, Hilkka Soininen, Magda Tsolaki, Bruno Vellas, Sebastian Muehlboeck, Alan Evans, Per Julin, Niclas Sjögren, Christian Spenger, Simon Lovestone, Femida Gwadry-Sridhar and the AddNeuroMed consortium, “Cluster analysis of MR imaging in Alzheimer’s disease using decision tree refinement”, *International Journal of Artificial Intelligence*, 2011, vol. 6(S11), pp. 90-99.

6. Femida Gwadry-Sridhar, **Ali Hamou**, Benoit Lewden, Claudio Martin, Michael Bauer, "Predicting Sepsis: A Comparison of Analytical Approaches", *eHealth 2010, 3rd International ICST Conference on Electronic Healthcare for the 21st Century*, 2010.
7. Femida Gwadry-Sridhar, Michael Bauer, Benoit Lewden, **Ali Hamou**, "A Clustered Markov Analysis of Patients Developing Sepsis", *European Conference on Artificial Intelligence, Knowledge Representation For Health Care (KR4HC)*, 2010.
8. **Ali Hamou**, Stacey Guy, Benoit Lewden, Adam Bilyea, Michael Bauer and Femida Gwadry-Sridhar, "Data Collection with iPhone Web Apps: Efficiently Collecting Patient Data Using Mobile Devices", *International Conference on e-Health Networking, Application & Services (HealthCom)*, 2010, pp 235-239.
9. **Ali Hamou**, Michael Bauer, Benoit Lewden, Andrew Simmons, Yi Zhang, Lars-Olof Wahlund, Catherine Tunnard, Iwona Kloszewska, Patrizia Mecozzi, Hilka Soininen, Magda Tsolaki, Bruno Vellas, Sebastian Muehlboeck, Alan Evans, Per Julin, Niclas Sjögren, Christian Spenger, Simon Lovestone, Femida Gwadry-Sridhar, and other participants in the AddNeuroMed consortium, "Cluster Analysis and Decision Trees of MR Imaging in Patients Suffering Alzheimer's", *Trends in Practical Applications of Agents and Multiagent Systems, Advances in Soft Computing*, 2010, vol. 71, pp. 477-484.
10. **Ali K. Hamou** and Mahmoud R. El-Sakka, "Optical Flow Active Contours with Primitive Shape Priors for Echocardiography", *EURASIP Journal on Advances in Signal Processing*, vol. 2010, Article ID 836753, 10 pages, 2010.
11. **Ali K. Hamou** and Mahmoud R. El-Sakka, "An SRAD and Optical Flow Based External Energy for Echocardiograms", *International Conference on Image Processing (ICIP)*, 2009, pp. 2613-2616.
12. **Ali K. Hamou** and Mahmoud R. El-Sakka, "Active Contours with Optical Flow and Primitive Shape Priors for Echocardiographic Imagery", *International Conference on Imaging Theory and Applications (IMAGAPP)*, 2009, pp. 111-118.
13. **Ali K. Hamou**, Said Osman and Mahmoud R. El-Sakka, "Carotid Ultrasound Segmentation Using DP Active Contours", *International Conference on Image Analysis and Recognition (ICIAR)*, 2007, LNCS 4633, pp. 961-971.
14. **Ali K. Hamou** and Mahmoud R. El-Sakka, "Blood Flow Generation in B-Mode Ultrasound Images of the Carotid Artery", *IEEE International Conference on Image Processing (ICIP)*, 2004, pp. 2945-2948.
15. Amr Abdel-Dayem, **Ali K. Hamou** and Mahmoud R. El-Sakka, "Novel Adaptive Filtering for Salt and Pepper Noise Removal from Binary Document Images", *International Conference on Image Analysis and Recognition (ICIAR)*, 2004, LNCS 3212, pp 191-199.
16. **Ali K. Hamou** and Mahmoud R. El-Sakka, "A Novel Segmentation Technique For Carotid Ultrasound Images", *IEEE International Conference on Acoustics, Speech, and Signal Processing (ICASSP)*, 2004, vol. 3, pp. 521-524.
17. **Ali K. Hamou** and Mahmoud R. El-Sakka, "Wavelet-Filter Performance Evaluation for Digital Images", *IEEE Canadian Conference on Electrical and Computer Engineering (CCECE)*, 2003, vol. 3, pp. 2075-2078.

18. **Ali K. Hamou**, “Segmentation of Carotid Artery Ultrasound Images”, *The University of Western Ontario*, Master of Science Dissertation, 2003.

BOOK CHAPTERS

1. Femida Gwadry-Sridhar, Michael Bauer, Benoit Lewden, **Ali Hamou**. “A Markov Analysis of Patients Developing Sepsis Using Clusters”, *Knowledge Representation for Health-Care, Lecture Notes in Computer Science*, 2011, Springer Berlin / Heidelberg, vol. 6512, pp. 85-100.
2. **Ali K. Hamou** and Mahmoud R. El-Sakka, “SRAD, Optical Flow and Primitive Prior based Active Contours for Echocardiography”, *Computer Vision, Imaging and Computer Graphics. Theory and Applications. VISIGRAPP 2009. Communications in Computer and Information Science*, 2010, Springer Berlin / Heidelberg, vol. 68, pp. 158-171.